AN INVESTIGATION OF LOW ENERGY $^{1}H(\vec{d},\gamma)^{3}He$ and $^{2}H(\vec{p},\gamma)^{3}He$ REACTIONS

by

Lijun Ma

A dissertation submitted to the faculty of the University of North Carolina at Chapel Hill in partial fulfillment of the requirement for the degree of Doctor of Philosophy in the Department of Physics and Astronomy.

Chapel Hill

1995

Approved by:

_____ Advisor

_____ Reader

_____ Reader

LIJUN MA. An Investigation of Low Energy $^{1}H(d,\gamma)^{3}He$ and $^{2}H(p,\gamma)^{3}He$ Reactions (Under the direction of Hugon J. Karwowski)

ABSTRACT

Angular distributions of the vector analyzing power A_y for $^{2}H(\vec{p},\gamma)^{3}He$ at an energy range of $E_{c.m.}$= 70-210 keV c.m. together with the vector and tensor analyzing powers iT_{11} T_{20} and T_{22} for $^{1}H(\vec{d},\gamma)^{3}He$ at an energy range of $E_{c.m.}$= 40-110 keV have been measured for the first time under the present investigation. The total cross section and astrophysical S-factor have been measured at $<E_{c.m.}>$=75, 108, 133, and 173 keV. Measurements of the analyzing powers for the reactions bear a great importance in probing low energy radiative capture reaction mechanisms such as meson-exchange-current effects, microscopic descriptions of the ^{3}He system and the role of the Coulomb field in the exact three-body formalism. In astrophysics, these reactions are the leading P-P chain reactions in the nucleosynthesis of main sequence stars. Precise measurements of their astrophysical S-factors could better our understanding of stellar evolution processes. In the course of the present investigation, vapor condensed ice or heavy ice targets and two large volume High Purity Germanium γ-ray detectors were used. The functional energy dependence for all the analyzing powers are extracted. The final results are compared and interpreted under two realistic nuclear models: Refined Resonating Group Model and Correlated Hyperspherical Harmonics expansion model.

ACKNOWLEGEMENTS

Many people have contributed immeasurably to this project. It would have never been possible without their help and support. First of all, I would like to thank my advisor Dr. Hugon Karwowski for his guidance, understanding and many long hours of hard work that have made this project advancing and fruitful. I would like to thank my committee members Dr. Tom Clegg, Dr. Jon Engel, Dr. Edward Ludwig and Dr. Steve Shafroth for their valuable advice and many helps throughout this project. I am specially thankful for Dr. William Thompson for offering me countless assistance in data analysis and numerical methods. I would also like to thank Dr. John Halton for many stimulating lectures and discussions.

Throughout this project, many postdoctoral fellows and graduate students have helped me tremendously with the data collecting process. Many thanks go to Dr. Zeid Ayer, Dr. Jeff Blackmon, Dr. Tim Black, Dr. Carl Brune, Dr. Eric Crosson, Dr. Ben Crowe, Dr. Rupak Das, Dr. Kurt Fletcher, Dr. Susan Lemieux, Dr. Beata Kozlowska, Dennis Dinge, Bill Geist, Steve Hale, Brian Hendrix, Denise Ralston, and Kevin Veal for their invaluable friendships and many long hours spent together in the control room.

I am also very grateful for the assistance that I received from all the technical staff at Triangle Universities Nuclear Lab and the University of North Carolina at Chapel Hill. These include Mr. Paul Carter, Richard O'Quinn, John Dunham, Sidney Edward, Patrick Mulkey, Bob Hogan, Hal Mann, Bo Sanford and David Lashley. I specially thank Mr. Paul Carter for his patience and many advice of wisdom.

Finally, I contribute all my effort and progress to my financée Quan Xin, whose love, support and sacrifices made everything possible for me. Throughout many difficult times, my parents and Quan are always there for me. I would like to dedicate this thesis to them. As in the words of my father: "You are fortunate."

TABLE OF CONTENTS

Chapter **Page**

I. Introduction 1

1.1 Background and Motivation 1

1.2 Nuclear Capture Reaction Mechanism 3

1.3 Meson-exchange-current effects 6

1.4 Three-body ^{3}He wave function 9

1.5 Coulomb effects 10

1.3 Astrophysical Significance 12

1.4 Review of the Previous Experimental Work 17

1.5 Review of the Previous Theoretical Work 19

II. Instrumentation Developments and Techniques 23

2.0 Overview 23

2.1 TUNL Polarized Ion Source 23

2.2 TUNL Low Energy Beam Accelerator Facility (LEBAF) 30

2.3 Beam Transport System and Minitandem Accelerator 31

2.4 Scattering Chamber Design 34

2.5 Deuterated and Hydrogenated Target Fabrication 37

2.5.1 Compressed Chemical Compounds Targets 38

2.5.2 Gas Evaporation Techniques 41

2.5.3 Ion and Plasma Implantation Techniques 47

2.5.4 Solid Ice and Heavy Ice Targets 51

2.6 Detectors 53

III. Experimental Techniques and Methods 57

3.1 Overview 57

3.2 Cross Section Determination 57

3.3 Analyzing Powers Formalism 58

3.4 Data Acquisition System 66

3.5 Proton Polarimeter 69

3.6 Low Energy and High Energy Deuteron Polarimeter 73

IV. Data Analysis and Observables Reduction 76

4.0 Overview 76

4.1 Analyzing Powers Data Analysis 77

4.2 Kinematics of the Reactions 77

4.3 Energy Calibration 79

4.4 Background Subtraction 83

4.5 Functional Form for Spectra Fitting 85

4.6 Detector Response Function 87

4.7 Beam Stopping Effects 90

4.8 Cross Section Expansion 92

4.9 Fitting Algorithm 93

4.10 Error Analysis for Analyzing Powers 97

4.11 Cross Section Data Analysis 101

4.12 Target Thickness and Beam Integration 101

4.13 Detection Efficiencies and Geometric Corrections 104

4.14 The Reduction of Total Cross Section 111

4.15 Error Analysis for Cross Sections 114

V. Final Results and Comparison With Previous Measurements 116

5.0 Overview 116

5.1 Legendre Polynomial Analysis 116

5.2 Vector Analyzing Powers 118

5.3 Tensor Analyzing Powers 126

5.4 Total Cross Section and S-factor 132

VI. Theoretical Analysis 138

6.1 Introduction 138

6.2 Important Characteristics of RRGM 141

6.3 System Hamiltonian and Meson-exchange-current 142

6.4 Wave Functions 145

6.5 Results of RRGM Calculations and Comparison With Data 147

6.6 Full Three-body Variantional Method 151

6.7 Faddeev Expansions 154

6.8 Variantional Wave Functions 155

6.9 Results of CHH Calculations and Comparison With Data 158

VII. Conclusion and Future work 163

References.....168

LIST OF TABLES

Table 2.1 Transition units settings used for obtaining vector and tensor polarized proton and deuteron beams. The combinations of SF2 and MF2 units can be used for one fast spin-scheme 25

Table 2.2 Typical values of beam current along TUNL LEBAF beam line 32

Table 2.3 Physical properties of BaF2 and NaI scintillators 52

Table 3.1 The switching values for three spin states selections 66

Table 5.1 Multipole contributions to each Legendre expansion coefficients 116

Table 5.2 Legendre coefficients of A_y for $^2H(\vec{p},\gamma)^3He$ at four reaction energies, where fore-aft symmetry is assumed for unpolarized cross sections, i.e., $a_1=0$. By definition $a_0=1$ 123

Table 5.3 Legendre coefficients of iT_{11} for $^1H(\vec{d},\gamma)^3He$ at four reaction energies 123

Table 5.4 Legendre coefficients of T_{20} for $^1H(\vec{d},\gamma)^3He$ at four reaction energies 129

Table 5.5 Legendre coefficients of T_{22} for $^1H(\vec{d},\gamma)^3He$ at four reaction energies. Note that e_0 and e_1 are zeros by definition 129

Table 6.1 Comparison of ^3H and ^4He binding energies by various calculation method 149

LIST OF FIGURES

Figure 1.1 The flow chart of P-P chain reactions 12

Figure 2.1 The schematic drawing of TUNL Atomic Beam Polarize Ion Source (ABPIS) 22

Figure 2.2 Breit-Rabi diagrams for hydrogen and deuterium atoms as a function of magnetic field. The B_c is critical external magnetic field and ΔW is character frequency. 24

Figure 2.3 The layout for TUNL low energy bay with LEBAF setup 29

Figure 2.4 Detailed layout of TUNL Low Energy Beam Accelerator (LEBAF). The arrow indicates the beam traveling direction..... 30

Figure 2.5 The schematics for main proton-deuteron capture scattering chamber. In the figure, Part A is side-view of the main chamber body, and part B is the solid target mounting assembly ..... .35

Figure 2.6 The evaporator setup for depositing deuteride or hydride targets. The egg-shaped transparent dome in the figure is vacuum sealed and isolated from the aluminum bottom plate 41

Figure 2.7 Scattering chamber set-up for target thickness measurements..... 42

Figure 2.8 Profiling spectrum for a TiH_2 target with 3 μm foil thickness 43

Figure 2.9 On-line Spectrum of $^2H(p, \gamma)^3He$ reaction measured from BaF_2 scintillator 44

Figure 2.10 The background subtracted peak spectrum from Figure 2.8. The solid line is the Gaussian fit 45

Figure 2.11 Set-up for ion implantation of thin Ti hydride or deuteride targets 46

Figure 2.12 Set-up for making hydrogenated targets by plasma deposition technique 48

Figure 2.13 Schematic drawing of the apparatus for making vapor condensed targets 50

Figure 3.1 The Madison convention for spin orientations 56

Figure 3.2 Block diagram for generating three-state switching using TUNL SSC module and illustration of the timing relationship among the three states 64

Figure 3.3 Block diagram for scalar interfacing 65

Figure 3.4 Block diagram for two solid state detectors that had been used for polarization monitor measurement 67

Figure 3.5 Block diagram for electronics setup of BaF_2 scintillator. The dashed box represents the set-up for the pulse shape discrimination used in the target testing runs 68

Figure 3.6 The 52° chamber set-up for measuring polarization of either proton or deuteron beam. Top part of the chamber was used for proton polarimeter and bottom part was used for deuteron polarimeter 69

Figure 3.7 Stability of vector polarization for polarized proton beam 71

Figure 3.8 Stability of P_{zz} for state-3 transition during one run sequence 73

Figure 4.1 Raw spectrum from proton-deuteron capture reaction at E_p=312 keV 77

Figure 4.2 Blow-up view of an accumulated on-line background spectrum... 79

Figure 4.3 Typical energy calibration curve for one spectrum. The line shown here carries a energy resolution of 0.9397 ± 0.0026 keV/channel..... 80

Figure 4.4 The stopping power for solid D_2O from TRIM92 calculations compared with the experimental data from Wenzel and Whaling[Wen52] 88

Figure 4.5 The full energy γ-ray spectrum from $^2H(\vec{d}, \gamma)^3He$ reaction detected at 90° for one spin state. The functional fit shown here has a χ^2/nf=1.2 94

Figure 4.6 The energy dependence for the integrated distance from D_2O stopping power.....101

Figure 4.7 Time dependence of BCI normalized γ-ray yield from $^2H(p,\gamma)^3He$ reaction. The constant line is the mean value reference line. Each run number corresponds on average to a period of 6 hours.....102

Figure 4.8 The simulated γ-ray spectrum for $^2H(p, \gamma)^3He$ reaction at $E_{c.m.}$= 200 keV. The full dynamics is included in this calculation, in which energy dependence of the cross section (or S-factor) was

taken from the previously extracted functional form [Rof88].....104

Figure 4.9 Calculated kinematic distribution of γ-rays for 125% HPGe detector placed at 90° lab angle.....105

Figure 4.10 γ-ray spectrum from $^{19}F(p, \alpha\gamma)^{16}O$ resonance reaction at 340 keV 108

Figure 4.11 Detected α-particles from $^{19}F(p, \gamma\alpha)^{16}O$ reaction. The pulser peak in the spectrum are used for gain adjusting of the amplifiers 107

Figure 4.12 The energy dependence of absolute photo peak efficiency for 125% HPGe detector. The exponential fit to the data has a reliability $R^2 = 0.998$ 109

Figure 5.1 The energy dependence of A_y for $^2H(\vec{p},\gamma)^3He$ reactions 118

Figure 5.2 The energy dependence of iT_{11} for $^1H(\vec{d},\gamma)^3He$ reactions 119

Figure 5.3 The best Legendre polynomials' fit of A_y for $^2H(\vec{p},\gamma)^3He$ at four sampled energies. The table of the all the fitting coefficients is given in Table 5.2 121

Figure 5.4 The best Legendre polynomial fits of iT_{11} for $^2H(\vec{d},\gamma)^3He$ at four energies. The table list for the fitting coefficients is given in Table 5.3.....122

Figure 5.5 Measured energy dependence of T_{20} for $^1H(\vec{d},\gamma)^3He$ reaction 125

Figure 5.6 Measured energy dependence of T_{22} for $^1H(\vec{d},\gamma)^3He$ reaction 126

Figure 5.7 The best Legendre polynomials' fit of T_{20} for $^1H(\vec{d},\gamma)^3He$ at four reaction energies.....127

Figure 5.8 The best Legendre polynomial's fit of T_{22} for $^1H(\vec{d},\gamma)^3He$ at four reaction energies.....128

Figure 5.9 The angular distributions of the cross sections at four binned energies.....130

Figure 5.10 Energy dependence of the Legendre coefficients for cross section data. The solid line in the second plot is the linear regression result with a 95% confidence level enclosed by two dashed lines.....131

Figure 5.11 The extracted total cross sections in comparison with previous results.....132

Figure 5.12 The comparison among the present extracted S-factors and previous measurements [Rof88, Sch95].....133

Figure 6.1 Diagram for allowed leading transitions and channel spins for proton-deuteron capture reactions.....136

Figure 6.2 Illustration of cluster pairing for ^3He in the RRGM calculation.....138

Figure 6.3 The leading meson exchange terms included in the RRGM calculation.....141

Figure 6.4 Comparison between measured iT_{11} and RRGM calculations for $^1H(\vec{d},\gamma)^3He$ reaction. The data points shown here are the

measured results at center of mass of 50 keV 145

Figure 6.7 RRGM calculations and measured T_{20} for $^1H(\vec{d},\gamma)^3He$ at 50 keV c.m 146

Figure 6.8 RRGM calculations and measured T_{22} for $^1H(\vec{d},\gamma)^3He$ at 50 keV c.m 146

Figure 6.9 RRGM calculations compared with the measured A_y for $^2H(\vec{p},\gamma)^3He$ reaction at 70 keV c.m.....147

Figure 6.10 The definitions of Jacobi coordinates for ^3He system 150

Figure 6.11 Comparison between CHH model calculation and measured iT_{11} for $^1H(\vec{d},\gamma)^3He$ reaction at 50 keV c.m 155

Figure 6.12 Comparison between CHH model calculation and measured T_{20} for $^1H(\vec{d},\gamma)^3He$ reaction at 50 keV c.m 155

Figure 6.13 Comparison between CHH model calculation and measured T_{22} for $^1H(\vec{d},\gamma)^3He$ reaction at 50 keV c.m 156

Figure 6.14 Comparison between CHH model calculation at 50 keV c.m. and the measured A_y for $^2H(\vec{p},\gamma)^3He$ reaction at 70 keV c.m.....156

I. Introduction

1.1 Background and Motivation

Low energy $^{2}H(p,\gamma)^{3}He$ and $^{1}H(d,\gamma)^{3}He$ radiative capture reactions are the benchmark experiments in few-body nuclear physics and nuclear astrophysics. Both reactions have been widely studied for energies ranging from several keV to few hundreds of MeV.

In the area of few body physics, many aspects of the three-body nuclear dynamics and structures can be probed by studying these two sister reactions, particularly the meson-exchange-current (MEC) effects, Coulomb field distortion and "exact" three-body dynamics. Recent experimental and theoretical results have indicated that polarization observables are particularly adequate and useful for studying these effects (see next section for references). Furthermore, new techniques in the theoretical nuclear physics propelled by the fast advancements in super computing have made it possible for the first time to perform the real-time calculations using realistic nucleon-nucleon potentials. Meanwhile, developments in the techniques of efficient production of intense polarized ion beams at Triangle Universities Nuclear Laboratory (TUNL) [Cle93] have made possible to measure the polarization observables in proton-deuteron radiative capture reactions at energies below $E_{c.m.}$= 200 keV for the first time as well. Thus performing such measurements becomes the primary theme for this thesis investigation.

The astrophysical significance for measuring such reactions lies in the fact that proton-deuteron radiative capture processes are the leading reactions in describing

nucleosynthesis and stellar evolution. They are the key effective reactions in generating solar energies which continuously affect the present solar system. A thorough study of these reactions could contribute to better understanding of the production of the solar energy which all the biological life on the earth relies upon.

On the practical side, investigation of proton-deuteron capture reactions is expected to contribute to a better understanding of the few-body reaction mechanism, and therefore provide valuable insights into its mirror reaction: D(n,γ)T. This reaction is critical in the modulation process for nuclear reactors [Aus52]. Furthermore, thermal neutron captures in deuterium-rich materials have also been widely used for providing neutron shielding in many research and commercial areas such as radiotherapy in treating cancer patients[Kha84].

The present project is focused on the measurements of vector and tensor analyzing powers for both $^2H(\vec{p},\gamma)^3He$ and $^1H(\vec{d},\gamma)^3He$ at very low energies. The unpolarized total cross section for $^2H(p,\gamma)^3He$ is also extracted by averaging over the two incoming spin projections of the protons and allow the determination of astrophysical S-factors. These results are compared with those of the previous measurements and will provide additional constraints on the inputs to the stellar evolution calculations. All polarization observables are interpreted under the exact formalisms of three-body dynamics and realistic nucleon-nucleon potentials using most recent theoretical descriptions.

It is also worth mentioning that the present investigation of proton-deuteron capture reactions is conducted in parallel with the investigation of proton-deuteron elastic scattering at energies $E_{c.m.} \leq 200$ keV [Bla95]. The existing discrepency between the

calculated and the measured doublet scattering length may be due to the improper treatment of the Coulomb penetrabilities or the neglecting of long-range polarizability effects in the few-body calculations [Fri95].

In this Chapter 1, background and motivation for the present project will be discussed in the context of the three-body nuclear reaction theory and astrophysical significance. An overview of the previous work both theoretical and experimental will also be given. In Chapter 2 and 3, experimental techniques and instrumentation used in the present experiment will be described. In Chapter 4 and 5, Computational aspects of data analysis and mathematical modeling as well as the results of the experiment will be described. In Chapter 6, theoretical model calculations and comparisons with the experimental results will be discussed. Finally, conclusions and suggestions for the future work will be given in Chapter 7.

1.2 Radiative Capture Reaction

The field of photonuclear physics was first originated from a brief note in Nature by Chadwick and Goldhaber in 1934 [Cha34]. It was entitled "A Nuclear Photo Effect: Disintegration of Diplon by γ-rays". Their experiment set-up consisted of ionization chamber filled with deuterium gas, which was irradiated by 2.6 γ-rays from a radioactive source. The disintegrated proton signals were first observed then on an oscilloscope. Ever since then, photodisintegration and radiative capture reactions have been widely studied.

Radiative capture reactions are usually described either by a single step mechanism or a multi-step mechanism. In the single step picture or so-called direct capture model, incoming particles are directly "fused" together into the target nucleus. In the multi-step mechanism, interacting particles firstly break up into several segments or sub-structures, and then the reaction constituents rescatter and synthesize into a single bound state system.

Since the electromagnetic operator limits the number of the partial waves in the incoming channel, the radiative capture reaction has become a powerful tool in investigating both the initial continuum state and the final bound state wave functions of the nuclei [Eir91]. This is especially true at low energies since only a small number of leading partial waves exists here. In order to describe the full reaction mechanism, nucleon-nucleon contributions to the electromagnetic operators such as meson-exchange-current (MEC) must be included explicitly and treated carefully. This has already been proven not only in the radiative capture processes, but also in elastic scatterings, charge exchange and meson production processes [Fri90].

Moreover, when using eletromagnetic transitions as a probe, one must realize that it is only sensitive to the eletromagnetic structure of the target nuclei such as charge or current densities. If information is sought about the hadronic system involved, the charge or current density must be deduced in a model-dependent way. Since the photon can couple to each of the charged particles in the nucleus, including mesons, the microscopic treatment becomes very complicated in theory.

It is found that the so-called impulse approximation (IA), which neglects MEC effects, could not properly describe neither the cross section data nor the polarization observables for the low energy proton-deuteron capture reactions [Fon93]. The polarization observables have been shown to be particularly sensitive to the MEC effects and other small internal nucleon-nucleon contributions to the reaction mechanisms [Jou86].

Due to a small Coulomb penetrability, in the regime of low energy reactions, radiative capture processes are predominantly influenced by the asymptotic tails of the wave functions. These reactions therefore become an excellent testing place for the validity of the conventional long range Coulomb treatment in most realistic two-body *and* three-body nucleon-nucleon potentials. The peripheral nature of the reaction makes it especially sensitive to the small admixtures in the wave functions, such as D-state components in the tri-nucleon bound states [Bal87]. Since the electromagnetic process is well established in today's QED perturbation theory, radiative capture reactions are in general easier to deal with theoretically than the nuclear transfer reactions which study the same effects. As we know, the emitted γ-rays from the radiative captures are always immune to the distortions induced by the Coulomb field to the total Hamiltonian of the system.

In the present measurements of proton-deuteron capture reactions, the focus on the reaction dynamics aspects has been concentrated on the two major effects as described above, i.e., the MEC effects and the Coulomb effects. The theoretical treatment of the system dynamics has been purposely constrained within the domain of exact three-body

nuclear physics. The next two sections will briefly introduce the background for studying these two effects.

1.3 Meson-exchange-current effects

Mesons were firstly proposed and discovered in the early fifities as the medium carrying the strong force interaction. The idea for testing the exchange force effects in the few-body nucleon systems has been actively pursued and applied ever since. The apparent simplicity of the few-body system was expected to make it easier to pinpoint the reaction contributions from a specific intrinsic nuclear structure. The MEC effects have been since discovered and observed in several areas of few-body nuclear physics.

Historically, the first evidence for the meson exchange current effects was found in the static magnetic moments discrepancies between ^{3}H and ^{3}He [Ris84]. The mere inclusion of the meson exchange current corrections can compensate for as much as 60% of discrepancies resulting from the approach of taking the nucleons degrees of freedom into considerations in the calculations. It has been considered as one of the classic examples in the case of explaining the dependence of ^{3}H and ^{3}He magnetic form factors as a function of momentum transfer [Had86].

More relevantly, radiative capture of thermal neutrons on hydrogen, i.e. ^{1}H(n,γ)D reaction, was the one of the classic processes for which clear and convincing evidence was provided for the importance fo MEC. The cross section for the reaction was measured to be σ^{exp}=334 mb. While calculation from impulse approximation, which only nucleonic degrees of freedom was included, yielded a result of σ=303 mb. However, inclusion of

one-pion-exchange (OPE) gave a result of $\sigma = 335$ mb, which is in excellent agreement with the experiment [Ris72].

If we assume charge symmetry for nucleon-nucleon interactions in the electromagnetic process, it is expected that low energy $^2H(p,\gamma)^3He$ and $^1H(d,\gamma)^3He$ reactions considered in the present investigation should show a definite signature of MEC effects, especially in their polarization observables. After all, the MEC current operator is composed from none other than the combinations of the spin and isospin operators that satisfy the translational and gauge invariance (see Chapter 6 for details).

In the low energy proton-deuteron capture reactions, the incoming partial waves are primarily S and P waves, the electric dipole moment (E1) and magnetic dipole moment (M1) become the leading transition moments according to the selection rules(see Chapter 6 for details). Since electric multipole (EL) transition is about several orders of magnitude stronger than its corresponding magnetic multipole (ML) transitions [Jac74], E1 transitions should dominate the proton-deuteron capture process. Nonetheless, M1 transition matrix elements still plays an important role in describing the angular distributions of the reaction's cross section and even more so, the polarization observables. The M1 contribution manifests itself more explicitly in the extreme forward and backward angles, since at these angles E1 contributions diminish very quickly as it is governed by the $\sin^2\theta$ distribution, where θ is the angle between the radiation transverse axis and the beam direction.

Meson-exchange-current is directly sensitive to the M1 transitions rather than the E1 transitions. This postulation was first proved by Siegert under the well known Siegert

Theorem [Sie37], which states that for EL transitions the total charge density can be completely described by the nucleon charge density operator in the ideal point charge situation or under the so-called long wave approximation, which is very good one for most nonrelativistic photonuclear reactions. This can be seen most explicitly in the $^2H(n,\gamma)^3H$ reaction, which is almost entirely governed by the M1 transitions. Simply turning off the MEC parts in electromagnetic operator can lower the predicted total cross section by as much as a factor of 2 at the thermal energies [Tor84].

The Siegert Theorem is particularly true for the low energy proton-deuteron capture reactions. The exchange charge density simply vanishes for E1 transitions in the reaction mechanism. However, the total magnetic dipole moment must include the additional terms caused by the exchange currents among all the reacting nucleons. This exchange effects are expected to be very important in determining the M1 transitions present in our reactions.

In this project, full angular distributions of the polarization observables i.e. iT_{11}, T_{20} and T_{22} are measured. From these observables, the MEC contributions to the complete reaction dynamics could be traced. Since M2 and E2 contributions are considerably smaller in the proton-deuteron captures from the power scaling law [Jac74], they are usually truncated in the theoretical calculations. The mere inclusion of one higher order transition operator such as E2 or M2 still presents a big challenge in today's *exact* three-body nuclear physics [Leh94].

1.4 Three-body ^{3}He wave function

Recent experimental efforts have pushed the determined observables to such a precsion that even small components in the wave function of the bound state of ^{3}He must be taken into account. To generate such a wave function, three- body Schrödinger equation must be solved. One obvious approach is to find correct potential operators in the total system Hamitonian, which could realistically describe the two-body nucleon-nucleon interactions with some add-on terms correcting for three-body effects. This idea is justified by the small magnitude of three-body effects. Even without any three-body terms, the present two-body nucleon-nucleon potential models already enjoy a great success in explaining many effects in nuclear physics. One dazzling example is the shell model originating from the L-S coupling term in the two-body potentials.

The ^{3}He wave function can be constructed from a two-body potential simply by assuming that ^{3}He consists of one proton and one deuteron particle. Such a microscopic construction is the foundation for the resonating group model (RGM), which will be discussed in detail in Chapter 6.

Unfortunately, even in the frame of two-body potential, many questions still persist, e.g., the precise correlation between the ^{3}He D-state probability and tensor strength in proton-deuteron capture reactions are not clearly understood [Arr83]. More seriously, no wave function generated from a two-body potential which well describes the nucleon-nucleon scatterings could adequately reproduce the binding energies of ^{3}He and ^{3}H that are consistent with the experimental values. It has been realized ealy on that new models incorporating three- body effects must be used to solve these problems [Ber86]. With a rapid advancement in the super computer's power, detailed three-body calculations

are becoming feasible only within last several years. Results have shown that ^{3}He bound-state wave function generated from such potentials could effectively account for some of the differences in tri-nucleon binding energies but discrepancies still exist [Fon93]. More efforts are still needed in order to calculate *exactly* the proton-deuteron doublet scattering lengths and their correlations with tri-nucleon binding energies.

The measurements of proton-deuteron capture reactions could serve as an important tests for such realistic ^{3}He wave functions. A very recent experiment had found that ^{3}He wave function generated from the two-pion-exchange (TPE), three-body potentials could not adequately describe the tensor analyzing powers of ^{1}H($\vec{d}$,γ)^{3}He at 17.5 MeV [Sag94]. More examinations both theoretically and experimentally should be further pursued to improve the present full three-body ^{3}He wave functions.

One major motivation for carrying out this project is that the polarization observables especially tensor analyzing powers for ^{1}H($\vec{d}$,γ)^{3}He at reaction energies below 200 keV do not exist. Measuring such observables should impose a strong constraint on the three-body ^{3}He wave function and effectively elucidate the low energy radiative capture reaction mechanism.

1.5 Coulomb effects

As it is known, the Coulomb interaction in the two-body Schrödinger equation can be solved exactly by using its exponentially screened form, which purposely removes the singularity of 1/r behavior when r goes to zero. However, the long range nature of the Coulomb field has presented a serious challenge in solving the exact three-body

Schrödinger equations. In a popular treatment, Coulomb effects are simply approximated by an energy shift or an overall normalization. Since in most scattering processes, Coulomb field simply "slows down" the incoming projectiles and shifts the reaction energy. The comparison of n-d and p-d elastic scattering data seem to justify such a treatment and the idea behind this has been applied to probing the charge symmetry breaking effects [Glö90].

The first inclusion of the Coulomb field in the three-body treatment was tested recently in the proton-deuteron breakup analysis [Alt78]. Since the three-body effects are much smaller comparing to any two-body Coulomb interactions from the power counting law by Weinberg [Wei92], any approximations made in the Coulomb treatment should cast a great shadow over their final predictions. The exact treatment of the Coulomb field must be pursued rigorously in order to go beyond any two-body interaction model, especially the effect is coupled with the validity of ^{3}He wave functions.

It has been found that the Coulomb field can effectively influence the asymptotic behavior of the ^{3}He wave function [Fri88]. It had been argued that in the low energy proton-deuteron capture, the asymptotic tail of the wave function plays an important role in the final analysis of the polarization observables. A test by Berthold *et al.* clearly confirmed the importance of the Coulomb effects [Ber88]. In their test, both neutron-deuteron capture and proton-deuteron capture reactions are compared and it was concluded that Coulomb corrections must be properly included in order to resolve the analyzing power data at the center of mass reaction energy of 1.7 MeV. In the present measurements, the reaction energy is much lower than 1.7 MeV, thus the Coulomb

penetrability is even smaller for the incoming projectiles. This makes the precise treatment of Coulomb interaction even more necessary in our final interpretation of the data. From this point of view, probing Coulomb effects could be deemed as another goal of this project.

Another aspects of Coulomb effects is that they are also the cross-link between p-d capture and mirror n-d capture reactions. Understanding such effects could probably produce more information on the charge symmetry in the electromagnetic interaction processes. A recent calculation based impulse approximation within the framework of the three-body approach has indicated that Coulomb distortion could dramatically affect the M1 cross sections for proton-deuteron capture reactions at zero reaction energy [Kha92]. It was concluded that Coulomb distortion both in the entrance and exit channels leads to a considerable increase in the reaction astophysical S-factor comparing with the mirror neutron-deuteron capture - almost twofold from the contribution of the doublet state and almost fourfold from the quartet state. The precise calculation and the measurement of the astrophysical S-factor for proton-deuteron capture reaction carries a great importance in determine star evolution and nucleosynthesis. This leads us to the next discussion on the astrophysical significance of radiative proton-deuteron captures.

1.6 Astrophysical Significance

The astrophysical importance of proton-deuteron capture reactions could be dated back to the birth of astrophysics itself. All of the astrophysics can be said to originate from our ideas regarding the nature of stars and their evolution [Cla83]. With the

explosive development in nuclear physics and the quantum theory at the beginning of this century, people began to realize that nuclear reactions are directly linked to the questions about the origin and the history of the universe. The standard model of star evolution developed during the process had proven that the energy of the stars predominantly comes from the thermo-nuclear reactions rather than from the other sources. In a even broader sense, they are the sole reason for the existence of stars. Since it is the power and the pressure generated from such nuclear reactions that counterbalanced the gravitational contractions of the stars to form a singular black hole.

Up to now, a general picture of the nucleosynthesis has been developed based on tremendous experimental evidence and observations. Traditionally, the whole picture is divided into a series of major processes that have taken place in accordance with the natural formation of a star. The first process is the hydrogen burning in which helium is produced, then helium burns to produce carbon, neon, oxygen etc. Next in the process of the C-N-O cycle, carbon, nitrogen, and oxygen react and medium heavy elements such as silicon are generated. Finally, undergoing silicon burning process and the s-, r-, p-, processes, all the heavy elements on a star are produced. The other exotic reactive light elements such as ^{6}Li, ^{7}Be, and ^{8}B can be produced through so-called l-process [Rol88].

Hydrogen burning process can be summarized as a catalyzed reaction in which four protons generate one helium,

$$4p \rightarrow {}^{3}He + 2e^{+} + 2\nu$$

This reaction can be achieved through several reaction chains. They are traditionally labeled as the P-P chain in hydrogen burning process as illustrated in Figure 1.1.

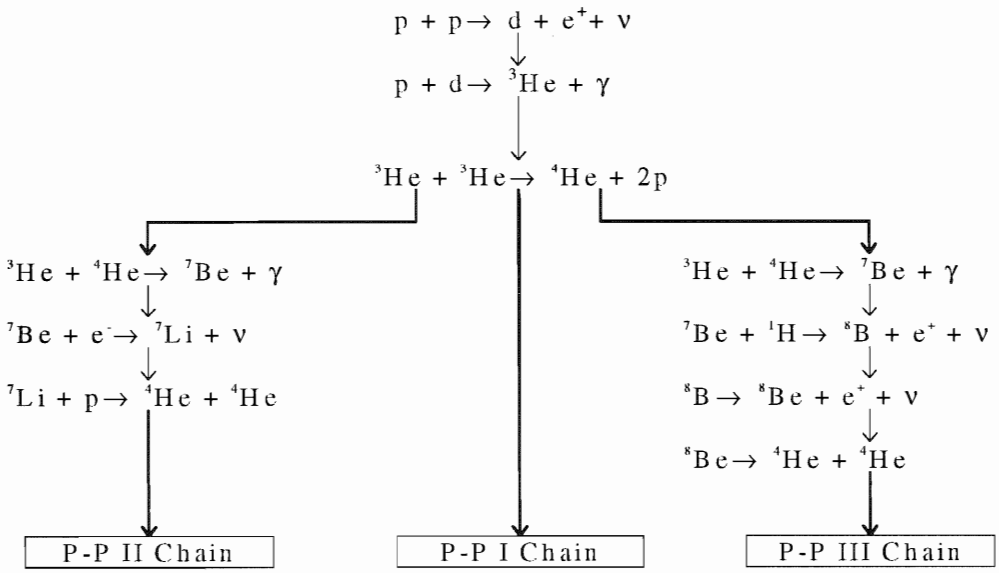

Figure 1.1 The flow chart of P-P chain reactions.

As it is shown in Figure 1.1, radiative proton-deuteron capture reaction is the "bottle-neck" reaction leading to all three proton-proton chain reactions. It has been widely accepted as the first thermal nuclear reaction to occur in the formation of a protostar as it has the lowest Coulomb barrier among all the radiative capture reactions.

Due to the fact that the life time of deuteron is much shorter than proton during the p-p chain burining process, the proton-deuteron radiative capture becomes the primary deuterium destruction reaction in a star [Par64]. The primordial abundance ratio between deuterium and hydrogen can be directly calculated through the reaction rate of all the deuterium-related thermo-nuclear reactions.

The interstellar rate for a nuclear reaction in an early star is calculated from the following equation,

$$\langle \sigma v \rangle = \int \phi(v) \sigma v dv \qquad (1.1)$$

where σ is the total reaction cross section, v is relative velocity between the interacting nuclei, and $\phi(v)$ is the velocity distribution in the form of Maxwell-Boltzmann distribution with the assumption that the stellar gas is non-degenerated.

The calculated primordial ratio between deuterium and hydrogen abundance yields a result around 10^{-17} (see reference [Rof88]). This value is far less than the terrestrial value of 10^{-4} obtained from sea water. The reason for such a difference has not yet been completely understood. It is however believed that terrestrial deuterium could not have been coming from the primordial leftovers [Fow62].

To describe the energy dependence of σ in Equation 1.1, the astrophysical S-factor is generally introduced. It is defined as,

$$S(E) = \sigma(E)\, E \exp(2\pi\eta) \qquad (1.2)$$

where η is Sommerfeld parameter ($\eta = Z_1 Z_2 e^2/\hbar v$). It can be seen that S-factor is just the total cross section scaled by kinematic factor (De Broglie wave length) and the Coulomb penetrability function. Even though Equation 1.2 is just another representation of the total cross section, it serves an important practical purposes in calculating nuclear reaction rate.

In most cases, star temperature in the standard model calculation is around 10^7 Kelvin, which corresponds to a reaction energy that is below the experimental detection limit (note that 10 keV $\approx 10^7$ Kelvin). Therefore, it is necessary to extrapolate the total cross sections of interest from those measured at much higher energies. Direct extrapolation of total cross section data are vulnerable to big subjective errors in its scaling procedures. By separating large Coulomb dependence, S-factor is expected to be

a slowly varying function of energy for all non-resonant reactions. Such a slow varying behavior can be well described by the leading terms in its Maclaurin expansions. As for the proton-deuteron capture reactions, the first order expansion is normally sufficient.

Some caution should be taken before extracting S-factor at zero energy S(0). First of all, the energy dependence of the S-factor should be studied over a wide range of energies before reliable extrapolations can be made even in the case of the non-resonant reactions. It is known that S-wave, P-wave or D-wave captures yield different energy dependence of S-factors. If only S-waves are present, we would have obtained S(0) by just *one* single measurement since it is constant. However some experimental work had shown that even at very low energies, P-wave capture still represents a large fraction of total capture strength, even up to 90% in some reactions [Kra92]. More data points at different energies are always necessary in order to constrain the extrapolation. The presence of higher partial waves can be easily observed in the analyzing power measurements. If only S-wave presented, the analyzing powers should be identically zero.

Additionally, it is necessary to have the knowledge of relative strengths between electric dipole (E1) and magnetic dipole (M1) transitions for proton-deuteron captures in order to precisely describe the angular distribution of the cross sections. As it is known, the shape of the angular distribution can be directly influenced by different multipole strength present in the reaction. From this point of view, understanding different contributions from all the multipole transitions, especially M1 contributions in proton-deuteron capture reactions could have a great astrophysical significance.

1.7 Review of the Experimental Work

The first series of measurements for proton captured on deuteron below 1 MeV were performed by G.M. Griffiths and G.M. Bailey about thirty years ago [Gri55], [Gri62], [Gri63], [Bai70]. In these experiments, a large volume sodium iodide (NaI) scintillators were used as the γ-ray detectors and a thick heavy ice (D_2O) was used as the target. The total cross section and S-factors from this set of data covered an energy range from 16 keV to about 2 MeV in the center of the mass frame. The theoretical work associated with these measurements by Donnelly had further proved that $^{2}H(p,\gamma)^{3}He$ is a non-resonant capture reaction [Don64].

The extrapolated energy dependence of the S-factor from this set of measurements has been regarded as the standard for all the astrophysical model calculations. However, a recent repeated measurement by Schmid *et al* [Sch95a] at the reaction center of mass energy below 55 keV had indicated that Griffiths' data considerably underestimated the error in target thickness, and the S-factor could have been overestimated by as much as 40%. One major improvement of this recent measurement over the previous ones is that high resolution HPGe γ-ray detector was used. Clearly, the new result merits further investigation over a larger sets of data and the measurements of the total cross section in the present thesis project will hopefully contribute to this purpose.

At energies above 1 MeV, there have been a moderate number of measurements for either $^{2}H(p,\gamma)^{3}He$ or $^{1}H(d,\gamma)^{3}He$ reactions. Since these measurements, especially those of the polarization observables, are directly related to the issue of the ^{3}He wave functions and their D-state components, a brief summary of most important work will be given here.

Jourdan et al. [Jou86] measured the $A_{yy}(\theta_{lab}= 90^{o})$ for $^{1}H(d,\gamma)^{3}He$ at E_d = 29.2 MeV and 45.3 MeV. Their results showed that D-state wave function of ^{3}He in the region of 2-5 fm is 20% smaller than that predicted by Reid soft-core nucleon-nucleon potential. They also found that E1 transition dominates the reaction mechanism and meson-exchange-current effects at both energies are relative small.

A TUNL group measured the full angular distributions of cross sections and vector analyzing powers for $^{2}H(p,\gamma)^{3}He$ reaction over the excitation energy region of 6-15 MeV. The measured angular distribution was fitted by a Legendre series with the focus on extracting the coefficients which are sensitive to the D-state component of ^{3}He. It was found that M1 strength could not be neglected in explaining near threshold captures [Kin83], [Kin84]. Another measurement [Vet85] of T_{20} for $^{1}H(d,\gamma)^{3}He$ reaction at a deuteron lab energy of 19.8 MeV clearly indicated the presence of D-state effects in ^{3}He wave function, although strong model dependence made the determination of D-state probabilities impossible. It was found however that the measured T_{20} has a small negative value(~ -0.07) instead of zero, as predicted for a pure S-state ^{3}He wave function.

A more recent experiment [Goe92] determined the cross sections and polarization complete sets of observables for both $^{1}H(d,\gamma)^{3}He$ and $^{2}H(p,\gamma)^{3}He$ reactions at center of mass energy of 3.33 MeV. The data placed a very strong constraints on all direct matrix elements especially on the spin-flip E1 components. The highest reaction energies measured so far for proton-deuteron capture reactions have reached the deuteron energy of 95 MeV [Pit88], and the proton energies of 99.1 MeV, 150.3 MeV and 200.7 MeV

[Pic87]. The authors for these measurements had argued that in order to account for the observed angular distributions of vector and tensor analyzing powers, a full three-body calculation with inclusion of E2 radiation multipole is necessary.

1.8 Review of the Theoretical Work

The early theoretical investigations of $^{2}H(p,\gamma)^{3}He$ reaction were performed at the same time of the Griffiths experiments. Much of the effort in explaining the cross section data had concentrated on the two-body formalism. In most calculations, the incoming scattering states were approximated by plane waves or distorted plane waves. The electromagnetic operator did not include any of the meson-exchange-currents. Since the effective two-body potential models even with the inclusion of Coulomb field can be separated and treated in a quite straightforward form, the Schrödinger equations were solved exactly in most cases. This two-body model had shown some degree of success in explaining the cross section data [Wöl66]. However, the work by Jourdan [Jou86]as mentioned above clearly indicated the necessity for exact three-body dynamics and inclusion of MEC effects in the theoretical calculations for the interpretation of tensor analyzing powers for $^{1}H(d,\gamma)^{3}He$. This is the isssue that we would like concentrate on in our next discussions.

In the area of exact three-body dynamics, the first breakthrough for calculations of photodisintegration of ^{3}He (the inverse reaction of proton-deuteron capture reactions) was achieved in 1967. Barbour and Phillips [Bar67] first used the Faddeev expansion techniques [Fad67] to solve the three-particle equations. The wave function for ^{3}He was in

the empirical form but the continuum states and three particle unitarity were treated exactly. Later studies by Gibson and Lehman [Gib76] effectively treated the rescattering states from the three-body channel to the two-body channel. A recent paper by Fonseca and Lehman [Fon91] has found that the exact three-body dynamics is essential for interpreting the magnitude of the polarization observables in $^{1}H(d,\gamma)^{3}He$ reaction, and that the D-state component in ^{3}He wave function is totally responsible for the behaviors of the tensor analyzing powers. In order to separate the model dependence for various calculation methods and test the sensitivity of the three-body force in various potentials, Ishikawa and Sasakawa performed calculations using seven available nucleon-nucleon potentials with and without three-body nucleon force [Ish92]. They found that Argonne-V14 potential [Wir84] with inclusion of three-body-force can best fit the existing observables for proton-deuteron captures. All of the above theoretical work had been concentrated on the reaction energy above 1 MeV where the polarization observables had been measured. The electromagnetic operators used were typically long-wave Siegert E1 and E2 operators. Therefore the inclusion of meson-exchange-currents operators in the calculation was largely overshadowed or simply disregarded. As it has been discussed previously, we expect M1 transition and thus MEC effects play an important role in explaining any low energy polarization data. The inclusion of these effects in any theoretical model calculations has become the major criteria for any comparisons with the experimental data.

Many methods have been developed for performing full dynamic calculations with inclusion of MEC effects either in the configuration space or in the momentum space. For

the relevance to the present work, two successful models will be introduced: the Resonating Group Model (RGM) and variational Correlated Hyperspherical Harmonics expansion method (CHH) [Car88], [Viv95].

The Resonating Group model was first proposed in a 1937 paper by John Wheeler on atomic physics [Whe37]. Since then, it has been reconstructed and developed for nuclear physics applications at the University of Erlangen in Germany [Hof86]. Although RGM is a two-body model, the microscopic nature of the model has been very successful in explaining many properties of few body systems [Sch91]. Attempts had already been made to successfully incorporate the meson-exchange-current effects into the model. The calculated results are in excellent agreement with some high energy data for proton-deuteron captures and other photo-nuclear reactions [Web92].

A very recent direct cluster model calculation using essentially RRGM formalism but different nucleon-nucleon potentials has been performed by Dubovichenko [Dub95]. It has shown that the total cross sections for ^{3}H(γ, n)d, ^{3}He(γ, p)d could be successfully described. The astrophysical S-factor considering only E1 transition in ^{2}H(p,γ)^{3}He is also calculated and has been found to agree very well with the Griffith data [Gri63]. This caluclation will also be used to compare with the present measurements in Chapter 6.

The CHH calculation is a relatively new method derived in the context of full three-body and even four-body nuclear physics. It has so far achieved quite remarkable agreements with experimental results. It has been tested against all the other popular methods in the same areas e.g. the Faddeev-Yakubovsky (FY) method [Fad67], Variational Monte Carlo method (VMC) [Car85], etc. The method itself embodies a full

three-body or four-body method constructed by exactly solving Schrödinger equation. There are no free parameters in this model and both initial and final state interactions are treated completely under the calculation.

The bound state tri-nucleon eigenfunctions are calculated by using variational principles. Both ^{3}H and ^{4}He binding energies are reproduced exactly by this method. The meson-exchange-current operators are also included in the CHH model.

The Coulomb field is treated exactly in both RGM and CHH calculations unlike in many other methods. These two models will be examined in more details later in Chapter 6. Up to now, major theoretical challenges are still present in determining and separating the few-body force effects in the nucleon-nucleon field. The study of the electromagnetic process including the current project could hopefully contribute to the theoretical progress for a better understanding of few-body systems.

II. Instrumentation Developments and Techniques

2.0 Overview

Since the cross sections for low energy proton-deuteron capture reactions are in the sub-microbarn region, a great deal of experimental and technical efforts have been invested to make the present experiment productive. For a proper detection yield, high target density, high beam intensity and high detector efficiency are needed. Most important of all, ratio of true events to backgrounds and the dark noise from detection systems should be minimized as much as possible.

In this chapter, discussions will be concentrated on how to meet all these challenges. The TUNL Atomic Beam Polarized Ion Source (ABPIS) and Low Energy Beam Accelerator Facility (LEBAF) are introduced first. Then techniques of targets fabrication and results of on-line analysis are described. Finally, design and performance of two detection systems, i.e. BaF_2 Scintillator and High Purity Germanium Detector, are reviewed.

2.1 TUNL Polarized Ion Source

TUNL Polarized Ion source (see Figure 2.1) is capable of producing more than 40 μA of polarized positive proton or 10 μA of polarized positive deuteron beam. It consists of four major sections: dissociation section, state transition and nuclear polarization optimization section, ionization charge-exchange section, and spin filter section.

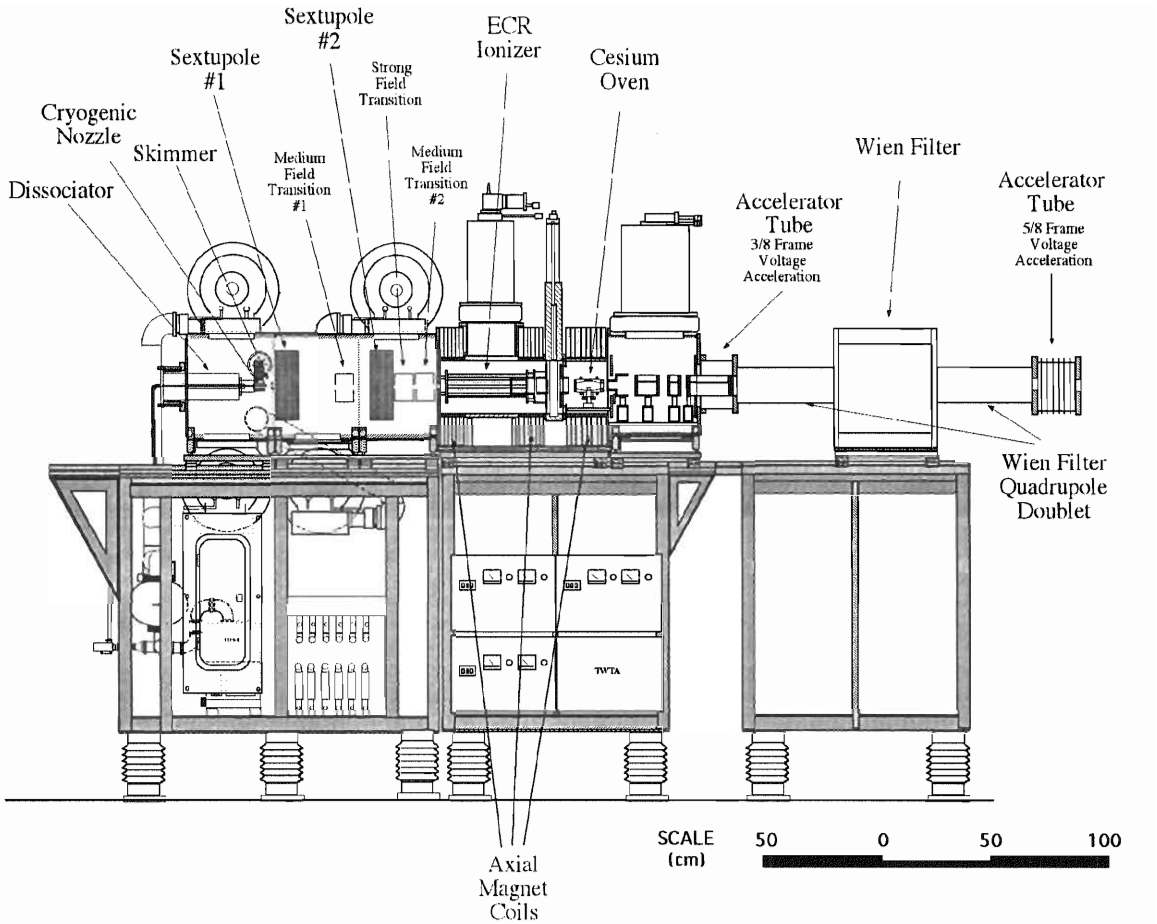

Figure 2.1 The schematic drawing of TUNL Atomic Beam Polarized Ion Source (ABPIS) [Cle93].

In the dissociator, neutral atomic beam is generated. Hydrogen or deuterium gas molecules are disunited in a Pyrex glass tube through an intense Radio Frequency (RF) field. The discharged atoms are streamed down a copper pipe with a small nozzle. The nozzle is kept cooled at about 30° Kelvin by a close-cycle Helium refrigerator. This low temperature can effectively slow down an atom and thus reduce its chance of

recombination. The whole section is continously buffered with pure nitrogen gas for the same purpose.

The hydrogen or deuterium atom is polarized in nuclear spins by a combination of sextupole magnets and RF transition units as shown in Figure 2.1. The sextupole magnets are cylindrically symmetric. Their magnetic fields are inhomogeneous along the radial direction. When an atom travels through the sextupole's inhomogenous center field, it experiences a magnetic force that is given by

$$\boldsymbol{F} = \nabla(\mu \cdot \boldsymbol{B}) \qquad (2.1)$$

where μ is the spin magnetic moment.

Since F in Equation 2.1 is spin dependent, it is capable of polarizing the beam in electron spins[Cle93]. After the sextupole, three consecutive RF transition units are used to polarize the beam in nuclear spins through nuclear hyperfine interactions and substates transitions. The Breit-Rabi diagrams, as shown in Figure 2.2, are conventionally used for labeling nuclear hyperfine substates.

The separations between any two substates (e.g. state 1 and state 3) are determined by the external magnetic field. Transitions between two nuclear substates can occur only if they satisfy the spin parity selection rules, i.e. $\Delta m_j = 0, \pm 1$. After desired transitions, certain fractions of nuclear substates are populated. The atomic beam thus become nuclear polarized. Typical settings for different state transitions have been listed in the Table 2.1.

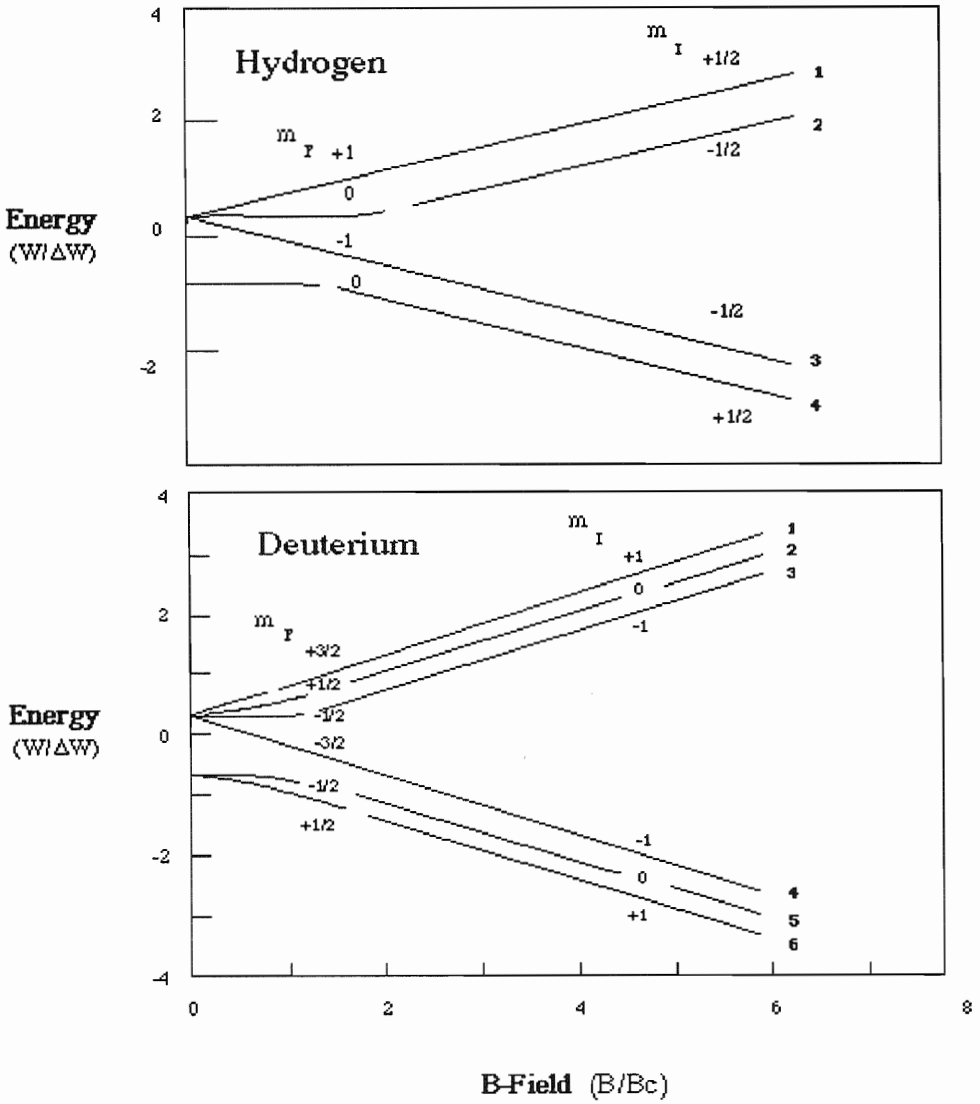

Figure 2.2 Breit-Rabi diagrams for hydrogen and deuterium atoms as a function of magnetic field. The B_c is critical external magnetic field and ΔW is character frequency.

The working definitions for vector polarization and tensor polarization is given as

$$\begin{cases} P_z = N^+ - N^- \\ P_{zz} = 1 - 3N^0 \end{cases} \quad \text{if } N^+ + N^- + N^0 = 1 \qquad (2.2)$$

where N^+, N^-, N^0 are the number fractions of particles occupying the nuclear substates of m_j=+1, 1, and 0, respectively for deuterium, or only N^+ , N^- for hydrogen occupying m_j=+1/2, and −1/2 separately (see Figure 2.2 for illustration). In theory, vector polarization or tensor polarization is identified by its spin matrix components along their eigenvector's direction, which is usually taken to be the direction of beam momentum. The calculated P_z and P_{zz} in Equation 2.4 are just the observation values of the spin matrices over the ensemble of entire beam particles.

Transition Unit	Particle	f (MHz)	B (mT)	Transition
MF1	H_0	12	0.4	1→3
	D_0	12	1.2	1→4
SF2	H_0	1485	16.0	1→4
	D_0	460	16.0	3→5
MF2	H_0	12	0.4	1→3
	D_0	28	2.6	2→4

Table 2.1 Transition units settings used for obtaining vector and tensor polarized proton and deuteron beams. The combination of SF2 and MF2 units can be used for one fast spin-flipping scheme.

In this project, we only used the second Strong Field (SF2) transition unit and the second Medium Field (MF2) transition unit. For proton beam, SF2 and sextupole

magnets produce a vector polarization $P_z = +1$, which is often referred as "spin-up". Similarly, MF2 and sextupole magnets produce proton beam with $P_z = -1$, which is often referred as "spin-down".

For deuteron beam, SF2 transitions eventually produc a polarized deuteron beam with $P_{zz} = -1$ and $P_z = +1/3$ and similiarly, MF2 with $P_{zz} = +1$ and $P_z = -1/3$. The reason for choosing MF2 and SF2 together in our measurement is the so-called fast "spin-flipping" scheme. As it can be seen, P_z and P_{zz} values for MF2 transition are just in opposite signs with those of SF2. Therefore by simply switching on and off SF2 and MF2 in a desired sequence, we can effectively change the signs of both P_z and P_{zz} simultaneously. This is equivalent to flipping the direction of spins during the measurement. The detailed implementation of the scheme will be discussed in the next chapter.

It should be noted however that optimizing tensor polarization does not mean optimization of the vector polarization and vice versa. This can be seen from the implementation of the above MF2 transition unit. In this case, P_{zz} is maximized at its value of $P_{zz}^{max} = +1$, whereas P_z is only one third of the maximum value that can be achieved from its definition in Equation 2.4 (i.e. $P_z^{max} = -1$),.

In the third section of the source after the spin state transition units, nuclear polarized neutral atoms are ionized in the Electron-Cyclotron-Resonance (ECR) Ionizer. They are going through an intense plasma region maintained by microwave radiation. The spatial constraint of the plasma is set by an axial magnetic field from a DC solenoid. The hydrogen or deuterium coming out of the plasma is stripped of its electron and become

positive. The charged beam can then be extracted by a six-lens focusing system placed after the ECR Ionizer. If negative beam is wanted, positive ions are sent through a charge exchange canal. In the canal, Cesium vapor permeates the traveling path of the ions. The vapor is created by heating Cesium metal in an oven heater controlled by a temperature feedback. Incoming positive ions can pick up two extra electrons from the Cesium vapor to becomes negatively charged. The electrostatic field directions of the last two lenses can be easily reversed for accelerating either positive or negative ions. The frame voltage applied over the final sections of the ABPIS is capable of accelerating beam up the energy of 80 keV.

In the final section of the source, the spin direction of the beam can be rotated. Initially, the quantum axis of the spin is set by ECR's axial magnetic field. In order to send a beam to a designated target chamber, several bending magnets have been used in the following beam transporting systems. Since spin angular momentum can undergo Lamar precession in an external magnetic field, compensation has to be made for such a spin rotation. The angle after a precession is proportional to the total bending angle of the magnet. This bending angle is largely determined by the field strength of a magnet. Therefore, we can counter-rotate the total procession angle by a correcting B-field applied before polarized ions are injected into this magnet. Such a B-field is naturally attached to the last section of the source.

The strength of the B-field is selected so that it rotates the spin axis to a direction that cancels the angle precessed by *all* the inflection magnets. In order to keep the beam traveling straight in this B-field, a vertical E-field is also applied to cancel the spin torque

that is equal to $\mu \times \mathbf{B}$. The final $\mathbf{E} \times \mathbf{B}$ points to the direction where ions are traveling. Such a "spin-filter" device is called Wien filter named after its inventor. After the Wien filter, the spin axis of the beam is uniquely aligned with its B-field direction. After passing through a master bending magnet, the polarized beam is sent into the LEBAF transporting system.

2.2 TUNL Low Energy Beam Accelerator Facility (LEBAF)

TUNL LEBAF is used for studying nuclear reactions at energies up to 680 keV. It incorporates a minitandem accelerator that is capable of accelerating negative proton or deuteron beam up to 500 keV [Bla93]. It complements the existing TUNL Van de Graaff tandem accelerator, which has a terminal voltage of 10 MeV. The main section of the beam line was designed and built between 1991 and 1992. Besides minitandem accelerator, LEBAF consists of two Y-shape branched beam lines (see Figure 2.3). One bends the beam 40° to the rightside and the other one bends it 45° to the leftside. The measurements of proton-deuteron capture reactions were conducted on the right-side 40° beam line.

In this chapter, minitandem accelerator and its associated beam transporting systems are discussed. The reaction chamber and vacuum system are also presented. The design for the reaction chamber especially the implementation of high vacuum system is very important for making vapor condensed target used in our experiments. The detailed discussions on target making will be introduced in the last section of this chapter.

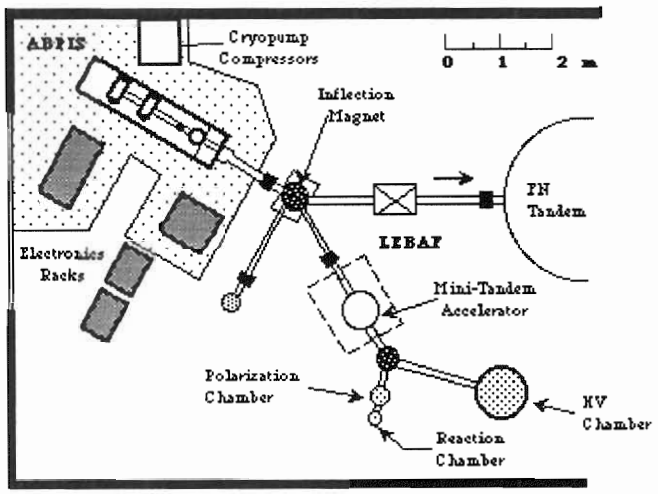

Figure 2.3 The layout for TUNL low energy bay with LEBAF setup.

2.3 Beam Transport System and Minitandem Accelerator

As shown in Figure 2.3, primary beam line of LEBAF is extended to the rightside of an inflection magnet right after the Wien filter. Polarized ions from the source at energy of 80 keV are first focused in an electrostatic quadrupole triplet. A pair of magnetic coil steerers is installed to steer the beam both horizontally and vertically. After a limiting slits, beam is injected into minitandem.

The minitandem first accelerates the beam up to 280 keV by a 200 kV terminal potential applied through a Spellman high voltage power supply. The 280 keV negative ion beam at the terminal is intercepted by a thin carbon foil which strips a negative ion of two extra electrons to make it positive. The resulting positive ions are accelerated again by the same 200 kV electrostatic field. The similar principle is being applied to the Van de Graff tandem accelerator.

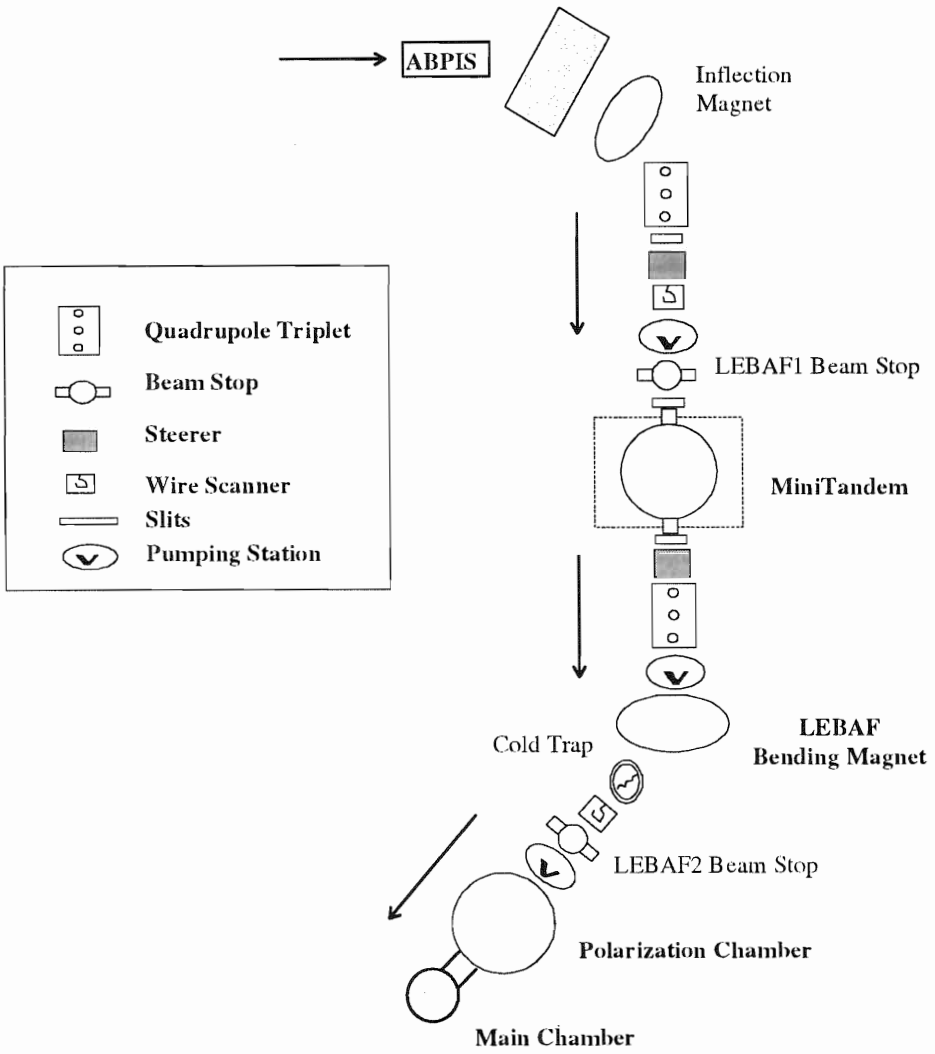

Figure 2.4 Detailed layout of TUNL Low Energy Beam Accelerator Facilities (LEBAF). The arrow indicates the beam traveling direction.

A manual carbon foil changer is used to select and to change carbon foils inside the minitandem chamber. The thickness of the carbon foil can vary from 1 $\mu g/cm^2$ to 3 $\mu g/cm^2$ depending on experimental requirements. It is from experience that foil thickness that is greater than 3 $\mu g/cm^2$ will greatly reduce the beam transmission efficiency. Foils of

thickness less than 1 $\mu g/cm^2$ foil are not durable enough for a beam current of 10 μA or larger. Floating delicate foils that are less than 1 $\mu g/cm^2$ thick has also become very difficult. Nevertheless, if energy loss in a stripping foil becomes a concern for the experiment, 1 $\mu g/cm^2$ foil is normally used. The whole minitandem assembly is made from polished Aluminum. It is interlocked electronically with the surrounding safety fences.

A question arises about using of carbon stripping foil for transmitting polarized beam. How large is the depolarization effect ? Similar question was investigated for high energy Van de Graff tandem accelerator. The role of carbon stripping foil has been studied since the very beginning of the accelerator engineering [Bok69]. For energy above 1 MeV, depolarization effects was found to be negligible. This can also be seen from comparison of the polarization of injecting source and the polarization measured from nuclear reactions in the scattering chamber. In the low energy region, beam polarization can be determined using reactions such as $^3He(d,p)^4He$, which yields good polarization standard. The results are compared with polarization measurement made at higher energies where well calibrated polarimeters exist. It has been found that even for low energy beam, depolarization for beam through the minitandem carbon foil is negligible within statistical errors.

After passing through minitandem, beam is calibrated by the object slits. It is refocussed by another quadrupole triplet lens. The beam is then bent by 40° to the right-side beam line, where the $^2H(p,\gamma)^3He$ and $^1H(d,\gamma)^3He$ reactions were measured in this project. The beam line consists of a cold trap, a beam image wire scanner and a pair of coil steerers. Along the entire beam line, there are also several beam stops installed to

measure the beam current effectively and accurately. The beam transmission efficiency from LEBAF1 beam stop to the reaction chamber is typically 30%. The typical beam current measured during on-line experiment is shown in Table 2.2.

The vacuum and power of the whole system are automatically interlocked with several isolation gate valves to protect them against accidents or failures. This is specially important when high voltage has been switched on for the minitandem supplies.

Beam stop positions	Integrated beam current (μA)
ABPIS Source	10
LEBAF1	8
LEBAF2	5
Target	2-3

Table 2.2 Typical values of beam current along TUNL LEBAF beam line.

The final reaction was measured in a two scattering chambers that are chained together (see Figure 2.3). The first chamber serves the purpose of monitoring beam polarization. In the second one, vapor-condensing target is placed.

2.4 Scattering Chamber Design

The first scattering chamber used in the present experiment was originally designed and built by K. Fletcher [Fle92]. It has 50 cm in diameter and 15 cm in height. Its bottom

is clamped onto a 2,200 liter/second turbo molecular pump. The top and bottom plates are grooved and collared for mounting surface barrier solid state detectors.

A target rod can be inserted into the top plate of the chamber. The target rod was vacuum sealed by double O-rings along its moving path. When polarization measurements were carried out during the present experiment, the target rod was lowered into the chamber to intercept the beam and detectors were rotated into the necessary angular settings for the measurement. Large size of implanted ^{3}He targets were used. Chamber collars had been modified so that the target rod could be lifted up to clear the beam path after the measurement.

The second chamber is attached to the zero-degree port of the primary chamber. The connecting pipe line is about 60 cm long and 11 cm in diameter. The chamber itself is 9.1 cm in diameter and 18 cm in height. The outside aluminum wall is only 0.5 cm in thickness for the purpose of reducing the attenuation for outgoing γ-rays passing through the wall.

The bottom part of the chamber has a beam stop aligned at zero degree. A cushion bellow is controlled electronically for pushing the beam stop in and out. This beam stop measures the beam current right in front of the target. This enabled beam current to be easily tuned for maximizing beam current on target.

The chamber top can be fitted with either a vapor condensing dewar or a solid target mounting assembly. The vapor condensing dewar will be discussed in the following section. The solid target mounting assembly together with the chamber over view are shown in Figure 2.5.

Since the precise measurement of beam integration on the target is necessary, care should be taken to isolate the whole chamber from any other conducting pipe or metal supporting stand. Both incoming and exiting ports of the chamber and bottom plate are isolated by double Delrin connections and plastic supporting discs. The chamber can be cleanly grounded or correctly biased to ensure the accurate beam integration. The target rod itself is usually biased to a positive 90 Volts by DC batteries. This is intended for suppressing scattered electrons originating from the beam hitting the target rod.

A beam current integrator is used to measure the total accumulated charges. The signal is digitized by the integrator and then sent to a computer scalar interface. The current integrator used in the present work is manufactured by Brookhaven Instrument Corporation, which has been calibrated commercially within 0.1% instrumental error. A precise counting of the total charge deposited on the target is important for the measurement of cross sections.

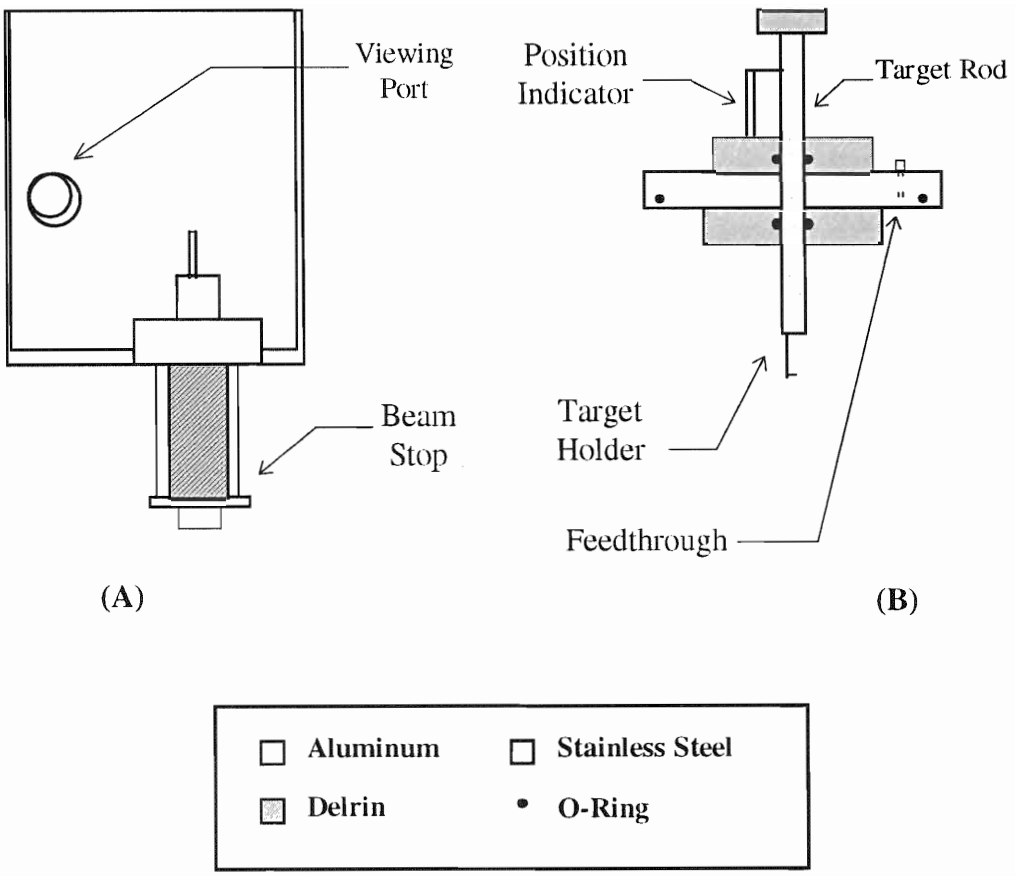

Figure 2.5 The schematics for main proton-deuteron capture scattering chamber. In the figure, Part A is sideview of the main chamber body, and part B is the solid target mounting assembly.

2.5 Deuterated and Hydrogenated Target Fabrications

Developing suitable targets is a critical step for almost any successful nuclear experiments. It is especially important for low energy nuclear capture reactions since one usually has to face the difficulty of a large amount of heat dissipated from beam bombardment. Such a condition requires the target to be extraordinarily durable to last

even a few weeks of ion bombardment. In the case of proton-deuteron capture reactions, several choices of targets have been attempted and tested. The overview of the techniques associated with each target development is very useful for providing new ideas for many experimental endeavors. The final choice for the target material for this project turned out to be the simplest and the easiest of all. Nevertheless, the experience itself is valuable and very rewarding. In this chapter, discussions will be focused on target processing design and testing methods. Hydrogen surface profiling technique using high energy proton-proton elastic scattering analysis is also introduced.

2.5.1 Compressed Chemical Compound Targets

The pursuit of high density hydrogenated and deuterated targets began with finding hydrogen or deuterium enriched materials. It is natural to think about hydrogen-rich materials in the forms of organic compounds. There is a wide variety of such compounds containing hydrogen and its isotopes. However, due to the single-valence bond of hydrogen atom, most of them are in gas or liquid form because the bonds are generally not strong enough to constrain or combine the compounds into solid form unless special site binding is structured.

After a large database search by Aldrich Chemical Company, only about 80 solid compounds was found containing hydrogen or deuterium [Ald92]. Only two categories of the compounds satisfy the basic requirements for this thesis project. Namely, the material must have a high percentage concentration of hydrogen and a high melting point to ensure the durability. One type is the multi-element compound materials such as $NaBH_4$ / $NaBD_4$

or NH_4Cl / ND_4Cl. The other type is the rare earth hydride or deuteride compounds such as ZrH_2 or TiH_2. All of these compounds are in the form of either fine powder or small pellet grain .

In order to make powder-like targets that can be put into a high-vacuum chamber, a brute force method was attempted. The powder compound was placed inside a small round die made from copper. Then they were smashed into a solid chunk by using a very high pressure. The idea behind this was developed from polarized target experiments [Hee85]. In these experiments, fine metal compound powder was compressed onto a heat sink in order to increase the cooling efficiency of the target. The temperature could reach as low as sub-Kelvin region.

A safety point should be mentioned that almost all of the hydrogen compounds tend to be explosive. When compressing the powder, time and speed have to be under careful control. In principle, the slower the powder is compressed, the easier the generated heat can be dissipated. One reason for using copper to make the die is also out of this concern since copper is a very good heat conductor. The die was made about 2 cm in diameter and 0.4 cm in thickness. The pressure was generated from a hydraulic compressor, which is capable of reaching a pressure of 5 T/cm^2. The normal pressure used for compressing hydrogen targets is around 1 T/cm^2 to 2 T/cm^2. Usually after the compression, the shape of the die was deformed dramatically. To limit such deformation, a thick stainless steel mold was placed around the die. All of the aforementioned compounds except ZrH_2 were experimented with. ZrH_2 was not used as it was not commercially available.

The $NaBH_4$ target was tested first for beam bombardment, but after only 5 minutes, the compound was burnt out and no trace of hydrogen was ever detected. The NH_4Cl target tested had shown a much better durability. During two hours of bombardment, the target still held together. The γ-rays of 5.5 MeV from the $^1H(p,\gamma)^3He$ reaction were detected by using two BaF_2 detectors . There had been found that a large amount high energy γ-rays were coming from beam induced reactions. Further investigation revealed that they were from $^{15}N(p,\gamma)^{16}O$ reaction. The γ-rays from this reaction carried a full energy of 7.29 MeV. Due to its much higher cross section, the Compton plateau and escape peaks from the reaction interfered greatly with the 5.5 MeV γ-rays from the proton-deuteron captures. These target choices were therefore abandoned for our investigations. The compressed NH_4Cl target should well serve the purpose for $^{15}N(p,\gamma)^{16}O$ measurements.

The TiH_2 / TiD_2 target was experimented with next by the compression technique. This black-grayish powder has a mass density of 3.75 g/cm^3. It is commercially available with a chemical purity of 99.9%. The hydrogen number density calculated from TiH_2 structure is almost as twice as that of pure hydrogen gas. The on-line testing for the TiH_2 powder compressed targets were carried out in the same way as described above. The resulting yields is much less than calculated value. The target density thickness estimated from the experiments was only in the range of 10^{16} atoms/cm^2.

Since low energy hydrogen ions were stopped quickly on the surface of the compressed target, the surface property became the deciding factor for the hydrogen thickness of the target. A calculation using the parameters of stopping powers for

deuterium ions by Anderson and Ziegler [And77] showed that the average range for hydrogen ion is around 1.2 microns in TiH_2 compound. Therefore, it was concluded that surface contamination for the compressed powder might be causing the much lower target density than expected. This contamination might come from compressing process or simply from the head of hydraulic compressor that had been used. After realizing this, effort was shifted to other target-making techniques in order to improve the surface properties of the target. Two techniques had been attempted for this purpose, one is the gas deposition method and the other one is ion and plasma implantation method.

2.5.2 Gas Deposition Techniques

The idea for making targets by gas deposition is quite similar to that of material burning process in the open air. Firstly, the solid material is heated up to certain temperature, then it "burns" with oxygen to form final oxidized material. In this investigation, thin Ti metal foil was used. It was burnt and mixed with hydrogen or deuterium gas. Since hydrogen or deuterium could only penetrate a thin layer (less than 1 micron) of Ti foil, hydride or deuteride compound was formed on the surface of pure Ti metal foil.

Titanium was chosen over other metals for loading hydrogen or deuterium mainly because of its large loading capacities. Titanium hydride system had been proposed about thirty years ago for storing hydrogen, which was considerd as a fuel substitue for auto gasoline [Dus62]. It was noticed that both Titanium hydride and Titanium deuteride could be formed easily when gas deposition method was used [Sie31].

The experimental arrangement for making such a target is shown in Figure 2.6. The same setup can also be used for evaporating salt or other compound materials. During the fabrication process, the heated vapor can easily solidify itself on a cold surface of a slide placed inside the evaporating chamber. The thickness of the condensed layer could be as thin as several Angstroms. This method is commonly used for making thin film slides. Before gas deposition or vapor condensation, the chamber was pumped out through a standard two-stage diffusion pump. A current transformer was connected to two copper electrodes on the bottom of the evaporator chamber. It is capable of conducting DC current up to 50 A.

Titanium foils of 0.6-3.0 microns was used. The top of the chamber is vacuum-sealed by a thick metal-glass dome. This enables the operator to observe the evaporation process. A Freon compressor drives the coolant through a copper tubing placed inside of the cold finger to which prong electrodes were attached. A small dewar is placed in contact with a cold baffle. The dewar was filled with liquid nitrogen to provide additional cooling.

The foil is placed between two electrodes before the chamber was evacuated. When current of about 10 A ran through the foil, it was heated up to a glowing red color. The released power could be calculated from measured foil resistance and the current. The temperature of the glowing foil was estimated at 400 ^{o}C.

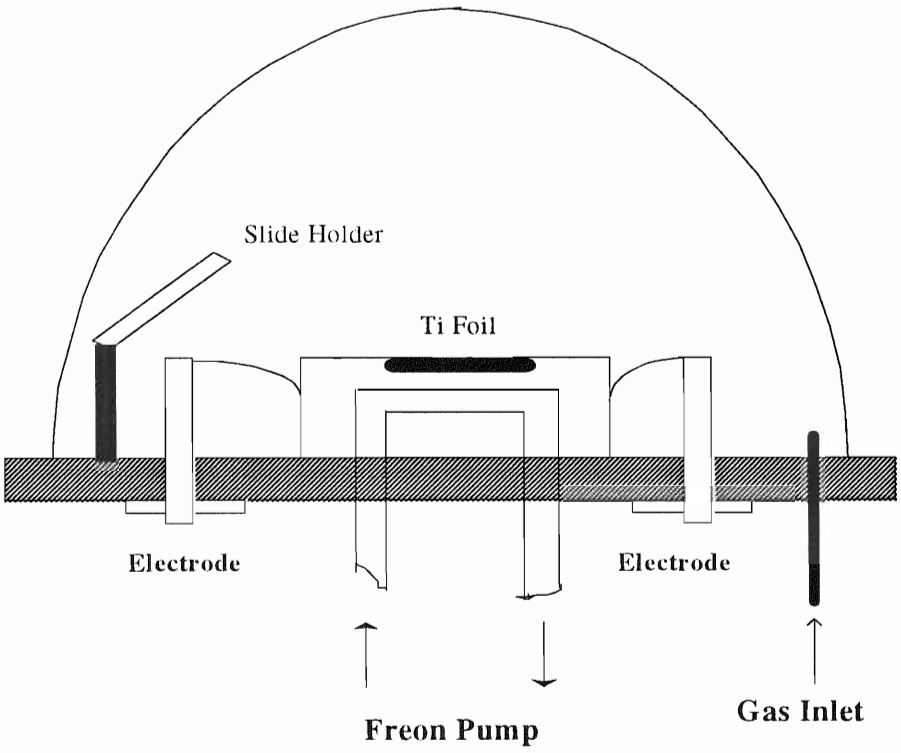

Figure 2.6 The evaporator setup for depositing Titanium deuteride or hydride targets. The egg-shaped transparent dome in the figure is vacuum sealed and isolated from the aluminum bottom plate.

At this point, chemically pure hydrogen or deuterium gas was slowly bled into the evaporating chamber. The foil instantly changed shape when this occurred. Wrinkles wasobserved to form on its surface during the absorption process. The reason for this is that the mass density of the Titanium deuteride or Titanium hydride is less than that of pure Titanium metal. The foil had to expand its volume to accommodate the forming of the compound.

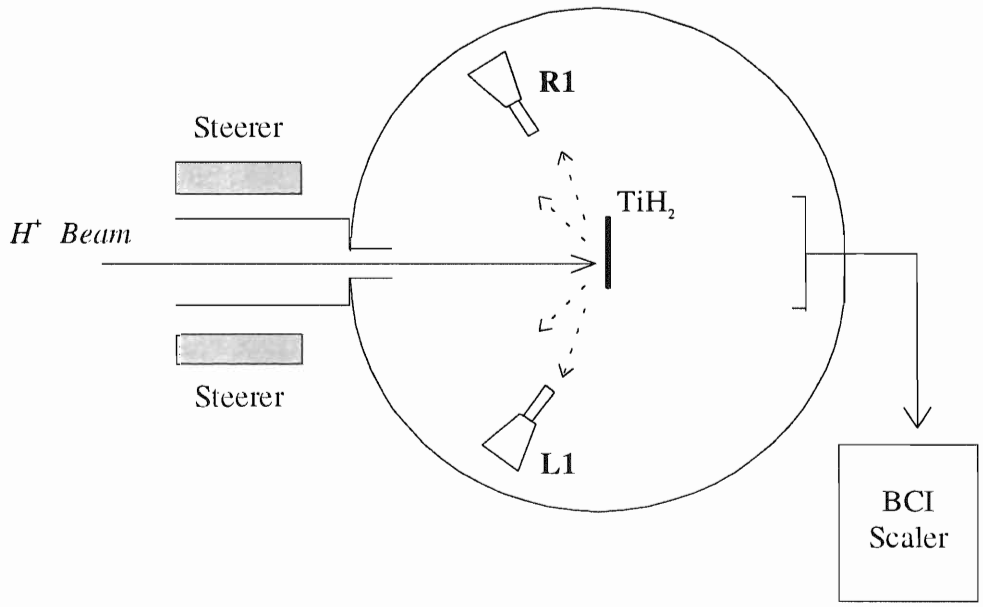

Figure 2.7 Scattering chamber set-up for target thickness measurements.

The deposited target was tested by high energy proton elastic scattering method. This is one of the nondestructive methods for hydrogen tracing analysis [Coh72]. The set-up is shown in Figure 2.7. Proton beam of 16.6 MeV energy was used to bombard a TiH_2 target. Two detectors were placed symmetrically at 135° in the lab frame.

The total energy of the two protons scattered from the target are precisely measured in coincidence in the left (L1) and the right (R1) detectors. Since the energy loss of the proton in the target is given by

$$\Delta E \equiv E_b - (E_L + E_R) = (\frac{dE}{dx})_{E_b} * x / \cos(45^\circ) \qquad (2.3)$$

where E_b is the beam energy, $(E_L + E_R)$ is the total energy of the scattered protons from left and right detectors, dE/dx is the stopping power of the Ti foil, and x is the depth where an incoming proton can penetrate inside the target.

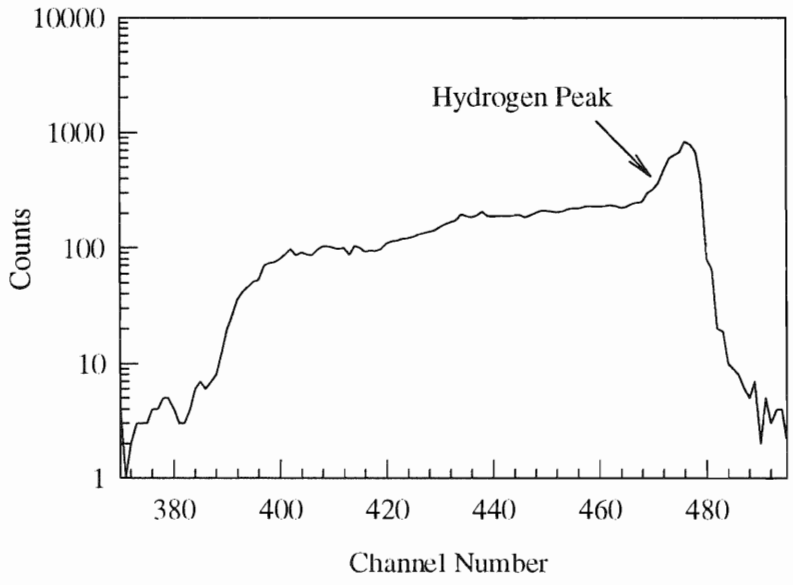

Figure 2.8 Profiling spectrum for a TiH_2 target with 3 μm foil thickness.

As we can see from Equation 2.3, (E_L+E_R) is a linear function of x therefore represents the contents profile of the target. A typical TiH_2 target profile spectra is shown in Figure 2.7.

The observed flat level in Figure 2.8 was mostly coming from Titanium itself. The typical deuterium or hydrogen concentration measured from this type of targets were around 10^{16} atoms/cm^2.

A batch of gas deposited deuterium targets was also tested for deuterium contents by taking spectra from low energy $^{2}H(p,\gamma)^{3}He$ reaction using one large BaF_2 scintillator (see Figure 2.8).

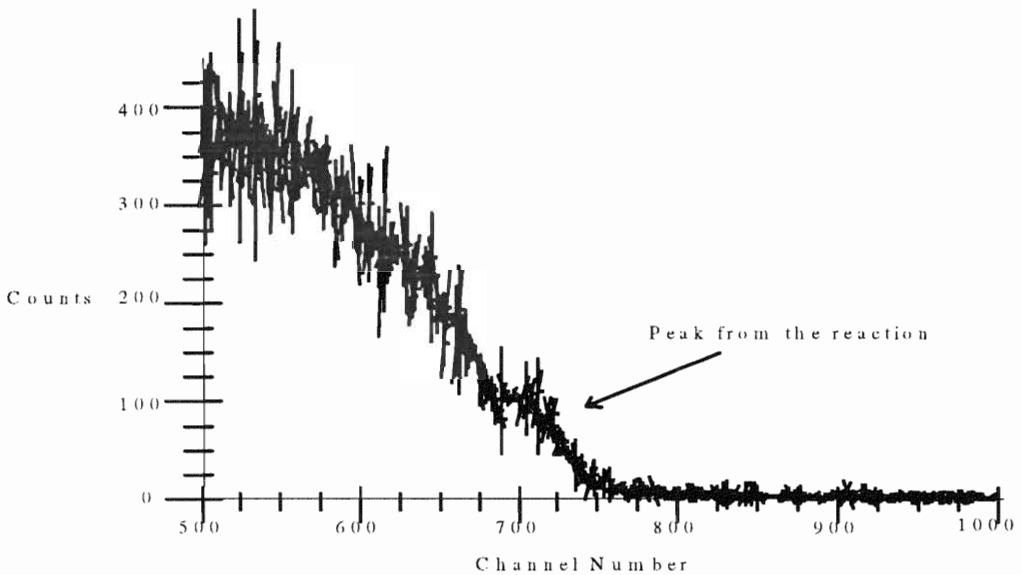

Figure 2.9 On-line Spectrum of $^{2}H(p,\gamma)^{3}He$ reaction measured from BaF_2 scintillator.

The raw γ-ray spectrum is shown in Figure 2.9 and the background substracted peak along with a Gaussian fit is shown in Figure 2.10. The target thickness calculated from this reaction was in agreement with the results obtained from proton elastic scattering.

However, the gas deposited targets proved to be unstable under beam bombardment. After several hours of irradiation by 2 μA proton beam, the yield from the reaction was found to decrease continuously. It is believed that the target surface is outgassing and losing its deuterium contents. The changing of target thickness might not

present a problem in analyzing powers measurement if the targets are often replaced, but it makes the precise measurement of cross sections very difficult.

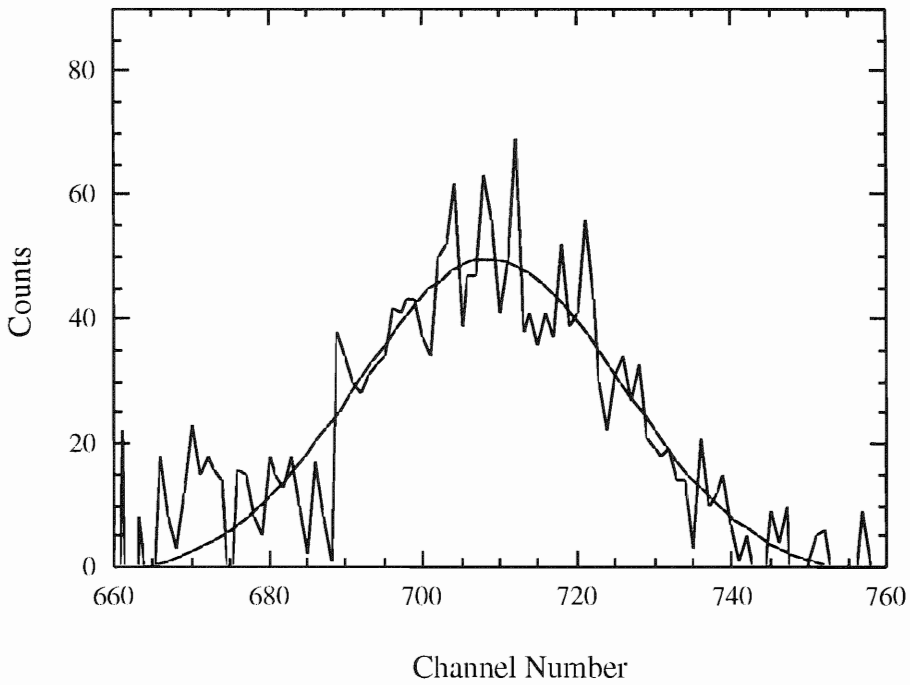

Figure 2.10 The background subtracted peak spectrum from Figure 2.8. The solid line is the Gaussian fit.

2.5.3 Ion and Plasma Implantation Techniques

As it has been noticed, all techniques mentioned above are used for providing targets whose thickness are hard to monitor during the fabrication process. Separate experiments have to be conducted to determine the thickness of the produced targets.

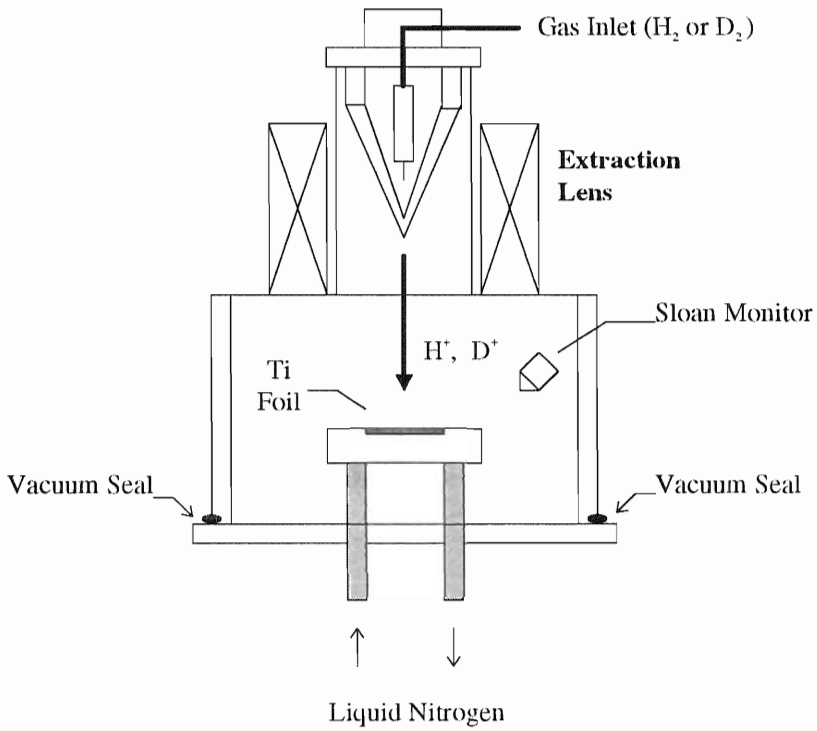

Figure 2.11 Set-up for ion implantation of thin Ti hydride or deuteride targets.

The situation is different for ion implantation technique. Here one can easily monitor the total hydrogen or deuterium ions implanted onto the substrate foil. The sputtered material during the process can be monitored by a Sloan detector placed inside the implantation chamber (see Figure 2.11). Pure 1.5-5.0 μm thick Titanium foils were used for ion implantation. When hydrogen or deuterium ions are implanted into Titanium, vacancies were produced in the foil and hydrides or deuterides are eventually formed through the exothermal chemical reactions [Tak88].

The ion implantor consists of a duoplasmatron source, a high-voltage extraction lens and a sputtering chamber. A magnetic field generated by a DC coil is used for

focusing the extracted ions. The implantor is capable of implanting ions with a maximum energy of 20 keV (see Figure 2.11).

There are two processes accompanying each other during the ion implantation. Ions are trapped into the foil substrate, while at the same time they sputter away its surface materials. The initial implanted depth is determined by the momentum of incoming ions. Eventually, sputtering process would recess the initial implanted layer and proceed to implant into a deeper layer. These two processes are competing with each other and quickly bringing the concentration of implanted ions to an equilibrium . The final dosage can be calculated from a phenomenological model which incorporates these two effects. A FORTRAN code was written for computing the average accumulated implanted hydrogen or deuterium dose inside the target and it was used for the calculation of the final target thickness [Moo88].

The resulting target thickness was typically at 10^{16}-10^{17}atoms/cm^2. On-line experiments had shown that there had been a considerable improvement of target outgassing problems in comparison with gas deposited target. However, decrease in target thickness was still observed after about ten hours of beam bombardment. It was concluded that this is mainly due to the target loss caused by the beam sputtering process. During the measurement, it was also noticed that the target had become very brittle after a long time of bombardment.

In order to reduce the effects of too much sputtering from Titanium foil surface, a plasma deposition method, which is similar to ion implantation, was also tried (see figure 2.12). In this method, a glass tube was first filled with a gas mixture of 96% argon and

4% hydrogen. A 3 μm thick 0.5" by 0.5" Titanium foil was placed inside the glass tube. It was placed inside an LC coil which was connected through a high power microwave generator to strike a plasma inside the glass tube. After six hours of plasma shower, the Titanium foil was extracted. The hydrogen density in the targets was measured to be around 10^{15} H/cm^2 from this method. It was considerably lower than ones that produced by ion implantation method. It was instantly suspected that hydrogen concentration in the gas mixture was too low. However, when hydrogen content in the tube was raised to 6%, the plasma became too weak to sustain itself. The initial striking of the discharge had become very difficult to achieve.

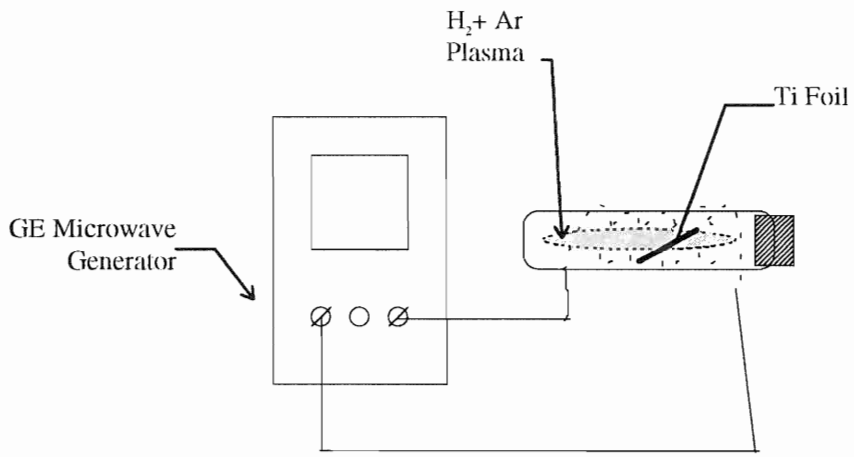

Figure 2.12 Set-up for making hydrogenated targets by plasma deposition technique.

The pursuit of thin transmission target was completely overhauled after we had acquired two high resolution Germanium detectors. With their high energy resolutions, energy dependence of the beam stopping effects in a thick target can be easily extracted. The goal of making thin target so that reaction energy could be precisely localized had

become unjustifiable. Therefore vapor condensed thick ice and heavy ice targets were chosen for the present experiment instead.

2.5.4 Solid Ice and Heavy Ice Targets

The method for making heavy ice and ice targets was implemented following that of Griffiths [Gri63]. The schematic drawing of the apparatus is shown in Figure 2.12.

The dewar holding liquid nitrogen is made from stainless steel. A copper cold finger 25 cm long was attached to the inside of the dewar. A round copper disc was machined to counter set into the copper finger. The disc was 4 cm in diameter and 0.5 cm in thickness. It served as the substrate onto which ice or heavy ice could be formed. A thin vapor conducting tubing was silver soldered onto the side of the dewar. On one end of the tubing that was twisty bent inside the chamber, a nozzle sprayer was attached. The funnel-shaped sprayer was stuffed with glass wool to prevent water drops from being directly sucked into the chamber. The outside of the tubing was inserted into a high-vacuum flask through a No. 2 standard plug. The flask was first cleansed by alcohol, heated dry, then rinsed with pure water or heavy water before its use.

Procedures were tested and developed to make pure ice or heavy ice target without contaminating its surface. Firstly, the chamber was rough out to a vacuum of 10^{-2} torr with the valve to the water flask closed. Then the valve was cracked open to pump out the section leading to the flask. When pressure in the flask became gradually lower than the vapor pressure, water started boiling. Then the tube gate valve to the turbo molecular pump was opened. The chamber pressure improved dramatically afterwards.

When pressure was below 10^{-5} torr, dewar was filled with liquid nitrogen. As water vapor solidified on the cold disc, vacuum slowly improved to below 10^{-6} torr. The final thickness of the ice could reach approximately 0.5 cm.

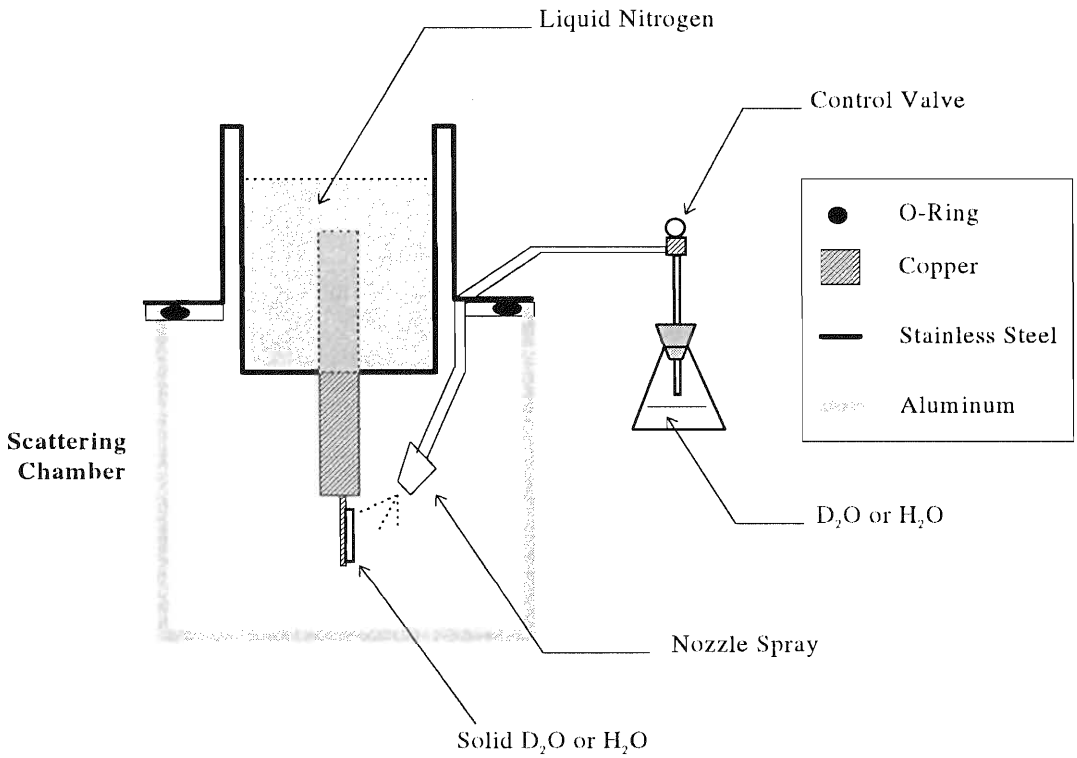

Figure 2.13 Schematic drawing of the apparatus for making vapor condensed targets.

When the beam was sent onto the target for the first time, evaporation from the ice could happen due to large heat deposition. This was indicated by the worsening vacuum of the chamber. As the heat was conducted away, target reached a state of thermal equilibrium and pressure reading became stabilized. The condensed target could

last for more than one week of in-beam bombardment. The target thickness calculated by using the stopping powers of solid H_2O and D_2O reached the order of 10^{19} atoms/cm^2. This is more than one order of magnitude higher than any of previously made thin targets.

2.6 Detectors

Throughout this project, two different kinds of detectors were tested and used: BaF_2 scintillators and Germanium detectors. BaF_2 Scintillator was used in the early stage of the project to test targets and to conduct sensitivity studies of neutron background from deuteron captured on proton. High purity Germanium (HPGe) detectors were used for final data collecting.

BaF_2 scintillator has been popular for studying light charged particle reactions [Lan92] and hard photons [Nov87] in recent years. The crystal itself is easy to grow and easy to shape mechanically. It possesses a pico-second response time and a energy resolution that is comparable to that of NaI Scintillator [Kar86]. A summary of its properties in comparison with that of the popular NaI scintillator is listed in Table 2.3. Due to its high Z and large density, BaF_2 is generally more efficient than most of the other scintillating materials.

It has been noticed that there are four distinct lines in the background spectrum of BaF_2. They have the energies of 1.46 MeV, 1.78 MeV, 1.98 MeV and 2.86 MeV respectively [Wis84]. All of them are from the intrinsic decay chain of radioactive contaminants in the crystal itself. These four lines had be used as part of the energy calibration of the spectra. They served as the reference for monitoring and stabilizing

gains of the detector amplifiers. However other radioactivity such as the β-decays of ^{212}Bi and ^{208}Tl from the crystal also increased the detecting background in the energy region of interest. The block diagram of the electronics for using two BaF_2 detectors are shown in Figure 2.13. Constant Fraction Discriminators (CFD) in the set-up are used to generate the fast gates that are required by the ADC interface.

	BaF_2	NaI
Density (g/cm^3)	4.88	3.67
Hardness (Mho)	3	2
Refraction Index	1.49	1.85
Boiling Point (^oC)	1357	751
Fast Timing constant	600 ps	320 ns
Emission Wavelength (nm)	220	415
Energy Resolution (^{137}Cs)	~12%	~10%
Hygroscopic	No	Yes

Table 2.3 Physical properties of BaF_2 and NaI scintillators.

The two HPGe detectors used in the present work are manufactured by EG&G ORTEC company. One has a straight PopTop design and the other one has an off-centered dewar [Ort95]. Both detectors are made from P-type materials. The relative efficiencies for two detectors are 125% and 145% respectively, which are measured with

respect to a standard Φ3×3 cm NaI scintillator. The energy resolutions for both detectors are under 2 keV for 1.33 MeV ^{60}Co full energy peak.

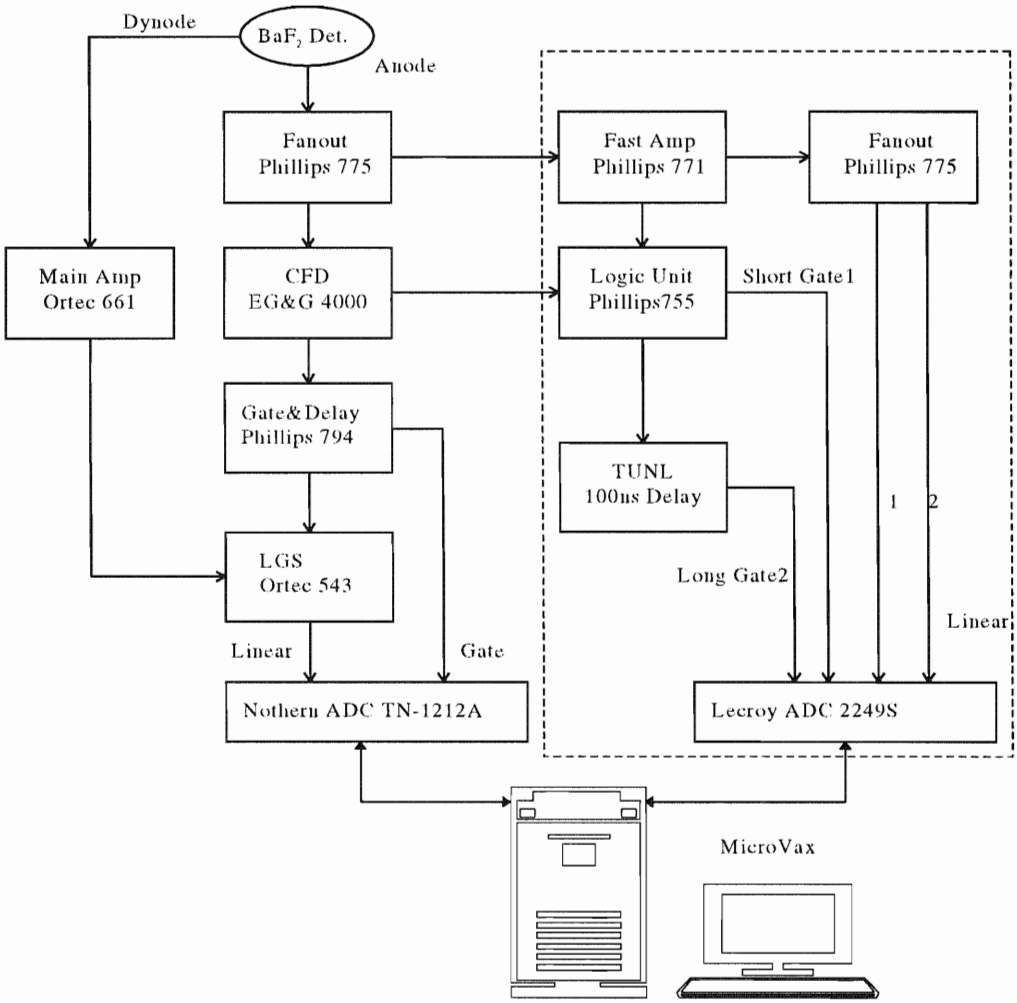

Figure 2.13 Block diagram for electronics setup of BaF_2 scintillator, The dashed box represents the set-up for the pulse shape discrimination used in the target testing runs.

It is known that Germanium detectors are extremely sensitive to the neutron damage. Both detectors have been recommended against operating under a neutron flux

of 10^8 per second per cm^2 [Ort95]. During the on-line experiment, neutron flux could be present from $^2H(d,n)^3He$ reaction in the target material. Therefore, BaF_2 scintillators were also used to monitor neutron background. No noticeable radiation damage effects had been observed during the course of this work. Finally, the electronics setup for HPGe detector is given in Figure 2.14.

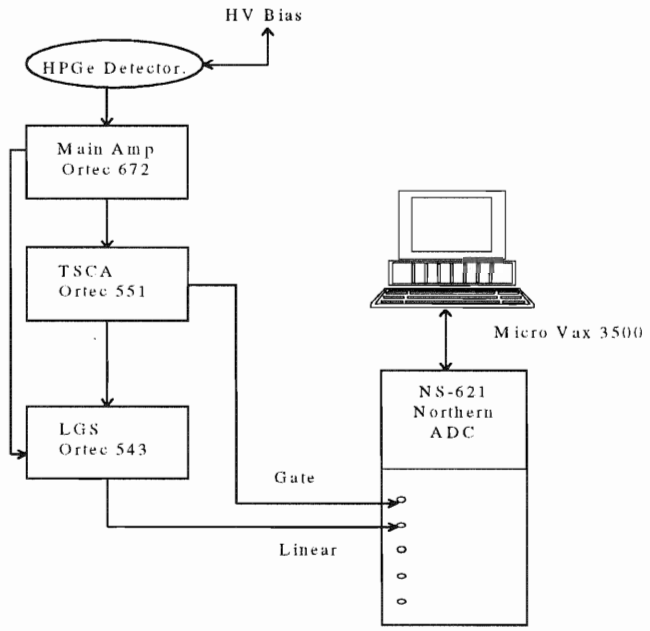

Figure 2.14 Electronics set-up for HPGe detector.

III. Experimental Techniques and Methods

3.1 Overview

The formalism for the measurement of cross section is straightforward, while the experimental implementation is tedious and full of pitfalls. On the other hand, the formalism for analyzing powers measurements could be quite complicated, yet it is easier to accomplish experimentally. In this chapter, the discussion will be focused on experimental formalisms rather than their implementations.

First of all, the concepts and techniques for measurements of differential cross section and spin-1 (deuteron) and spin-1/2 (proton) analyzing powers are introduced. Since the monitoring of the beam polarization is vital to determination of polarization observables in nuclear reactions, both low energy and high energy polarimeters for vector and tensor measurements are discussed. The results for the measured vector and tensor polarizations are presented. The upgraded TUNL data acquisition system and electronics setup for polarization measurements are discussed exclusively in this chapter.

3.2 Cross Section Determination

The definition of experimental cross section at a given beam energy can be written as

$$\sigma(\theta,\phi) \equiv \frac{d\sigma}{d\Omega}(E_{cm}) = \frac{dN}{F\,nt\,D\varepsilon\;d\Omega} \qquad (3.1)$$

where dN is the number of the events detected by a detector with a solid angle $d\Omega = sin\theta\, d\theta\, d\phi$, F is total number of beam particles, n is the target density, t is the target thickness, D is the electronic dead-time correction for detectors, and ε is the detector efficiency.

Total cross section is theoretically defined as the differential cross section integrated over entire 4π solid angles. It should be noted that in Equation 3.1, variables such as dN, t, and ε are both energy and space dependent. An integration over $d\Omega$ on the right-hand side of the equation will not just produce a 4π multiplier. The technique for resolving angular dependence of the cross section is by the method of complete Legendre polynomial expansion. This technique will be discussed in Chapter 4.

Extraction of energy dependence of the total cross section is the focal point in the field of nuclear astrophysics. As we have discussed in the first chapter, it is convenient to define astrophysical S-factor S(E) in order to extrapolate the total cross section to the energy region that is equivalent to the stellar temperature (see Equation 1.2). Both S-factor and the definition of differential cross section in Equation 3.1 is for the spin averaged unpolarized cross section.

3.3 Analyzing Powers Formalism

If incoming beam is spin polarized, the cross section can be expressed as the unpolarized cross section multiplied by a function that is spin dependent. This results from the fact that the wave functions describing all nuclear systems are spin and isospin separable.

For a *purely* vector polarized beam, the cross section definition in Equation 3.1 can be expressed as

$$\sigma(\theta,\phi) = \sigma_u(\theta,\phi)\{1 + \frac{3I_b}{I_b + 1}\mathbf{P}\cdot\mathbf{A}\}, \qquad (3.2)$$

where I_b is the spin of the projectile, **P** is polarization vector of the beam, **A** is vector analyzing power and σ_u is the unpolarized cross section. It can be easily seen that for spin-1/2 polarized proton beam, Equation 3.2 is reduced to

$$\sigma(\theta,\phi) = \sigma_u(\theta,\phi)\{1 + \mathbf{P}\cdot\mathbf{A}\} \qquad (3.3)$$

and for spin-1 "purely" vector polarized deuteron beam, it becomes

$$\sigma(\theta,\phi) = \sigma_u(\theta,\phi)\{1 + \frac{3}{2}\mathbf{P}\cdot\mathbf{A}\} \qquad (3.4)$$

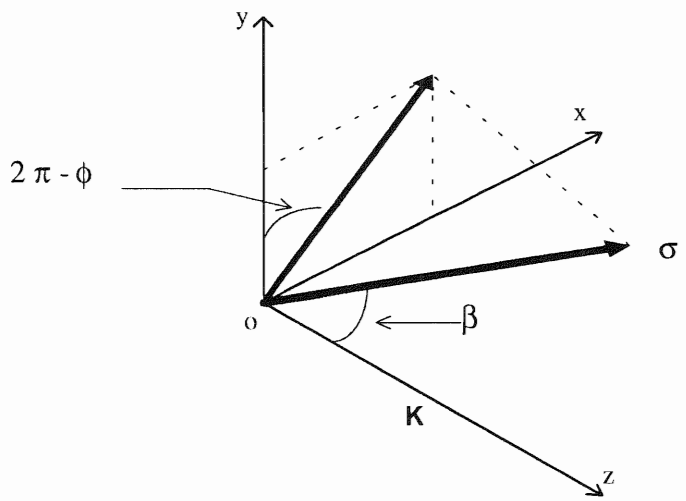

Figure 3.1 The Madison convention for spin orientations.

To specify the direction of the spin vector in Equation 3.1, coordinates frame is generally chosen to follow the agreement that set forth by the Madison Convention [Hae70]. This system of coordinates is illustrated in Figure 3.1.

The z-axis is chosen to be beam's momentum direction $\mathbf{K}_{in}$ and y-axis is determined by $\mathbf{K}_{in} \times \mathbf{K}_{out}$ i.e. cross product of incoming momentum $\mathbf{K}_{in}$ of the projectile and the detected particle's momentum $\mathbf{K}_{out}$. The x-axis can then be fixed by the cross product between the unit vectors of y and z-axis's following the definition of right-hand Cartesian coordinates .

Two independent angles (β and ϕ) are used to determine the inner direction of spin vector. β is defined as the angle between the spin vector and z-axis, and ϕ is the angle from y-axis to the projection of the spin vector in the x-y plane (see Figure 3.1). The conventional rule for the "left" and "right" is always defined by following the direction of the incoming particle i.e. $\mathbf{K}_{in}$ direction rather than $-\mathbf{K}_{in}$ direction.

Usually the direction of **P** is pre-fixed along z-axis by the magnetic field in the ion source during the experiment. This would reduce the inner product of **P** and **A** to its algebra product of $P_z A_z$. Therefore,

$$\begin{cases} \sigma^{(+)}(\theta, \phi) = \sigma_u(\theta, \phi)(1 + P^{(+)}_z A_z) \\ \sigma^{(-)}(\theta, \phi) = \sigma_u(\theta, \phi)(1 + P^{(-)}_z A_z) \end{cases} \tag{3.5}$$

where $\sigma_u(\theta, \phi)$ is the unpolarized cross section, $P^{(+)}_z$ and $P^{(-)}_z$ correspond to the two different spin states generated by switching on MF2 and SF2 transition units separately. Solving the two equations in Equation 3.5, A_z is given by

$$A_z = \frac{\eta - 1}{P_z^{(+)} - \eta P_z^{(-)}} \tag{3.6}$$

where η is the ratio $\sigma^{(+)}/\sigma^{(-)}$.

Since A_z depends only on the ratio of two-spin-state cross sections, all the efficiencies, geometric factors, and target thickness effects are canceled between the

nominator $\sigma^{(+)}$ and the denominator $\sigma^{(-)}$ in Equation 3.6. Therefore, η can be simply substituted with $Y^{(+)}/Y^{(-)}$, which is the ratio of the two-spin-state yields from the *same* detector.

In the ideal case of two-spin-state flipping, $P_z^{(+)}$ is equal to $-P_z^{(-)}$. Then Equation 3.6 can be reduced to the standard formula for calculating vector analyzing power of spin-1/2 system

$$A_z = \frac{1}{P_z}\frac{\eta - 1}{\eta + 1} \quad , \tag{3.7}$$

where the vector analyzing power A_z is calculated from the asymmetry factor $\frac{\eta - 1}{\eta + 1}$ divided by the beam polarization.

On other hand, the formulae become a little more complicated for the polarized deuteron induced reactions,. Since deuteron carries spin-1, which is a rank-2 tensor. The cross section in this case can be expressed as

$$\frac{d\sigma}{d\Omega} = \frac{d\sigma}{d\Omega_u}\left\{\sum_{kq} t_{kq} T_{kq}^{*}\right\} \tag{3.8}$$

where $d\sigma/d\Omega_u$ is the unpolarized cross section, t_{kq} describes the polarization state of the incident deuteron, T_{kq} is the tensor polarization for the reaction.

Expanding Equation 3.8 in Madison Coordinates, the cross section for incident spin-1 deuteron is given by

$$\frac{d\sigma}{d\Omega} = (\frac{d\sigma}{d\Omega})_{unpol}\{1 + \frac{3}{2}P_z A_y(\theta)\sin(\beta)\cos(\phi) + \frac{1}{4}P_{zz}A_{zz}(\theta)(3\cos^2(\beta) - 1)$$
$$+ \frac{1}{4}P_{zz}A_{zz}(\theta)(3\cos^2(\beta) - 1) + P_{zz}A_{xz}(\theta)\sin(\beta)\cos(\beta)\sin(\phi) \qquad (3.9)$$
$$+ \frac{1}{4}P_{zz}(A_{xx}(\theta) - A_{yy}(\theta))\sin^2(\beta)\cos(2\phi)\}$$

It should be noted that both spin and analyzing power matrices are trace free, e.g., in the case of analyzing powers

$$A_{xx} + A_{yy} + A_{zz} = 0 \qquad (3.10)$$

When measuring A_{zz}, β is set to be 0^o and for A_{yy} measurement, β is rotated to 90^o instead. By the substitutions of β values and using the traceless condition of Equation 3.10, Equation 3.9 can be reduced to

$$\frac{d\sigma}{d\Omega} = (\frac{d\sigma}{d\Omega})_{unpol}\{1 + \frac{1}{2}A_{zz}(\theta)P_{zz}\} \qquad (\text{if } \beta=0^o) \qquad (3.11)$$

$$\frac{d\sigma}{d\Omega} = (\frac{d\sigma}{d\Omega})_{unpol}\{1 + \frac{3}{2}P_z A_y(\theta)\cos\phi + \frac{1}{2}A_{yy}(\theta)P_{zz}\} \qquad (\text{if } \beta=90^o) \qquad (3.12)$$

Based upon Equation 3.11, the measurement of A_{zz} could be carried out by using only two spin states which have different values of P_{zz}, namely $P_{zz}^{(2)}$ from spin-state-2 and $P_{zz}^{(3)}$ from spin-state-3. It is by our convention that spin-state-1 is used to denote the unpolarized state. It is evident from Equation 3.11 that A_{zz} can also be measured by just using either one of the spin-state together with another unpolarized state. However, the two-spin-state data taking scheme is favored by error analysis, which will be discussed in the later chapter.

More explicitly, by substituting $P_{zz}^{(2)}$ and $P_{zz}^{(3)}$ into Equation 3.11 we have

$$\begin{cases} \dfrac{\sigma^{(2)}}{\sigma^{(1)}} = 1 + \dfrac{1}{2} P_{zz}{}^{(2)} A_{zz}(\theta) \\ \\ \dfrac{\sigma^{(3)}}{\sigma^{(1)}} = 1 + \dfrac{1}{2} P_{zz}{}^{(3)} A_{zz}(\theta) \end{cases} \tag{3.13}$$

Solving these equations for A_{zz}, we obtain

$$A_{zz} = \frac{2(1-\eta)}{\eta P_{zz}{}^{(2)} - P_{zz}{}^{(3)}}. \tag{3.14}$$

where

$$\eta \equiv \frac{\sigma^{(3)}}{\sigma^{(2)}} = \frac{Y^{(3)}}{Y^{(2)}}. \tag{3.15}$$

and $Y^{(2)}$ and $Y^{(3)}$ denote the detector yields for spin state-2 and spin state-3 respectively.

The A_{yy} measurement can be approached by many methods. It is important that any measurement scheme should minimize various sources of errors such as spin misalignment, etc. A detailed discussion of different aspects of using tensor polarized deuteron in analyzing power measurements can be found in the Ph.D. thesis of Tonsfeldt [Ton81]. Since vector polarizations are also present in our two-state tensor polarized beam as discussed in Chapter 2 (i.e., for state-2, P_z = -1/3 and for state-3, P_z = +1/3), it is possible to measure vector analyzing powers and tensor analyzing powers simultaneously. In this case, two symmetrically placed detectors together with two-spin states coulc be used. From Equation 3.12, it can be seen that for a left-side placed detector whose ϕ=0°,

$$\begin{cases} \dfrac{\sigma_L{}^{(2)}}{\sigma_L{}^{(1)}} = 1 + \dfrac{3}{2} P_z{}^{(2)} A_y(\theta) + \dfrac{1}{2} P_{zz}{}^{(2)} A_{yy}(\theta) \\ \\ \dfrac{\sigma_L{}^{(3)}}{\sigma_L{}^{(1)}} = 1 + \dfrac{3}{2} P_z{}^{(3)} A_y(\theta) + \dfrac{1}{2} P_{zz}{}^{(3)} A_{yy}(\theta) \end{cases} \tag{3.16}$$

while for the right-side detector whose $\phi = 180^{o}$, Equation 3.12 becomes,

$$\begin{cases} \dfrac{\sigma_R^{(2)}}{\sigma_R^{(1)}} = 1 - \dfrac{3}{2} P_z^{(2)} A_y(\theta) + \dfrac{1}{2} P_{zz}^{(2)} A_{yy}(\theta) \\ \\ \dfrac{\sigma_R^{(3)}}{\sigma_R^{(1)}} = 1 - \dfrac{3}{2} P_z^{(3)} A_y(\theta) + \dfrac{1}{2} P_{zz}^{(3)} A_{yy}(\theta) \end{cases} \tag{3.17}$$

Either Equation 3.16 or 3.17 can be solved directly for both A_y and A_{yy}. If Equation 3.16 is put into matrix form, it becomes

$$\begin{bmatrix} \dfrac{3}{2} P_z^{(2)} & \dfrac{1}{2} P_{zz}^{(2)} \\ \\ \dfrac{3}{2} P_z^{(3)} & \dfrac{1}{2} P_{zz}^{(3)} \end{bmatrix} \begin{bmatrix} A_y \\ \\ A_{yy} \end{bmatrix} = \begin{bmatrix} 1^{(2)} - 1 \\ \\ 1^{(3)} - 1 \end{bmatrix} \tag{3.18}$$

where $l^{(2)} \equiv \dfrac{\sigma_L^{(2)}}{\sigma_L^{(1)}}$ and $l^{(3)} \equiv \dfrac{\sigma_L^{(3)}}{\sigma_L^{(1)}}$. The direct solution for Equation 3.18 is straightforward and it is given as

$$\begin{bmatrix} A_y \\ \\ A_{yy} \end{bmatrix} = \begin{bmatrix} \dfrac{2P_{zz}^{[2]}}{3(P_z^{[3]}P_{zz}^{[2]} - P_z^{[2]}P_{zz}^{[3]})} \left(l^{(3)} - 1 - \dfrac{P_{zz}^{[3]}}{P_{zz}^{[2]}} l^{(2)} + \dfrac{P_{zz}^{[3]}}{P_{zz}^{[2]}}\right) \\ \\ \dfrac{2P_{zz}^{[3]}}{3(P_z^{[3]}P_{zz}^{[2]} - P_z^{[2]}P_{zz}^{[3]})} \left(l^{(2)} - 1 - \dfrac{P_{zz}^{[2]}}{P_{zz}^{[3]}} l^{(3)} + \dfrac{P_{zz}^{[2]}}{P_{zz}^{[3]}}\right) \end{bmatrix} \tag{3.19}$$

A similar expression can be obtained for Equation 3.17, which simply substitute all the P_z's to negative P_z's in Equation 3.19.

This method is suitable if only one detector is used in the measurement. To implement this scheme, run time has to be divided into three parts to count one

unpolarized state and two polarized states. Howeve, if two detectors are used instead, it is possible to just count the two polarized states. This is illustrated as the following.

From Equation 3.16 and 3.17, we can derive that

$$\begin{cases} l = \dfrac{1+\dfrac{3}{2}P_z^{(2)}A_y(\theta)+\dfrac{1}{2}P_{zz}^{(2)}A_{yy}(\theta)}{1+\dfrac{3}{2}P_z^{(3)}A_y(\theta)+\dfrac{1}{2}P_{zz}^{(3)}A_{yy}(\theta)} \\ r = \dfrac{1-\dfrac{3}{2}P_z^{(2)}A_y(\theta)+\dfrac{1}{2}P_{zz}^{(2)}A_{yy}(\theta)}{1-\dfrac{3}{2}P_z^{(3)}A_y(\theta)+\dfrac{1}{2}P_{zz}^{(3)}A_{yy}(\theta)} \end{cases}, \tag{3.20}$$

where

$$r \equiv \frac{\sigma_R^{(2)}}{\sigma_R^{(3)}} = \frac{Y_R^{(2)}}{Y_R^{(3)}} \quad and \quad l \equiv \frac{\sigma_L^{(2)}}{\sigma_L^{(3)}} = \frac{Y_L^{(2)}}{Y_L^{(3)}} . \tag{3.21}$$

Equation 3.20 can be written into a standard form of 2×2 linear equation:

$$\begin{bmatrix} -\dfrac{3}{2}(rP_z^{(3)} - P_z^{(2)}) & \dfrac{1}{2}(rP_{zz}^{(3)} - P_{zz}^{(2)}) \\ \dfrac{3}{2}(lP_z^{(3)} - P_z^{(2)}) & \dfrac{1}{2}(lP_{zz}^{(3)} - P_{zz}^{(2)}) \end{bmatrix} \begin{bmatrix} A_y \\ A_{yy} \end{bmatrix} = \begin{bmatrix} 1-r \\ 1-l \end{bmatrix} \tag{3.22}$$

Therefore, its solution is

$$\begin{bmatrix} A_y \\ A_{yy} \end{bmatrix} = \mathbf{P}^{-1} \begin{bmatrix} 1-r \\ 1-l \end{bmatrix}, \tag{3.23}$$

where **P** is defined as the 2×2 matrix on the left-side of Equation 3.22. The matrix form of the solution can be later used for simplifying error propagation calculations.

Another method for determining A_{yy} and A_y has also been used throughout this project. The formalism is used by taking advantage of symmetric pair setup of the detectors. From Equation 3.16 and Equation 3.17, it can be derived that

$$\begin{cases} A_{yy}(\theta) = \dfrac{1}{P_{zz}^{(i)}}\left(\dfrac{\sigma_R^{(i)}}{\sigma_R^{(1)}} + \dfrac{\sigma_L^{(i)}}{\sigma_L^{(1)}} - 2\right) \\ \qquad\qquad\qquad\qquad i = 2,3 \\ A_y(\theta) = \dfrac{1}{3P_z^{(i)}}\left(\dfrac{\sigma_R^{(i)}}{\sigma_R^{(1)}} - \dfrac{\sigma_L^{(i)}}{\sigma_L^{(1)}}\right) \end{cases} \tag{3.24}$$

This method has been used when only one polarized spin state is available for the measurement. It can be seen that Equation 3.24 is totally symmetric in the sense that we can swap A_{yy} between P_{zz} and A_y between P_z. Therefore, this method has also been frequently used for monitoring beam polarization. Usually A_y and A_{yy} are known for the monitoring reaction and beam polarizations P_z and P_{zz} can be handily calculated for each spin state by using Equation 3.24.

3.4 Data Acquisition System

Data acquisition system is the heart for realizing schemes for polarization and analyzing power measurements as described above. It is fully responsible for the polarization state switching and time sharing and dividing throughout this project.

The electronic data acquisition system for the present measurements consists of three major sections, namely, spin-state switching section, polarization monitoring system, and γ-ray detection system (i.e. Germanium or BaF_2). Digitized data processed through these three sections are controlled by a TUNL Multiple Branch Driver (MBD). A DEC microVAX 3500 work station which supervises the data acquisition processes is

connected to this driver through standard CAMAC databus. The on-line software system is run under the environment of XSYS analysis package [Gou81].

3.4 Spin-states Switching System

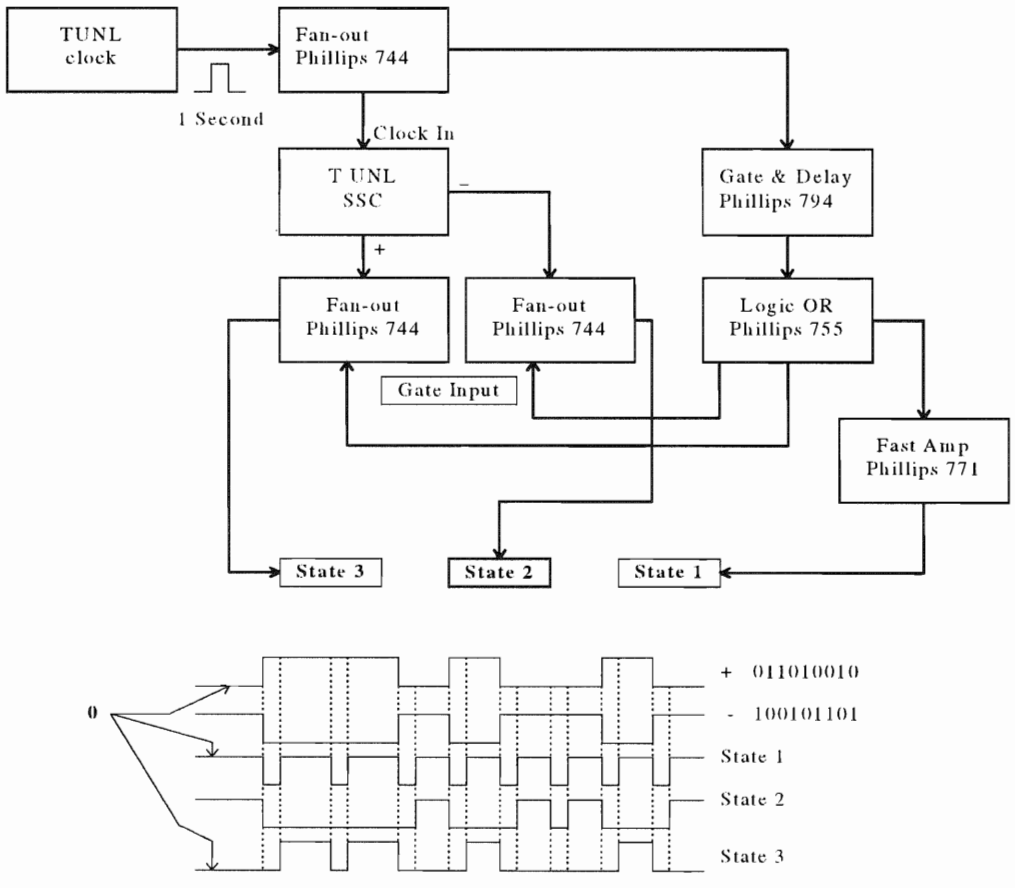

Figure 3.2 Block diagram for generating three-state switching using TUNL SSC module and illustration of the timing relationship among the three polarized states.

The TUNL spin state transition units are driven by a Spin State Control (SSC) module. The module uses an external clock to produce a TTL signal in the repeating step sequence of 10010110, where 1 means transition unit is turned on and 0 means it is turned

off . The time interval for each step is determined by the clock period, which was set to be 1 second for this project. The order of the switching sequence is designed to cancel up to second order spin drifting effects [Kos90].

In order to allow the transition units to recover and achieve a stable state after the spin-state switching, a veto signal of 15 ms is generated to prevent all the data from collection during the state changing period. Standard NIM gate and delay generators are used to generate this signal. The veto signal was fed into the veto control of the sixteen-channel Phillips-706 discriminator. All detector and scalar signals are filtered through this discriminator. The schematic diagram for the scalar signal vetoing is shown in Figure 3.3.

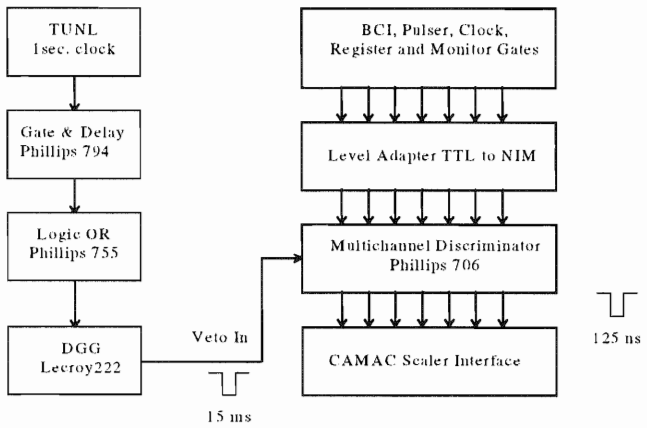

Figure 3.3 Block diagram for scalar interfacing.

The veto gate is also used to inhibit the MBD-11 driver in order to stop all the analog to digital converters (ADC) from working while transition units is not yet stabilized. The SSC module can be used just for driving one transition unit for state switching between polarized and unpolarized states. It is more frequently used to initiate switching between two polarized states. The block diagram for achieving this is shown in

Figure 3.2. The time dependence diagram is also illustrated in the figure. This set-up also allows an arbitrary time allocation among the three spin-states. It is easy to reduce the three-spin-state switching to a two-spin-state switching by simply adjusting the time width of the unpolarized step to be a relative insignificant amount compared with that of one spin step, usually by a factor of 1000 times smaller.

The spin state recognition in the data collection process is achieved by on-line software. The spin switching signals are sequentially fed into two Northern ADC data bit registers. Depending on the value of any two registered spin bits, data are sorted into different storing areas accordingly. A status table for such a process can be given as the following.

	SF2 = On (1)	SF2 = Off (0)
MF2 = On (1)	11 = State-4 (non-existent)	10 = State-2 (Pzz = +1)
MF2 = Off (0)	01 = State-3 (Pzz = -1)	00 = State-1 (unpolarized)

Table 3.1 The switching values for three spin states selections.

3.5 Proton Polarimeter

Since the low energy proton polarimeter was not available at the time present investigation was conducted, the proton polarization measurement was carried out using TUNL 52° scattering chamber and Tandem accelerator. The setup for the measurement is shown in Figure 3.4. The reaction was chosen to be $^4\vec{He}(\vec{p},p')^4He$. It has a well-

determined vector analyzing power whose A_y is close to one at $\theta_{cm} = 125^o$. The calibration value for vector analyzing power was calculated by using phase shift parameters extracted from the previous measurements [Sch71]. The reaction also has a large cross section of about 100 mb at a proton energy of 6 MeV. These properties make it an ideal monitor for measuring proton beam polarizations.

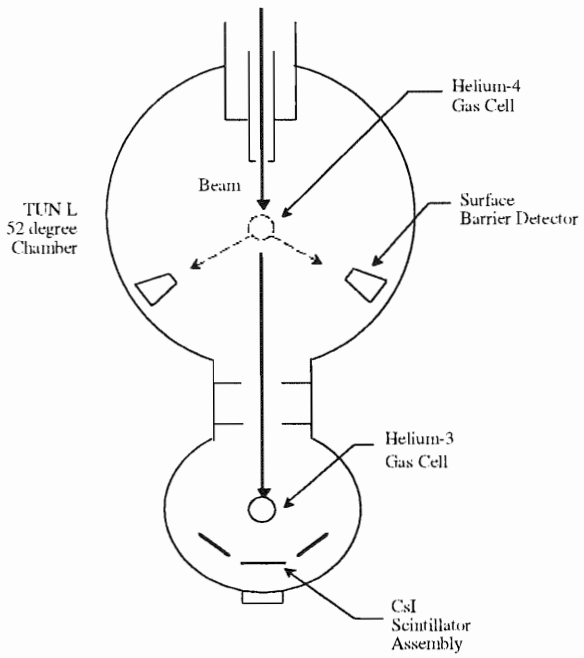

Figure 3.4 The 52° chamber set-up for measuring polarization of either proton or deuteron beam. Top part of the chamber was used for proton polarimeter and bottom part was used for deuteron polarimeter.

The chamber was originally designed for high precision nuclear structure measurement [Ton81]. The beam coming into the chamber was well centered and precisely collimated. The target was chosen to be a ^{4}He gas cell. The wall of the cell for

our measurement was made from thin Havar foil of 2.108 $\mu g/cm^2$ in thickness. The cell was firstly evacuated, expunged, and then filled with pure ^4He gas. The pressure of the cell can reach as high as 1.5 atmosphere under 10^{-6} torr chamber vacuum. Two surface barrier detectors were placed symmetrically at a backward lab angle of 132.2° corresponding to $\theta_{c.m.}$=125°. The electronics set-up for the two solid state detectors are shown in Figure 3.5. Signals for the detector pair were routed into one Northern ADC.

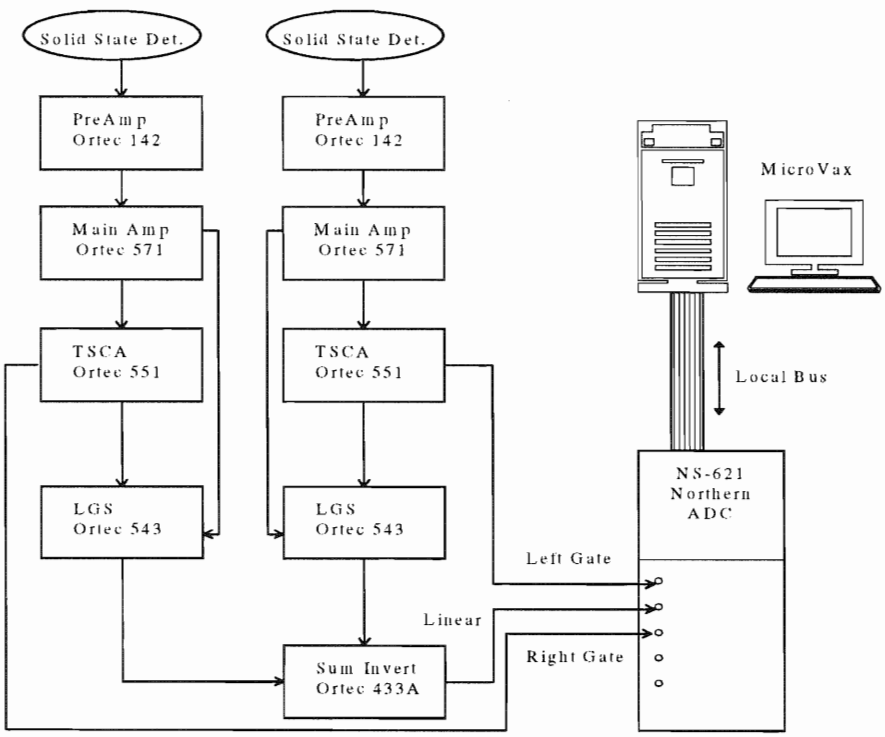

Figure 3.5 Block diagram for two solid state detectors that had been used for polarization monitor measurement.

The energy loss in the Havar foil was calculated by using proton stopping cross section in Havar[Zie84]. A FORTRAN code BABEL from TUNL source library was used [Bow89]. The result indicated that an average of 89.4 keV was lost by 6 MeV

proton beam when penetrating the wall of the gas cell. This loss was adequately compensated by a higher beam energy raised on the tandem accelerator.

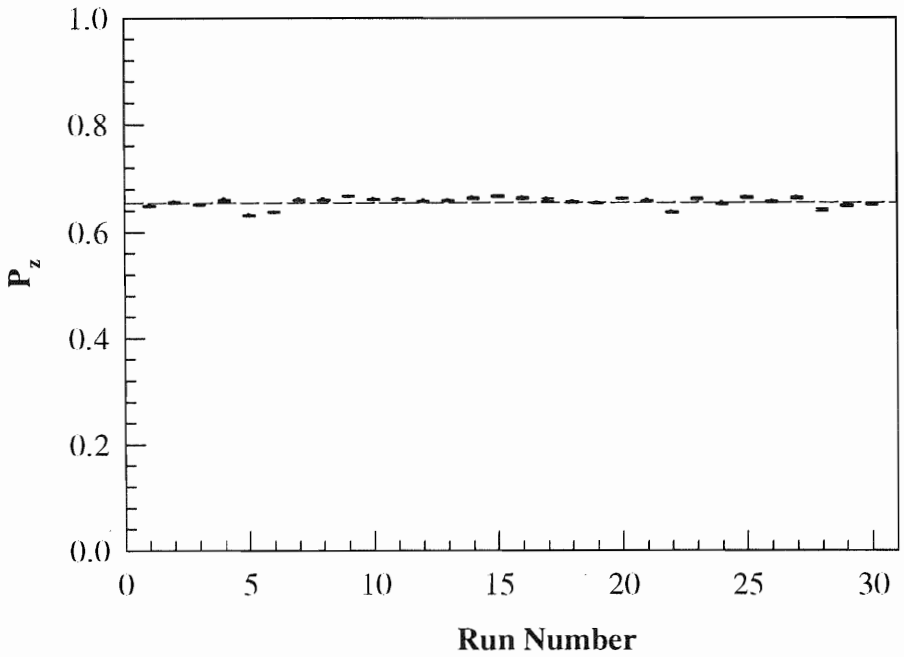

Figure 3.6 Stability of vector polarization for polarized proton beam measurements.

The polarization of the beam was measured by switching the proton beam from LEBAF beam line through Tandem accelerator to high energy beam line on the average of every 6 hours. The result is shown in Figure 3.7. The averaged proton polarization P_z=0.653±0.007. It was found that proton beam polarization is stable and constant within 1% throughout the experiment.

3.6 Low Energy and High Energy Deuteron Polarimeter

The measurements of polarization for deuteron beam was carried out both at high energy and low energy. The high energy polarization measurement was carried out in a small chamber that is immediately behind the TUNL 52 degree scattering chamber using the polarimeter designed by Tonsfeldt [Ton81] (see Figure 3.4). The reaction used was $^3H(\vec{d},p)^4He$ at E_d=10.5 MeV. The outgoing protons are detected in the three small CsI scintillators separated by 24.5° inside the chamber. The center detector was fixed at 0°, i.e. incident beam's direction. This zero degree detector could help to eliminate various misalignment errors. Since at it is placed zero degree, detector is symmetric in x and y direction. A_{xx} equals A_{yy}. By using traceless condition in Equation 3.10, We have

$$A_{xx} = A_{yy} = -\frac{1}{2}A_{zz} \qquad (3.25)$$

Therefore, measurements of A_{zz} or A_{yy} at zero degree can be used to check the results of that from left and right side detectors. The calibration procedures and the electronics set-up for this standard polarimeter are discussed in great details in the reference by Tonsfeldt [Ton81].

While the present proton-deuteron capture project was underway, a low energy $^3He(\vec{d}, p)^4He$ polarimeter for E_d <350 keV was developed [Gei95]. It was calibrated against the high energy polarimeter using the same reaction. At low energies of below 350 keV, the reaction cross section is almost isotropic [Kra87]. Compared with low energy $D(\vec{d},p)T$ polarimeter, it has a much better figure of merit value, which is defined as cross section multiplied by square value of the analyzing powers.

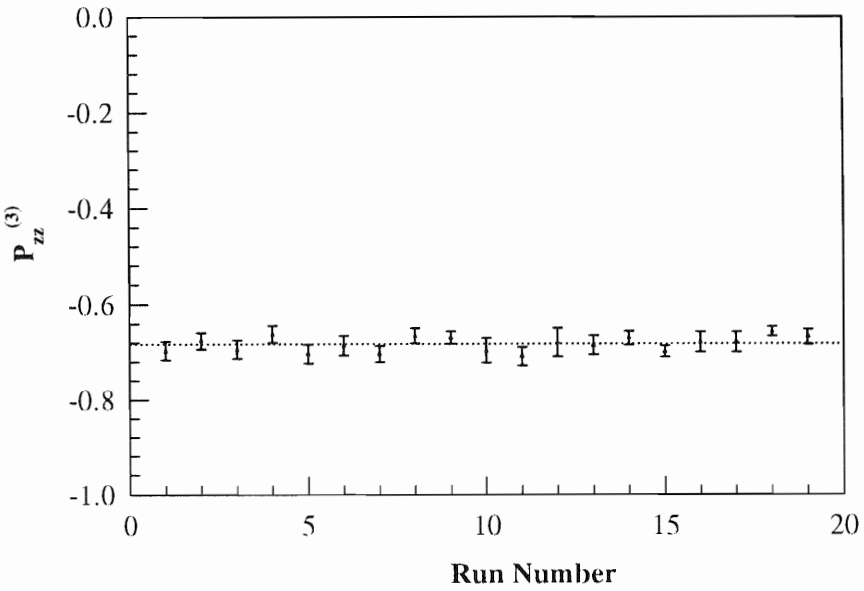

Figure 3.7 Stability of P_{zz} for state-3 transition during one run sequence.

In the low energy polarimeter measurement, a ^{3}He ion implanted target was used for the monitoring reaction [Gei95]. Two surface barrier solid state detector pair were placed symmetrically at a forward lab angle of 30°. The beam size is about 2 cm for the reason of maximizing the beam flux on the target. One polarimeter detector was placed at 0° for the reference measurement. This not only limited the skewness in detector angles caused by the finite size of the beam, but also minimized the angular dependence in the cross section which affected the reaction yield. By using Equations 3.25 and 3.10, P_{zz} was calculated from

$$P_{zz} = \frac{2}{A}\left(\frac{\sigma(0^{\circ})_{polarized}}{\sigma(0^{\circ})_{unpolarized}} - 1\right) = \frac{2}{A}\left(\frac{Y(0^{\circ})_{polarized}}{Y(0^{\circ})_{unpolarized}} - 1\right) \qquad (3.26)$$

where A could be A_{zz} for $\beta = 0^{\circ}$, and A_{yy} for $\beta = 90^{\circ}$ measurement.

Both vector and tensor polarization for the used deuteron beam were measured on an average every 4-6 hours depending on the angular settings of the experiment. Since the low energy polarimeter had not been calibrated for the determination of vector analyzing powers during this work, the vector polarization P_z was determined only from the high energy polarimeter. While the tensor polarization P_{zz} was cross-checked between low energy and high energy polarimeter on a regular basis. A typical time dependence for deuteron tensor polarizations for the two spin-state measurement scheme is shown in Figure 3.7, which is largely coming the low energy polarimeter measurements. The constant averaged polarization agrees well with data within 2.5% of statistical error. The results from both low energy polarimeter and high energy polarimeter measurements are consistently agreed with each other during all the experiment runs. The final averaged P_{zz} is typically -65% for state-3, 67% for state-2, and the averaged P_z is about 28.5%.

IV. Data Analysis and Observables Reduction

4.0 Overview

As described in Chapter 2, high resolution HPGe detectors and vapor condensed thick targets were used throughout this investigation. The beam of the charged particles was completely stopped inside the target. Therefore, the measured observables could in theory be determined for energies ranging from the incident beam energy to zero. The methods for deconvoluting this energy dependence especially in the calculation of the analyzing powers are presented in this chapter. Since all physical effects could not be included rigorously in most of the deconvolution models, approximations were usually made to account for all the major effects influencing the reaction processes. However, it will be shown in this chapter that such approximations could be adequately parametrized and eventually canceled out in the extraction of the energy dependence of the analyzing powers. The reduction of the cross sections data was also carried out.

In this chapter, details of various aspects of the analysis of data are presented and uncertainties in the associated procedures are carefully evaluated. Particularly, the absolute efficiency calibration of the HPGe detectors using both the Monte Carlo simulation and $^{19}F(p,\alpha\gamma)^{16}O$ resonance reaction measurement are described.

4.1 Analyzing Powers Data Analysis

The full angular distributions of vector and tensor analyzing powers for both $^{2}H(\vec{p},\gamma)^{3}He$ and $^{1}H(\vec{d},\gamma)^{3}He$ were measured extensively in the course of this investigation.

The measurement of $^2H(\vec{p},\gamma)^3He$ reaction was carried out at the proton energies of 312 keV and 242 keV corresponding to center of mass energies of 208 keV and 161 keV. Since thick targets were used for both energies, there was an overlap of 40 keV in the energy range covered by these two measurements. From statistical analysis and cross checking, we concluded that data well agreed with each other in the overlapping energy range. The measurements of $^1H(\vec{d},\gamma)^3He$ reaction were carried out at the deuteron energy of 330 keV corresponding to center of mass energy of 110 keV. Two separate measurements of T_{20} were also taken at 90° and 120° for the purpose of cross checking of the consistency of the data. The final results were obtained by taking the error weighted average among all the data sets.

4.2 Kinematics of the Reactions

The energy of the captured γ-rays in the proton-deuteron reactions can be derived by applying the energy and momentum conservation laws. Consider the relativistic constraint on any particle

$$P^2 - E^2 = M_0^2 \qquad (4.1)$$

where P is the momentum of the particle, E is the energy, M_0 is the rest mass (Natural units, i.e. h = c =1, is followed here), the final energy of the γ-ray in terms of projectile energy E_i can be written exactly as

$$E_\gamma(E_i,\theta_L) = \frac{(M_t + M_i + M_r)Q + 2M_t E_i}{2(Q + M_r + E_i - \cos\theta_L\sqrt{(E_i + M_i)^2 - M_i^2})} \quad , \qquad (4.2)$$

where θ_L is the angle between the momenta of incoming projectile and outgoing γ-ray, and M_i, M_t, M_r represent the rest masses of incoming projectile, target nuclei and final recoiled ^{3}He particle respectively. The Q-value can be calculated from the tabulated rest mass of ^{1}H, ^{2}H and ^{3}He. All the masses are known to within 0.5 keV [Wap85]. Since this uncertainty is about an order of magnitude smaller than fluctuations in the beam energy, it was neglected in the determination of the energies of the reaction γ-rays.

An approximation can be made to Equation 4.2 to make it more intuitively transparent. Since in the center of mass frame the projectile and the target particle are moving towards each other with an identical velocity, the total kinetic energy is then given as

$$E_{cm} = \frac{M_t}{M_t + M_i} E_i \qquad (4.3)$$

From energy conservation, the nonrelativistic approximation of Equation 4.2 can be reduced to,

$$E_\gamma = Q + \frac{M_t}{M_t + M_i} E_i - E_{recoil} \qquad (4.4)$$

where the ^{3}He recoil energy E_{recoil} can be estimated as the following

$$E_{recoil} \cong \frac{Q^2}{2M_r} = \frac{(5.5\,MeV)^2}{2(3\times 930 MeV)} \approx 5\ keV\,. \qquad (4.5)$$

Since this value is comparable with the uncertainty in beam energy and it is well within our detection limit, it has to be taken into account when Equation 4.4 is used in energy calibration of the on-line spectra.

From Equation 4.4, the center of mass energy for $^{1}H(d, \gamma)^{3}He$ reaction is very close to one half of that for $^{2}H(p, \gamma)^{3}He$ reaction. A typical spectrum of γ-rays resulting from $^{1}H(p,\gamma)^{3}He$ reaction at E_p= 312 keV is shown in Figure 4.1. One can see that full energy peak at 5.7 MeV, first escape peak at 5.2 MeV and second escape peak at 4.7 MeV and the background is flat and 50 times smaller than the full energy peak.

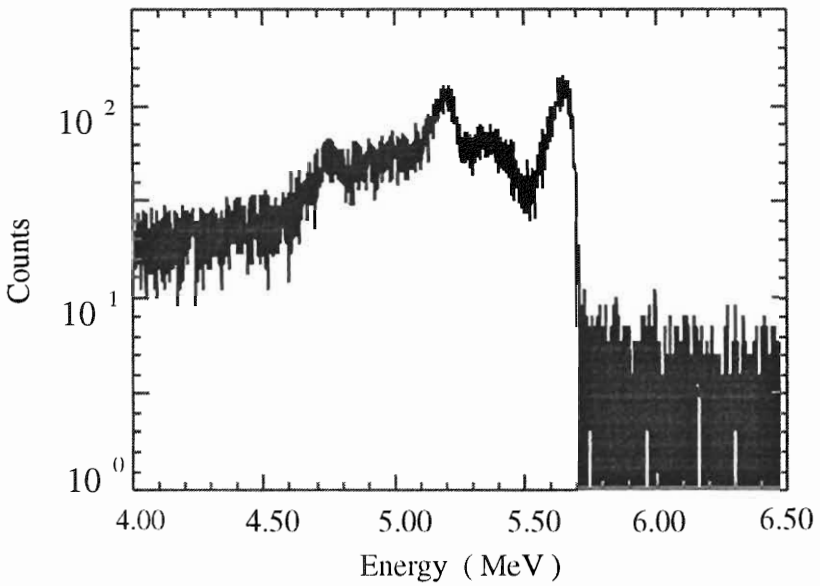

Figure 4.1 Raw spectrum from proton-deuteron capture reaction at E_p=312 keV.

4.3 Energy Calibration

The energy spectrum was calibrated to be approximately 1.1 keV/channel. To determine this calibration, we used standard radioactive γ-ray sources. The γ-ray lines normally used were 0.662 MeV from ^{137}Cs, and 1.173 and 1.332 MeV from ^{60}Co. Two

strong background energy lines were also included in the energy calibrations (see Figure 4.2). They were 1.466 MeV line from ^{40}K and 2.61 MeV line from ^{206}Tl. A linear fit to these energy lines in a spectrum produced the energy calibration in keV/channel with an error less than ± 0.01 keV/channel as shown in Figure 4.3.

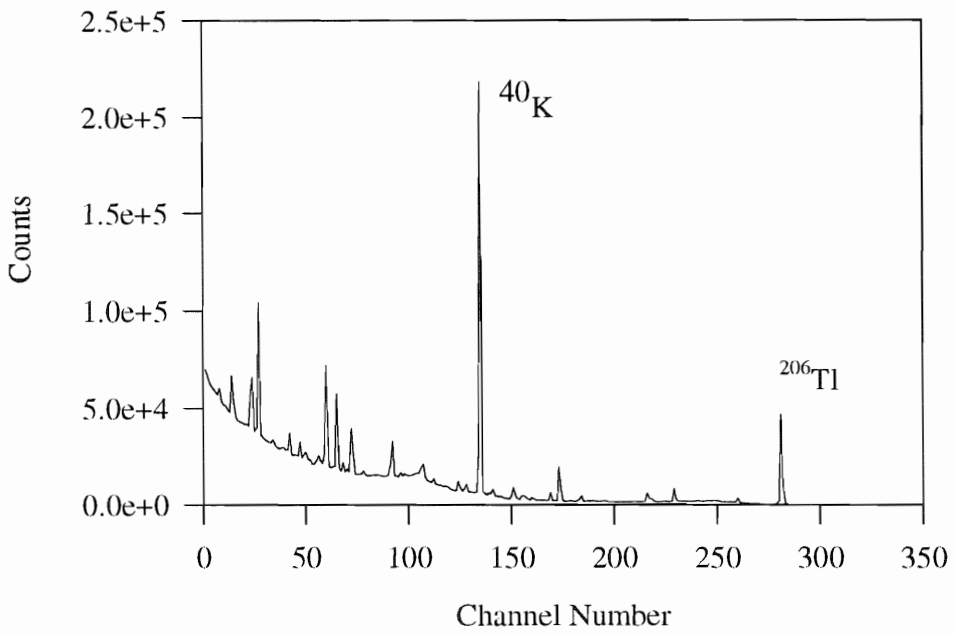

Figure 4.2 Blown-up view of an accumulated on-line background spectrum.

However, even with this precision, the absolute determination of γ-ray energy around 5.7 MeV was not feasible since a radioactive source which produced γ-rays with energy near 5 MeV is not available. The Northern 1215A ADC used for data taking has range of 8192 channels. The gain of the amplifier was adjusted so the 5.7 MeV γ rays

were stored around the channel number of 4500, which is the region of ADC range where response is expected to be most linear. When the linear calibration curve such as shown in Figure 4.2 was used, the propagated error from an uncertainty of 0.01 keV/channel in the slope would have produced an energy shift of 45 keV! Nonetheless, it will be shown below that by using the energy per channel value derived from the above procedures and together with the shape of the full energy peak of the γ-ray spectrum, we could determined the full energies of the detected γ-rays within 2 keV.

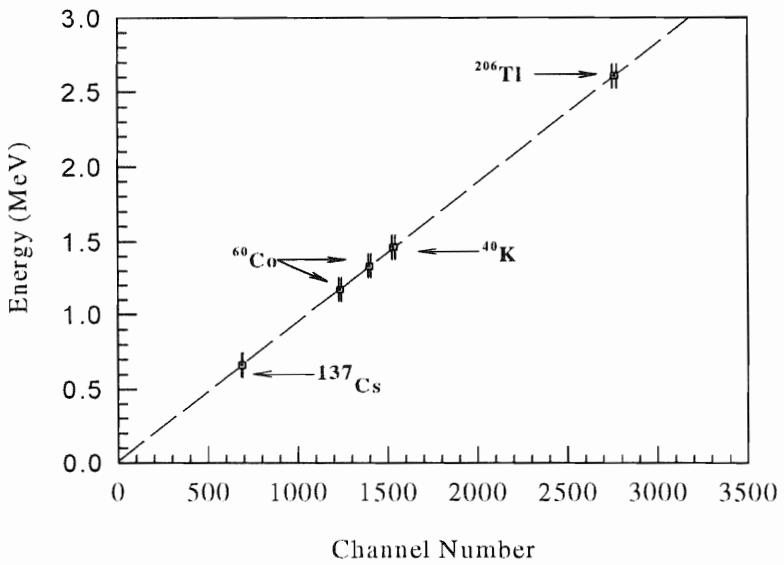

Figure 4.3 Typical energy calibration curve for one spectrum. The line shown here carries an energy calibration of 0.9397 ± 0.0026 keV/channel.

The method for such a compensation is done by using the following equation:

$$E_\gamma = S \times (N_C - N) + 2.61 + E \times \tanh(P), \qquad (4.6)$$

where S is the known value of energy per channel, N_c is the ADC channel number, N is the channel number of 2.61 MeV ^{206}Tl peak, P is the free fitting parameter and E is the adjusting range for E_γ. In another words, by freely adjusting P parameter, E_γ can vary from E_0- E to E_0 + E. The E_0 value corresponds to initial E_γ value if E equals zero. The reason to use hyper tangent function in Equation 4.6 is to allow the varying range of parameter P to be (-∞,+∞). This condition is usually imposed for the sake of avoiding fitting process to converge onto the border value of a fixed range. Since the maximum beam energy corresponds to the falling edge on the high energy end of the full-energy peak (see Figure 4.1), the value of E was usually chosen to cover the extension of this region, which was usually chosen to be 15 keV.

From the low energy side of the full energy peak, contributions from the Compton scattering are coming into the peak. The energy for single photon Compton scattering E_γ^c is given by the following formula,

$$\frac{1}{E_\gamma^{\,c}} = \frac{1}{E_\gamma} + \frac{1}{m_e}(1 - \cos\theta_\gamma) \qquad (4.7)$$

where E_γ is incoming γ ray energy, m_e is the rest mass of single electron (i.e. 511 keV), and θ_γ is the scattering angle between incoming and outgoing γ rays. The minimum of E_γ^c can be calculated by substituting $\cos(\theta_\gamma) = -1$ into Equation 4.7. In the case of $E_\gamma >> m_e$, the minimum of E_γ^c simply equals one half of the electron mass, which is 255.5 keV. From energy conservation,

$$E_\gamma^{\,c} = E_\gamma - E_e \qquad (4.8)$$

where E_e is the recoil energy of the electron. Since the recoiling electron is what generates the detector response, the "edge" of the Compton peak which corresponds to the maximum in E_e hence the minimum in E_γ^c is 255.5 keV below the full energy γ-ray peak. However, after a large number (>10^3 times) of Compton scatterings, E_e could be larger than 255.5 keV. Therefore, part of the detected Compton scattering could in theory overlap with the full energy peak (see Figure 4.1). However, the cross section for Compton scattering is inversely proportional to the square of the incoming γ ray energy, the yield from such a process is expected to be quite small. Nonetheless, it presents an additional background that should be considered together with the background from other sources.

4.4 Background Subtraction

The following approach was used to determine the background for the spectra analysis. The background on the right side of the full energy peak was fitted with a functional of

$$f(E) = (1 + P_1 E)\exp(P_2 + P_3 E) \qquad (4.9)$$

where E is the scaled channel number and P_1, P_2, P_3 are the fitting parameters. Since the background is low and flat in the spectra as shown in Figure 4.1, Equation 4.9 could be adopted to account for the high energy events mostly generated from cosmic rays and other randomly scattered electrons or muons [Leo87].

The experiments were also carried out to test the assumption about the shape of the background. The background spectra were taken for extended period of time first

before all the experimental runs and then after all the runs. The spectra were also taken with beam on target and beam off the target. The typical background yield was calculated be an average of 1.63 counts/channel/hour for the engery range of 500 keV center at the position of full energy peak compared with a value of 1.64 counts/channel/hour around 6 MeV region as shown in Figure 4.1. The results had remained constant for all the experimental conditions.

The beam-induced background was also measured by swapping the target from pure ice (H_2O) to heavy ice (D_2O) target and irradiating it with deuteron beam. The purpose was to observe the neutron background generated from the D(d,n)T reaction. The background in the full energy peak region did not contain any additional peaks and the background yield was consistent with the yield obtained when the beam was off. Therefore Equation 4.9 was used to fit the background on the right side of the full energy peak and it was extrapolated into the region of full energy peak. The multiple Compton background on the left side of the full energy peak was fitted with a fourth order polynomials and also extrapolated into the full energy peak. A cutoff channel number was determined from this polynomial extrapolation so that the multiple Compton background was neglected from this channel on to the right. The total background used in the fitting procedure was solely represented by the extracted background from the high energy side of the full energy peak. It will be argued in the next section that any small leftover effects from the background subtraction and the associated errors could be canceled out for calculating analyzing powers. Nevertheless, proper background subtraction is important for accurate the determination of cross sections.

4.5 Functional Form for Spectra Fitting

The main goal for analyzing thick target yield spectra at different angles is to extract the energy dependence of the analyzing powers. It is very tempting at first to simply extract the total counts from the entire full energy peak for each spin state and then use the total yield to calculate the analyzing powers following the scheme described in the previous chapter. This method is very misleading and generally wrong. It is not justified by the arguments that such results represent the "averaged" analyzing powers in the energy range from zero to the reaction energy.

To illustrate this point, the calculation of vector analyzing power can be used as an example. From Equation 3.7, vector analyzing power A_y can be written as

$$A_y(E) = \frac{1}{P}\frac{\sigma^+(E)-\sigma^-(E)}{\sigma^+(E)+\sigma^-(E)} = \frac{1}{P}\frac{Y^+(E)-Y^-(E)}{Y^+(E)+Y^-(E)} \tag{4.10}$$

The average of the $A_y(E)$ over several beam energy points is given by

$$\begin{aligned} < A_y(E) > \equiv \frac{1}{N}\sum_{i=1}^{N} A_y(E_i) &= \frac{1}{NP}\sum_{i=1}^{N}\frac{Y^+(E_i)-Y^-(E_i)}{Y^+(E_i)+Y^-(E_i)} \\ &= \frac{1}{P} < \frac{Y^+(E)-Y^-(E)}{Y^+(E)+Y^-(E)} > \end{aligned} \tag{4.11}$$

where N is total channel number or number of energy bins in the full energy peak, and the bracket denotes the average of the enclosed variable. In our case, the average size of the

energy step in each channel is 1.5 keV. The direct substitution of the total yield of the full energy peak into Equation 4.10 would give

$$\begin{aligned}
&\frac{1}{P}\frac{\sum_{i=1}^{N} Y^{+}(E_i) - \sum_{i=1}^{N} Y^{-}(E_i)}{\sum_{i=1}^{N} Y^{+}(E_i) + \sum_{i=1}^{N} Y^{-}(E_i)} \\
&= \frac{1}{P}\frac{\sum_{i=1}^{N} [Y^{+}(E_i) - Y^{-}(E_i)]}{\sum_{i=1}^{N} [Y^{+}(E_i) + Y^{-}(E_i)]} \\
&= \frac{1}{P}\frac{< Y^{+}(E_i) - Y^{-}(E_i) >}{P < Y^{+}(E_i) + Y^{-}(E_i) >} \\
&\neq \frac{1}{P} < \frac{Y^{+}(E_i) - Y^{-}(E_i)}{Y^{+}(E_i) + Y^{-}(E_i)} >
\end{aligned} \tag{4.12}$$

It can be seen from Equation 4.12 that any substitution of the yield over a wide energy bin is not physically meaningful for the analyzing power measurements. Since the yield is bound to be small in the beam energy region that is near zero, the practice of choosing a wide energy bin to satisfy the statistical requirements at this region would make the analysis completely useless. Therefore an energy cutoff has to be imposed when thick target yield is used to calculate the analyzing powers away from the effects of the Compton background. The relatively wide energy bin can only be used for the determination of cross section. In this case, the average yield over an energy range largely reflects its "energy averaged" values provided other effects such as target thickness and detector efficiencies are energy insensitive in such an energy bin.

In order to extract the analyzing powers observables, a new method of spectra deconvolution was developed in hte course of this project. It assumes that the observed γ-ray spectrum can be considered to be the convolution of several processes. The shape of the spectra can be described as

$$Y(E) = \int_{E_i}^{E_f} d\xi R(E,\xi) S(\xi) \sigma(\xi) \kappa(\xi) \qquad (4.13)$$

where Y is the energy dependence of the yield, R is the detector response function, S describes the beam stopping effects, σ is the differential cross section, κ describes other small effects which influenced the yield function, for example the fluctuations in beam energies, non-linear response of the ADC's, etc. In the following, we will consider each of these functions separately and describe the associated energy dependences and relevant errors.

4.6 Detector Response Function

The detector response function is determined by the physical processes of photon interacting with HPGe crystal and the design and geometry of the detector. The primary function of the intrinsic response can be described by a standard Gaussian curve [Leo87]. The FWHM of the function is given by

$$\sigma_{total}^{\ 2} = F\sigma^2 + \sigma_{\varepsilon}^{\ 2} \qquad (4.14)$$

where F is the Fano factor, σ^2 is the mean width arising from the ionization processes of incoming photons, the σ_ε^2 describes all the other effects such as electronic noise, drifts, etc.

The response function R(E, ξ) as shown in Equation 4.15 can be analyzed by measuring the peaks obtained from standard mono-energetic γ ray sources [Ald93]. The total response function has be found to have a small low energy tail in addition to the main Gaussian component. This tail is considered to be originating from the finite size of the detector and is mostly caused by the scattered Compton electron and escaping γ-rays. The tail can be written as a linear convolution of a complemented error function with a "modified exponential" [Jor77]:

$$R(E,\xi) = A e^{-0.5(\frac{E-\xi}{\sigma})^2} + (B + Ce^{-\alpha(E-\xi)}) \int_E^{\infty} e^{-0.5(\frac{E-\xi}{\sigma})^2} dE \,. \qquad (4.15)$$

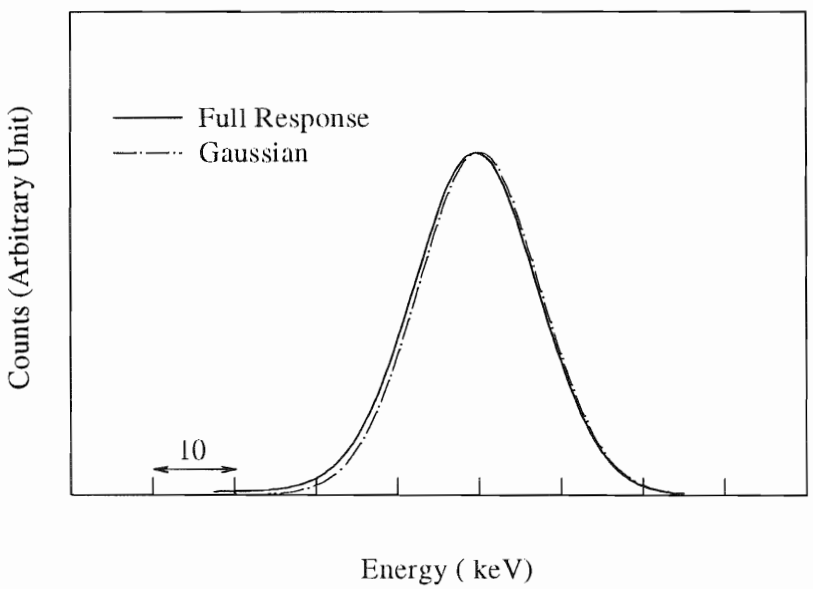

Figure 4.4 The full detector response function calculated from Equation 4.15 compared with a single Gaussian.

The comparison between a normalized single Gaussian and a full response function calculated from Equation 4.15 is shown in Figure 4.4. Since R(E,ξ) is predominantly determined by the leading Gaussian term, Equation 4.15 could be substituted by a Gaussian convoluted with a polynomial expansion (see Equation 4.16). This can be proved by comparing every term in the Taylor expansion between Equation 4.15 and Equation 4.16. The reason for this is largely for expediting the computing speed. The value difference from replacing Equation 4.15 with Equation 4.16 is less than 0.3% numerically. Futhermore, this resulting difference should be cancel out completely for the arguements that will be presented in the later sections.

$$R(E,\xi) = N e^{-0.5(\frac{E-\xi}{\sigma})^2} \sum a_i (E-\xi)^i \qquad (4.16)$$

It should be noted that the Gaussian term in Equation 4.15 should also contain the kinematic width of the γ-ray peak due to the finite size and the geometry of the HPGe detector. Since the detector is cylindrically symmetric, such an effect is expected to be small. The calculation of the kinematic response function of HPGe detector will be further discussed in the next section for cross section calculations. During the fitting process, the total width of the response function was set to be a free parameter. The estimated and final fitted results for such a total width including kinematic response is typically around 15 keV.

4.7 Beam Stopping Effects

The target thickness can be calculated from the hydrogen ions' stopping power in solid D_2O. The stopping powers are the sum of the electronic ionization part and screened nuclei energy loss part. The $S(\xi)$ in Equation 4.13 is given as the following:

$$S(\xi) = \frac{2}{(\frac{dE}{dx})_{\xi}} \qquad (4.17)$$

where the factor 2 comes from the fact that there are two deuterium atoms in one D_2O molecule. The stopping power for hydrogen and its isotopes had been precisely measured and tabulated [Zie85]. The functional form for the stopping power can be written as

For $E \leq 10$ keV $\qquad C_1 E^{0.45-0.5}$ $\qquad (4.18)$

For $E > 10$ keV $\qquad [C_2 E^{-0.45} + C_3 \frac{E}{\ln(1 + C_4 E^{-1} + C_5 E)}]^{-1}$ $\qquad (4.19)$

The high energy behavior of Equation 4.19 is mainly in the form of the Bethe formula. It was considered to be accurate within 5% between 10keV and 1000keV [Zie85].

In the present work, hydrogen ions' stopping power in solid D_2O was calculated using TRIM-92 program, which is capable of generating the stopping power for ions from 10 eV to 2 GeV/amu. The program used the full Monte Carlo method incorporated all the kinetic effects of ions interating with the target solids, e.g., target sputtering, ionization, and phonon production, etc.

The calculated results for the stopping powers of D_2O are shown in Figure 4.5 The data points on the curve are the previously measured values [Wen52].

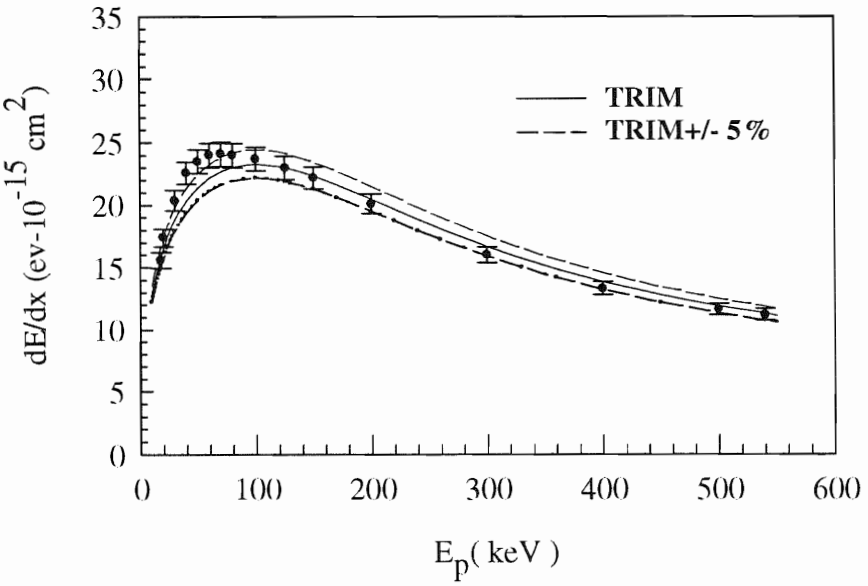

Figure 4.5 The stopping power for solid D_2O from TRIM92 calculations compared with the experimental data from Wenzel and Whaling. [Wen52].

In the TRIM92 calculations, the densities and the chemical structure of the solid D_2O were included *exactly*. From Figure 4.5, it can be seen that TRIM92 curves agree with the measured data within 5%.

4.8 Cross Section Expansion

The cross section $\sigma(E)$ in Equation 4.10 can be expanded into its S factor definition. (Note that this definition is in the center of mass frame while Equations 4.15-4.16 are in the lab frame. Necessary conversions should be done before Equation 4.13 can be used.) Since the proton-deuteron capture reactions are non-resonant, the S factor can be parametrized into polynomial expansions [Rol88]. Typically a linear form of the energy dependence for S factor is sufficient to describe its behavior. The total cross section $\sigma(E)$ can be written as

$$\sigma(E) = \frac{P_0 + P_1 E}{E} \exp(-2\pi\eta) \qquad (4.20)$$

where P_0 and P_1 are the linear coefficients. Typically P_1 is about two orders of magnitude smaller than P_0 for proton-deuteron capture reactions [Rol88].

If we expand the last term κ in Equation 4.13 into its Maclaurin series and combined with Equation 4.20, we have

$$\sigma(E)k(E) = \frac{\sum P_i E^i}{E} \exp(-2\pi\eta) \qquad (4.21)$$

where P_i's in Equation 4.21 become the deconvoluted parameters that we are after.

As it has been shown in Chapter 3, all the analyzing powers can be calculated from a function (i.e. asymmetry) involving only the *ratios* of any two spin-state cross sections. Therefore, any spin-independent effects can be canceled out from the numerator and denominator. Even certain spin-dependent effects could also cancel each other. Considering vector analyzing power A_y reduction as an example, it can be calculated through

$$A_y = \frac{1}{P}\frac{\sigma^+ - \sigma^-}{\sigma^+ + \sigma^-} = \frac{1}{P}\frac{(\frac{\sigma^+}{\sigma^-}) - 1}{(\frac{\sigma^+}{\sigma^-}) + 1} \equiv \frac{1}{P}\frac{\tau - 1}{\tau + 1} \tag{4.22}$$

where

$$\tau \equiv \frac{\sigma^+(E)}{\sigma^-(E)} = \frac{\sigma^+(E)k(E)}{\sigma^-(E)k(E)} = \frac{\frac{\sum P_i^+ E^i}{E}\exp(-2\pi\eta)}{\frac{\sum P_i^- E^i}{E}\exp(-2\pi\eta)} = \frac{\sum P_i^+ E^i}{\sum P_i^- E^i}. \tag{4.23}$$

In Equation 4.23, κ(E) can be interpreted as accounting for the non-zero spin-independent effects such as uncertainties in the detector response function, small beam energy shifts, etc. A spin-dependent effects in the form of g(E)σ(E), such as *small* Compton background, can be also canceled. It goes as the following,

$$\tau \equiv \frac{\sigma^+(E)}{\sigma^-(E)} = \frac{\sigma^+(E)k(E) + g(E)\sigma^+(E)}{\sigma^-(E)k(E) + g(E)\sigma^-(E)} = \frac{\sum P_i^+ E^i}{\sum P_i^- E^i} \tag{4.24}$$

provided that κ(E)+g(E) ≠ 0 locally. Since we are not dealing with the zero yield from the definition of Equation 4.13, these convoluted effects should satisfy the non-zero condition. Because $P_1 << P_0$ in Equation 4.20, the linear sum in Equation 4.21 was normally truncated only to the second order in energy.

4.9 Fitting Algorithm

The function fitting using Equation 4.13 was carried out using libraries in MINUIT routines for least square minimization[Jam77]. The data was user-interfaced with Physics Analyzing Workstation (PAW) package [Bru93]. The entire calculation was performed

under Sun0S system V. One typical linear regression process took about 2-4 hours of CPU time.

The minimization was performed by reducing the least-square error distribution, i.e. chi-square distribution, which is given in the form of

$$\chi^2 = \sum_{i,j} (y_i - f(x_i, \vec{\alpha}))E_{ij}(y_j - f(x_j, \vec{\alpha})). \qquad (4.25)$$

In Equation 4.25, y is the measured number of counts for each channel (or energy bin) in the spectrum, i and j are the bin labels, f is the fitting function which is in the form of Equation 4.13. Its independent x variable is the center of mass energy or the scaled channel number in the spectra and $\vec{\alpha}$ is the vector of the fitting parameters. E_{ij} is the weighting matrix i.e. the inverse error matrix. If all the measured variables are uncorrelated, Equation 4.25 is reduced to

$$\chi^2 = \sum_i \omega_i |y_i - f(x_i, \vec{\alpha})|^2 \qquad (4.26)$$

where ω_i is the positive weighting factor. If the errors in measured y_i's follow a normal distribution, which is generally true from the central limit theorem, then ω_i can be replaced by the inverse of the estimated variance from the error distribution. Our goal is to find out the unconstrained local minimum of χ^2 defined in Equation 4.25, which means find $\vec{\alpha}$ such that $\frac{\partial \chi^2}{\partial \vec{\alpha}} = 0$.

There are many numerical methods for searching for the minimum (or maximum) of a general function [Gil81]. Two algorithms had been tried during this project. The first one is the brute force grid searching method. The idea is to map the whole function with a

fine grid, calculating the value of function at each grid point and comparing among the results from its neighbor points. In order to improve the efficiency of the search, Monte Carlo method is usually adopted to sample the entire grid.

The other way is to follow the natural derivative condition of Equation 4.26. The minimization starts from calculating a trial point of the function. From this point, the gradients in all directions are calculated. A small step is then made to follow the changing course of the gradients. Through regression process, the minimum is determined through trial and error. In practice, we adopted the most useful searching algorithm of this type which was invented by Nelder [Nel65]. It is based on the calculation of the simplex of the function. A simplex is the "simplest" figure consists of only n+1 vertices in the n dimensional space. For example, a simplex in two dimensional space is a triangle. The simplex method starts by calculating the center of mass point of a chosen simplex of the function. After comparing this point with all the vertices of the simplex, a new simplex is formed around a new direction which always points from the highest value to the lowest value of all the vertices. The stepping size can be adjusted to fit into the local structure of the function. If the function has a large slope, the size of the step can be chosen to be much larger than the one which has a shallow bottom. Since the method was designed to take as large a step as possible, it is very robust against the various occurring rounding errors in the calculation process. The method is concentrating in its search on the general "flow" of the function rather than on the fine structure of it. The convergence time of the simplex method is much shorter than that of the Monte Carlo grid search method. It was also found that during the fitting calculations the error matrix from the simplex method is

much more stable than that derived from other methods. Therefore, the simplex method was selected to perform the final iterations associated with the calculations of the error matrix. In some cases, several schemes were tested to see which one works the best before the final iteration was implemented.

It should be mentioned that if the function *f* in Equation 4.25 is not too complicated such as a short linear form, Equation 4.26 can be solved directly rather than by going through the searching analysis. The final χ^2 at minimum divided by the total number of degrees of the freedom is typically 1.0-1.3 for all the fitted spectra. A typical fitted spectrum is shown in Figure 4.5.

Since two sets of measurements of the vector analyzing powers at the same energy range of $E_{c.m.}$=120-160 keV for $^2H(\vec{p}, \gamma)^3He$ reaction were performed, the Student-t test was applied to check if the mean values obtained from these two sets of data were in agreement with each other. The calculation was performed under the Mathematica statistical analysis package [Wof91]. The confidence level for the two data sets agreeing in their mean values are in the range of 79%-92%. This value also proved the robustness of the deconvolution analysis method applied in this work.

An alternative method of searching for the functional parameters is to minimize the maximum likelihood function [Lyo86]. This function is given as

$$\ell = -\sum_i w_i \log f(x_i, \vec{\alpha}). \qquad (4.27)$$

where w_i is the weighting factor. The function *f* in Equation 4.27 has to be adequately normalized. A constant is usually added to right side of Equation 4.27. Since this constant is α dependent, it affects the convergence of the calculation extensively. Due to

the complication in the error calculations from this method [Roe92], it was not implemented in the practical calculations.

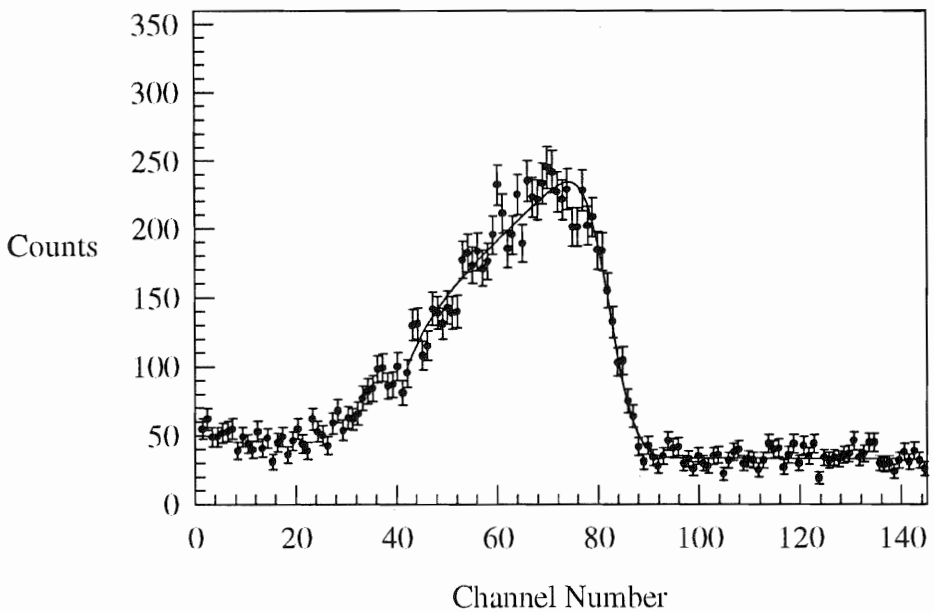

Figure 4.5 The full energy γ-ray spectrum from $^2H(\vec{d}, \gamma)^3He$ reaction detected at 90° for one spin state. The functional fit shown here has a $\chi^2/nf = 1.2$. The error bar on the data points is $\sqrt{N}$, where N is the number of counts in each channel.

4.10 Error Analysis for Analyzing Powers

Usually, the error matrix for the fitting parameters is defined as the inverse of the covariance matrix. It is given by

$$E_{ij} \equiv V_{ij}^{-1} = \{\overline{(\alpha_i - \overline{\alpha_i})(\alpha_j - \overline{\alpha_j})}\}^{-1} \qquad (4.28)$$

where E_{ij} is the error matrix, overbar denotes the statistical estimate of the parameters, and V is the covariance matrix.

By taking the partial differentials on both side of Equation 4.28 , V can be calculated from

$$V_{ij} = \frac{1}{2}\frac{\partial^2 \chi^2}{\partial \alpha_i \partial \alpha_j} \qquad (4.29)$$

Since the parameters in the fitting function are usually correlated, the interpretation of the error in the fitting procedure should take this into account. For χ^2 defined in Equation 4.25, one standard deviation (1σ confidence level) corresponds to χ^2-χ^2_{min}=1. It is assumed that near minimum, the χ^2 behaves approximately like a quadratic function, and the diagonal terms of the error matrix include the effects of the correlation [Roe92]. The total error at a given interpolated point of the fitting function is then given by

$$\sigma = (\sum_{i,j} \frac{\partial \chi^2}{\partial \alpha_i} V^{-1}{}_{ij} \frac{\partial \chi^2}{\partial \alpha_j})^{\frac{1}{2}} \qquad (4.30)$$

The error calculated from Equation 4.30 is a function of energy and it formed an error band around the fitted curve (see next chapter for the details of the error reduction results). Since the fitting function *f* is parametrized as the polynomial energy expansion in Equation 4.13, the two ends of the error curve are dominated by the uncertainties in the coefficients from the higher order terms in the energy expansion. At the center part of the curve, errors are dominated by the uncertainties in the lower order terms in energy. As a result, the error band is wider at the ends and narrower at the center. Experimentally, it

can be seen that the number of counts in each channel is much smaller at the ends of the spectrum than in the center (see Figure 4.1) , the statistical error is therefore much larger there than in the center of spectrum. The error curve should inherently represent this trend.

The errors for the final analyzing powers are propagated from the calculated functional error curves for each spin states. The formula for the error propagation of the function f(x, y) is given by

$$\sigma_f = \sqrt{(\frac{\partial f}{\partial x})^2 \sigma_x{}^2 + (\frac{\partial f}{\partial y})^2 \sigma_y{}^2 + 2\rho(x,y)\sigma_x\sigma_y} \qquad (4.31)$$

where ρ(x, y) is the correlation coefficient defined as

$$\rho(x,y) = \frac{\sqrt{\mathrm{cov}(x,y)}}{\sigma_x \sigma_y} \qquad (4.32)$$

The correlation coefficient can be estimated over all sets of the measured runs at each angle. When written in explicit form, it becomes

$$\rho(x,y) = \frac{\overline{(x-\bar{x})(y-\bar{y})}}{\left(\overline{(x-\bar{x})^2 (y-\bar{y})^2}\right)^{\frac{1}{2}}} \qquad (4.33)$$

For vector analyzing powers shown in Equation 3.7, the error of the η ratio for the different spin states was calculated by directly applying Equation 4.31. The error for A_y is finally given as

$$\Delta A_y = \left(\frac{(P_z^+ - P_z^-)^2}{(P_z^+ - \eta P_z^-)^4} (\Delta\eta)^2 + \frac{A_y{}^2}{(P_z^+ - \eta P_z^-)^2} (\Delta P_z^+)^2 + \frac{(A_y \eta)^2}{(P_z^+ - \eta P_z^-)^2} (\Delta P_z^-)^2 \right)^{\frac{1}{2}} \qquad (4.34)$$

For A_{zz} given in the formula of Equation 3.16, the error calculation is in a similar form, i.e.,

$$\Delta A_{zz} = \left(\frac{4(P_{zz}^{(3)} - P_{zz}^{(2)})^2}{(P_{zz}^{(3)} - \eta P_{zz}^{(2)})^4} (\Delta\eta)^2 + \frac{A_{zz}^{\ 2}}{(P_{zz}^{(3)} - \eta P_{z}^{(2)})^2} (\Delta P_{zz}^{(3)})^2 + \frac{(A_{zz}\eta)^2}{(P_{zz}^{(3)} - \eta P_{zz}^{(2)})^2} (\Delta P_{zz}^{(2)})^2 \right)^{\frac{1}{2}} \quad (4.35)$$

The error calculation for A_{yy} given in Equation 3.23 is a little bit more complicated. Even though it is possible to calculate the inverse of the matrix and expand the formula explicitly, such an expansion tested in the MathCAD environment would extend for about 5 pages in length! Fortunately, by using the symbolic substitution technique [Wol92], the error for A_{yy} can be calculated numerically at each energy point. Its representation can be put into the following form:

$$\begin{aligned} \Delta^2 Ayy = & \left([0 \quad 1] \frac{\partial \mathbf{P}^{-1}}{\partial r} \begin{bmatrix} 1-r \\ \\ 1-l \end{bmatrix} + [0 \quad 1] \mathbf{P}^{-1} \begin{bmatrix} -1 \\ \\ 0 \end{bmatrix} \right)^2 \Delta^2 r \\ & + \left([0 \quad 1] \frac{\partial \mathbf{P}^{-1}}{\partial P_{zz}^{(2)}} \begin{bmatrix} 1-r \\ \\ 1-l \end{bmatrix} \right)^2 \Delta^2 P_{zz}^{(2)} \\ & + \left([0 \quad 1] \frac{\partial \mathbf{P}^{-1}}{\partial P_{zz}^{(3)}} \begin{bmatrix} 1-r \\ \\ 1-l \end{bmatrix} \right)^2 \Delta^2 P_{zz}^{(3)} \end{aligned} \quad (4.36)$$

The error Δr in the equation can be calculated by following the formula of Equation 4.32. It should be noted that each matrix derivative in Equation 4.36 has to be applied to every component of the P matrix, which is defined in Equation 3.22.

4.11 Cross Section Data Analysis

The cross section data analysis is more complicated than the analysis of analyzing power data by the presence of various interaction processes and the energy dependence of the target thickness. The errors are compounded from each of the steps. To ensure that the statistical errors will be adequate to achieve our goal for comparison with the previous measurements, the total cross section was calculated from only four energy bins where yield are the highest.

4.12 Target Thickness and Beam Integration

The target thickness in the unit of number of atoms per cm^2 was calculated using the following equation

$$n = 2\frac{\rho_w}{w} N_A \int_{E_i}^{E_f} \frac{dE}{\left(\frac{dE}{dx}\right)} \qquad (4.37)$$

where ρ_w is the mass density for solid D_2O, w is its atomic weights (D_2O=20), N_A is the Avogadro constant. The stopping power dE/dx was calculated by using TRIM92 code as described in the previous section (see Figure 4.4). The total number of ions generated for each point in the TRIM92 calculation is typically equal to 10^7.

The integration in Equation 4.37 was performed numerically by using the output dE/dx data table from TRIM92. If we set $E_i = 0$ and $E_f = E$, then the integration result is a function of E and it represents the maximum distance of a hydrogen or deuterium ion of energy E could travel in solid D_20. The calculated curve for this distance as a function of E is shown in Figure 4.6.

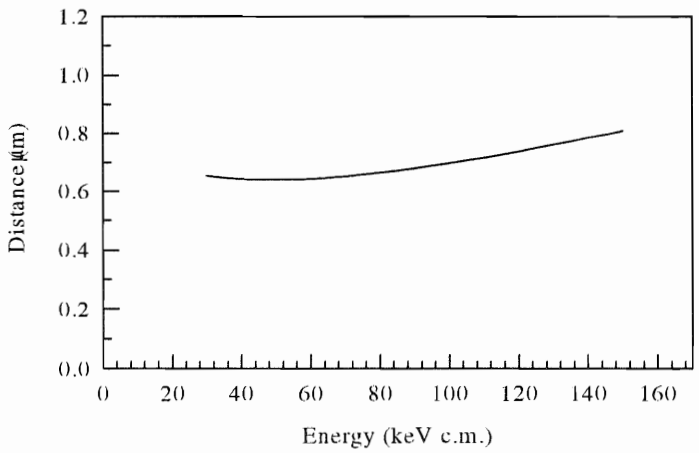

Figure 4.6 The energy dependence for the integrated distance from D_2O stopping power.

We eventually used this curve to determine the target thickness in Equation 4.37. It can be calculated as the following

$$n = 2\frac{\rho_w}{w} N_A \int_{E_i}^{E_f} \frac{dE}{\left(\frac{dE}{dx}\right)} = 2\frac{\rho_w}{w} N_A \left(\int_{0}^{E_f} \frac{dE}{\left(\frac{dE}{dx}\right)} - \int_{0}^{E_i} \frac{dE}{\left(\frac{dE}{dx}\right)}\right) \qquad (4.38)$$

For an energy bin of 20 keV around 173 keV center of mass energy, we can substitute E_i =153 keV and E_f =193 keV into Equation 4.38 and obtained the target thickness to be 5.436×10^{18} D/cm^2. Similarly, at 133 keV, it yields 4.813×10^{18} D/cm^2.

The total charge collected on the suppressed target can be extracted from the charge measured in the Beam Current Integrator (BCI). To ensure that the charge collection is stable and the target thickness has no deterioration, the yield of the full energy

γ-ray spectra was constantly monitored. A plot of normalized detector counts versus sequential run numbers is shown in Figure 4.7.

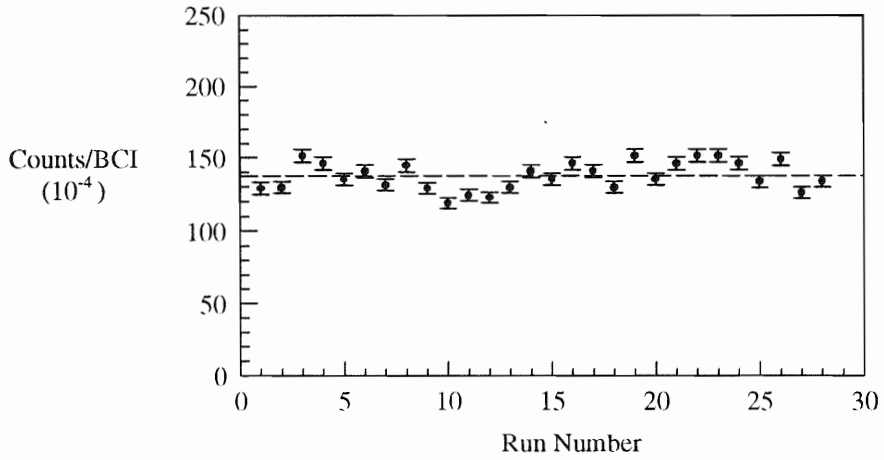

Figure 4.7. Time dependence of BCI normalized γ-ray yield from $^{2}H(p, \gamma)^{3}He$ reaction. The constant line is the mean value reference line. Each run number corresponds on average to a period of 6 hours.

We can see from Figure 4.7 that the count rate is a constant function of time. The total number of the incoming particles collected at each angle is on the average close to 1.5×10^{18}. Since the target was recycled all the time and the yield of the reaction stayed constant, the sputtering and charge loss processes were neglected in the analysis.

4.13 Detection Efficiencies and Geometric Corrections

The total γ-ray detection efficiency can be expressed as a product of the absolute detection efficiency ε and the geometric factor. The absolute detection efficiency associated with HPGe detector full energy peak arises from the physical electron-hole generating process in the Ge crystal. The full energy peak entails all the processes that deposit the total energy in the active volume of the crystal. They can either resulted from a single interaction or from multiple events. The geometric factor includes the solid angle of the detector, the finite size of the target, and the attenuation from the aluminum wall of the target chamber.

Although variations in the beam profile can affect the effective size of the target, This is generally a small effect and a uniform beam distribution is assumed in the calculation. The aluminum attenuation effects from the wall of the chamber and the thin capping in front of the detector were included in the calculation giving a correction of the order of 0.7%.

The extraction of the geometric factor for the experiment was performed using Monte Carlo simulation which takes into account all the aspects of γ-ray transport in the detector. The simulation is initiated by a γ-ray randomly generated with a finite-size target. The diameter of the target size was assumed to be the same as the beam spot on the target, which was measured after the experiment.

The full experimental geometry was modeled using the GEANT3.15 code [Bru93]. The γ-rays were sent into the hemisphere of the solid angle equals to 2π following the angular distribution of $a+b\sin^2\theta$. This is a very good approximation to the real emission

from proton-deuteron capture as the observed radiation is predominantly due to E1 transition.

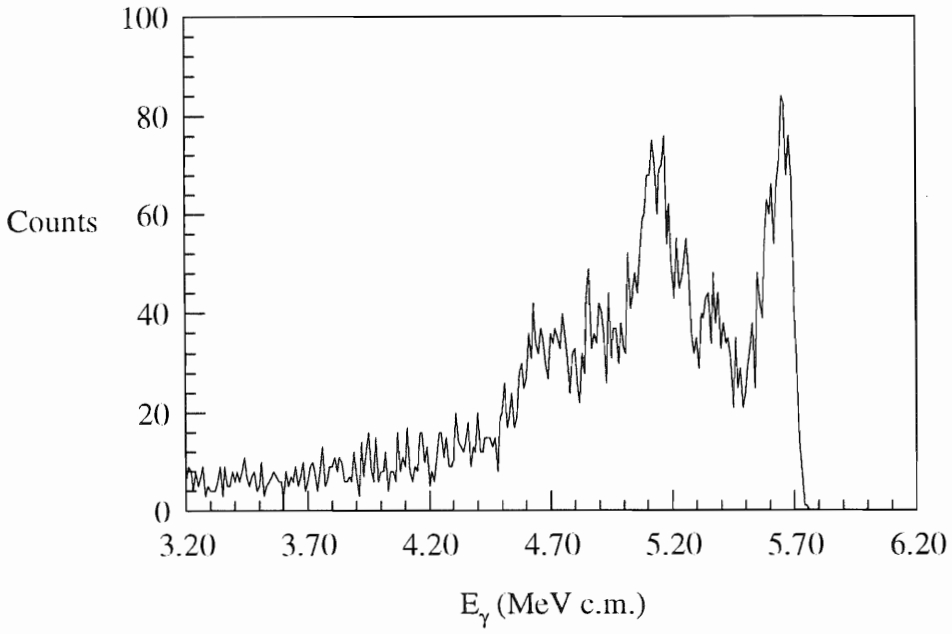

Figure 4.8 The simulated γ-ray spectrum for $^2H(p,\gamma)^3He$ reaction at $E_{c.m.}$= 200 keV. The full dynamics is included in this calculation, in which energy dependence of the cross section (or S-factor) was taken from the previously extracted functional form [Rof88].

An example of the energy spectrum obtained from the simulation is shown in Figure 4.8. The total sample size is typically 10^6 γ-rays originating at the target site. The geometric efficiency was calculated by taking the ratio of all tracked photons which struck the detector to the total number of photons generated at the target site. This ratio was

then normalized to 4π sr solid angle. Aside from the negligible energy dependence of the attenuation coefficient of the aluminum, the calculated geometric efficiency is an energy independent constant. The typical value for our setup has a geometric efficiency of 0.015.

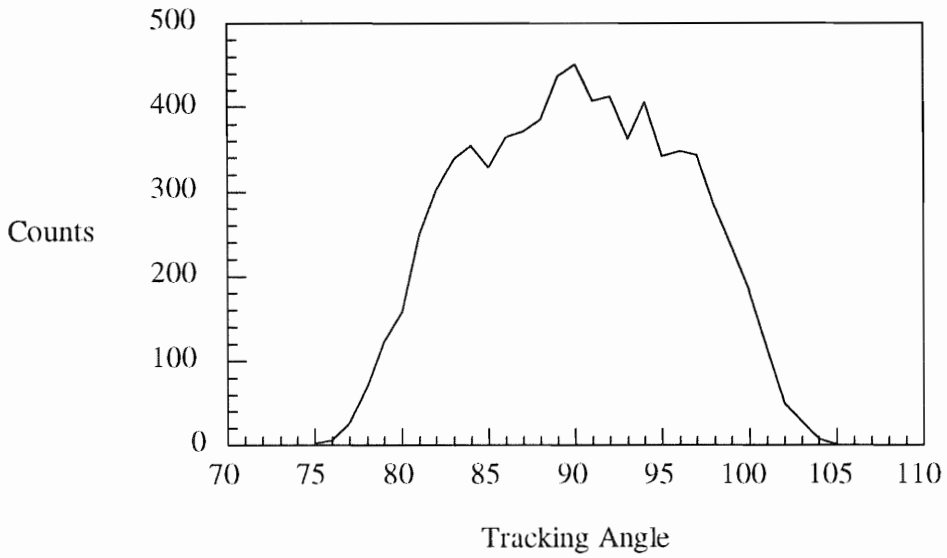

Figure 4.9 Calculated distribution of γ-rays for the HPGe detector placed at 90° lab angle.

The GEANT3.15 code has also been used to determine the kinematic distribution of the γ-rays for the HPGe detector. During the simulation, the angles for the outgoing γ-rays could be simply tracked as additional parameters in the output ntuple events. The kinematic distribution of γ-rays which interact with the detector is shown in Figure 4.9. The kinematic distribution has a maximum at the lab angle of 90°, and it is symmetric with respect to the center axis of the detector as expected.

The absolute efficiency ε of a HPGe detector for monoenergetic γ-rays detection can be calculated through Monte Carlo modeling. It is straightforward to track all the energy deposited inside the HPGe detector by the GEANT3.15 code and use the total counts in the full energy peak to calculate ε. The determination of ε has been performed assuming a monoenergetic γ-ray source of the energy of 5.7 MeV. ε was calculated by taking the ratio of total γ-ray counts in the full energy region with an low energy cut of 5.4 MeV to the number of the total tracked γ-rays each including at least 10^6 events. We obtained an averaged value of 0.0964 for 6 runs of full simulations. Another independent Monte Carlo simulation using EGS4 code [Nel85] had obtained a value of 0.098 [Sch95], which is a quite remarkable agreement considering completely different implementation schemes and computing platforms involved in each of the two codes.

However, it is very difficult to fully simulate the thick target yield by generating γ-rays from the target site in the present real case. The problem arises from the fact that the energy dependence of the sampling distribution should be known beforehand in order to treat the emission of varying energy γ-rays exactly. However, this distribution is none other than the energy dependence of the cross section which we are trying to measure!

In order to determine the absolute detector efficiency experimentally, two separate measurements were conducted. The first one used the calibrated γ-ray source, and the other one used a resonance reaction of known properties. In the first method, a calibrated γ-ray source manufactured by Amersham Corporation (code name QCD.1) was placed at the target site. The radioactivity of the source was derived using the well known half-lives of the elements constituting the source. Three γ-ray energy lines were used: i.e. 1.17

MeV, 1.33 MeV from ^{60}Co, and 1.86 MeV from ^{88}Y. The solid angle for the measurement was also calculated using the Monte Carlo simulation just like in the case of the finite beam size described above. The final absolute efficiency ε was extracted using the following formula:

$$\varepsilon = \frac{N_{det}}{N_0 (\frac{1}{2})^{\frac{t}{T}} \Omega} \quad , \qquad (4.38)$$

where N_{det} is the number of the detected γ-rays, N_0 the initial activity of the source, T is the half-life, t is the time difference between the source manufactured time to the experimental usage time, and Ω is the solid angle.

In the second experiment, an in-beam determination of ε was performed using the resonance reaction of ^{19}F(p,αγ)^{16}O. This reaction emits γ-rays with energy of 6.13 MeV (see spectrum in Figure 4.10). The recoil α particle carries the energy of 1.7 MeV. In the experiment, coincident α particles and γ rays at the resonance proton energy of 340.46 keV were detected simultanesouly.

The emissions of γ rays and α particles are isotropic in the center of mass frame. The efficiency can be calculated from

$$\varepsilon_\gamma = \Gamma \frac{N_\gamma (DTC)_\gamma}{N_\alpha (DTC)_\alpha} \frac{d\Omega_\gamma}{d\Omega_\alpha} \qquad (4.39)$$

where Γ is the kinematic corrections to account for the fact that γ-ray and α-particle detectors are placed at different angles in the center of the mass frame.

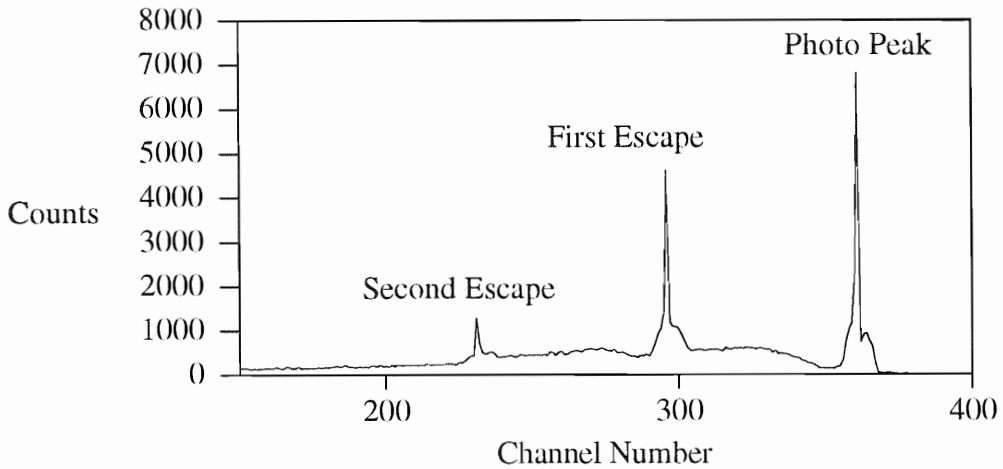

Figure 4.10 γ-ray spectrum from $^{19}F(p, \alpha\gamma)^{16}O$ resonance reaction at 340 keV.

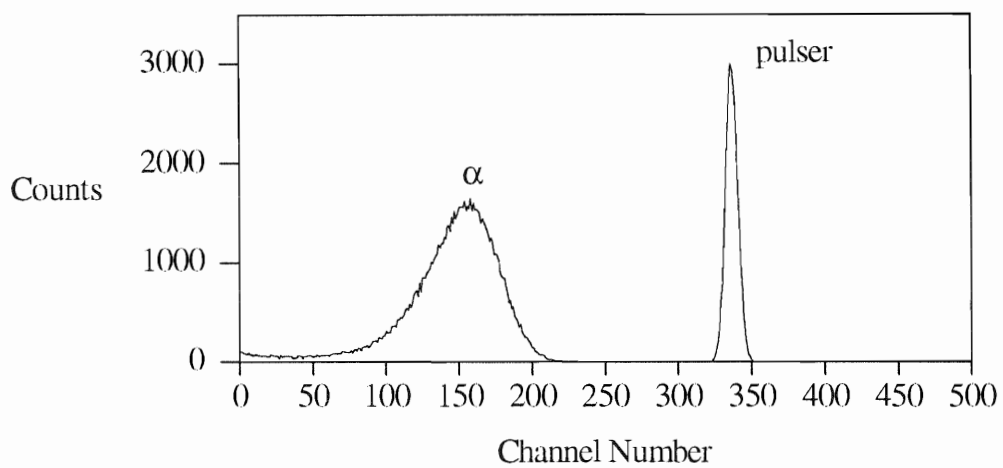

Figure 4.11 Detected α-particles from $^{19}F(p, \gamma\alpha)^{16}O$ reaction. The pulser peak in the spectrum are used for gain adjusting of the amplifiers and dead time measurement.

N_α and N_γ are the number of detected α-particles and γ-rays respectively. DTC_α and DTC_γ denote the dead time corrections, and $d\Omega_\alpha$ and $d\Omega_\gamma$ are the geometric factor for each detector. The absolute efficiency of α-particle detected by solid state detector was assumed to be 100%.

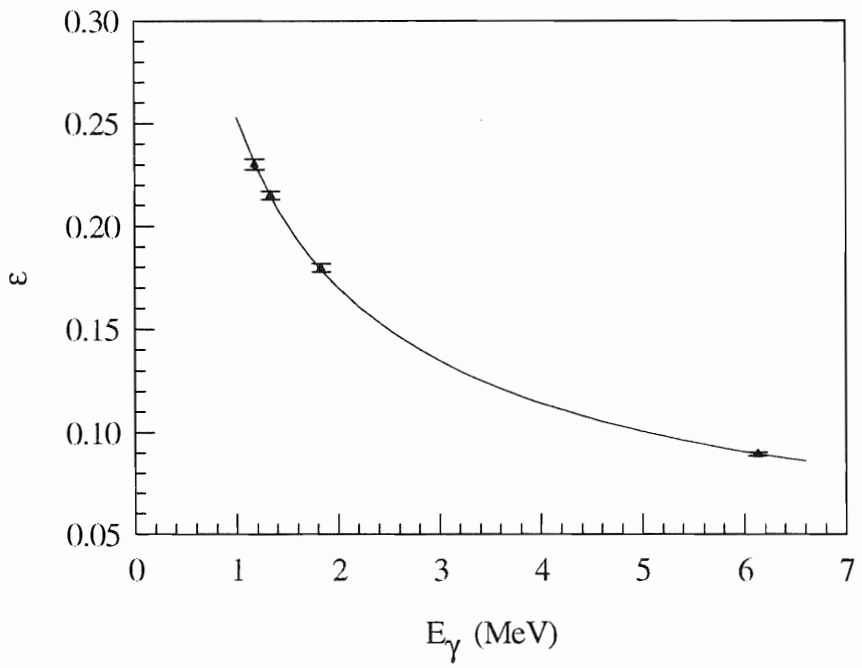

Figure 4.12 The energy dependence of absolute photo peak efficiency for 128% HPGe detector. The exponential fit to the data has a reliability $R^2 = 0.998$.

During experiment a thin Ni foil of 1.7 μm in thickness was placed in front of the surface barrier α detector. It served as the stopping foil for blocking the elastic scattered

proton beam, while still allow the α particles to pass through. In the spectrum shown in Figure 4.11, the α particle peak can be easily evaluated.

The final measured absolute photo-peak efficiencies at different energies are fitted with exponential function in the form of P_1*E**P_2, where P_1 and P_2 are the fitting parameters (see Figure 4.12). The fitting form is expected to be valid for γ-ray energies above 1.0 MeV [Ort95]. The resulting values of the parameters are P_1= 0.253±0.0019, P_2 = –0.5739±0.0083. The extrapolated efficiency from this curve at E_γ =5.7 MeV is 0.0932±0.0011, which agrees within 4% of the GEANT3.15 simulated value.

4.14 The Reduction of Total Cross Section

The total cross sections were calculated from the angular distribution of the differential cross sections. The differential cross section in the center of mass frame can be expanded into Legendre polynomials,

$$\frac{d\sigma}{d\Omega} = \frac{a_0}{4\pi}(1 + \sum_{L=1}^{\infty} a_L Q_L P_L(\cos\theta)), \qquad (4.40)$$

where a_0 and a_L are the fitted coefficients and Q_L is the finite geometry attenuation factor. By integrating Equation 4.40 over the solid angle $d\Omega = sin\theta\, d\theta\, d\phi$, the total cross section σ_{tot} can be obtained

$$\sigma_{tot} = \int \frac{d\sigma}{d\Omega}\sin\theta d\theta d\phi = \int \frac{a_0}{4\pi}(1 + \sum_{L=1}^{\infty} a_L Q_L P_L(\cos\theta))\sin\theta d\theta d\phi = a_0 \qquad (4.41)$$

Therefore, zero-order fitting coefficient a_0 equals the total cross section for the angular distribution at certain center of mass energy.

Q_L describes the correction factor associated with the effects of γ-rays hitting the Ge detector at an off-axis angle [Ros53]. When γ-rays hit the detector along the center axis of the detector, they have a maximum probability to be detected. When γ-rays enter the detector at a slanted angle, they become relatively less likely to be detected as they encounter less of an active volume of the Ge crystal. Additionally because of the finite size of the detector, even if all the γ-rays have the same off-axis angle, the detecting probability would be different for those hitting the detector at different distance with respect to the center axis. Therefore, Q_L coefficients originate from the finite or asymmetric shape of the detector geometry. It can be seen that all Q_L would be identically equal to one if the detector is completely symmetric with respect to the incoming angles of the γ rays, e.g. if the detector is shaped like an element of sphere surface.

In the present work, Q_L was calculated using the Monte Carlo averaging method [Bru94]. The following expression was used to calculate Q_L.

$$Q_L = \frac{1}{N}\sum_{i=1}^{N} P_L(\cos\beta_i), \qquad (4.42)$$

where N is the total number of sampled γ-ray events, and β_i is the tracked angle of individual γ-ray.

Since the detector was placed relatively far from the target, the Q_L should be all close to one. For example, the calculated first order Q_1 =0.996 (L=1 in Equation 4.42) and second order Q_2 =0.988 (L=2 in Equation 4.42). The expansion in Equation 4.42 was carried out only to the second power and the symmetry around the 90° was assumed, which means all the odd terms in Equation 4.40 would vanish. The assumption is in

accordance with the fact that the γ rays predominantly follow the $\sin^2\theta$ distribution as expected for E1 transitions. The systematic error arising from the presence of the other multipolarities is small.

The S-factor at each measured energy could be derived from its definition of Equation 3.2. The energy dependence of the S-factor for proton-deuteron capture reactions could be described with a straight line [Gri63].

$$S(E) = S(0) + E \times \frac{dS}{dE} \qquad (4.43)$$

where slope dS/dE is a constant which is usually evaluated at zero energy from the first order Maclaurin expansion of S(E).

A linear regression method is used to fit the experimental S-factors to the linear form of Equation 4.43. This method is a little different from the previous spectrum deconvolution method using χ^2 minimization technique. The essential point here is fitting a straight line using Equation 4.43 to a set of S(E) data points with errors on both y-coordinates value S *and* x-coordinates value E. The principle for performing such regression analysis is to minimize the distance of any point on the straight line in the form of Equation 4.43 to the error ellipses of all the data points [Lyo86]. The error ellipse for a data point (S_i , E_i) is given as

$$F(S,E) = \frac{(S - S_i)^2}{\delta S_i^2} + \frac{(E - E_i)^2}{\delta E_i^2} \qquad (4.44)$$

where δS_i and δE_i are the statistical errors on S_i and E_i respectively.

Therefore the final function *f* for minimization can be reduced to [Lyo86]

$$f = \frac{\sum_i (S_i - S(0) - (dS/dE)E)^2}{(dS/dE)^2 \delta E_i^2 + S_i^2} \qquad (4.45)$$

where the sum over i is for all the data point (S_i, E_i).

One important result from the minimization of Equation 4.45 is that the final regression line has the form of

$$S(E) = \overline{S}(E_c) + (E - \overline{E}_c) \times \frac{dS}{dE} \qquad (4.46)$$

where $\overline{S}(E_c)$ is the averaged S-factor from all measured data points and $\overline{E}_c$ is the averaged center of mass energy at all data points.

Therefore, the final regression line from Equation 4.46 passes through the center of the mass point of all the data points. Since this point is the averaged value of all the data points, the random uncertainties is expected to be minimum both in x-coordinate and y-coordinate directions.

4.15 Error Analysis for Cross Sections

In the analysis of cross section data, the systematic and statistical errors were estimated separately. The total percentage error was calculated by combining the quadratures of all the percentage errors from its components as shown in Equation 3.1.

The statistical percentage error δ_γ in the yield of γ-rays is given by

$$\delta_\gamma = \frac{\sqrt{N_\gamma + N_b}}{N_\gamma - N_b} \qquad (4.47)$$

in which N_γ is detected γ ray counts and N_b is the background.

If the background is relatively low (i.e. $N_\gamma - N_b >> 0$) as in our case (See Figure 4.1), Equation 4.39 could be applied. The typical error δ_γ in a spectrum as shown in Figure 4.1 is 1%-2.7%.

The statistical errors from all the Monte Carlo sampling for calculating geometric efficiencies are given by $\frac{1}{\sqrt{\text{Sample Size}}}$, which is typically less than 0.05%. The interpolated statistical error from the efficiency calibration curve was calculated using $\Delta\chi^2=1$ method. The assigned error as mentioned in preceding sections is 1.2%.

The systematic error from Beam Current Integration arising from the integrator was assigned to be 1% according to operation manual. The target thickness calculated from the extracted TRIM92 curve was assigned a 5% error [Zie85]. The finite target size measured from the beam spot and the target to detector distance which resulted in the final value of the geometric efficiency was estimated to be 2%. The assumption to constrain the angular distribution of the differential cross sections to be symmetric around 90^o was assigned a systematic error of 4% from the previous measured results [Gri63]. The assumption of uniformity in the profile distribution of the beam and other effects were assigned an error of 1%. The combined systematic error was taken to be arising from adding all these errors in quadrature in 6.8% overall.

V. Final Results and Comparison With Previous Measurements

5.0 Overview

In this chapter, experimental results including the polarization observables and cross sections for the $^2H(\vec{p},\gamma)^3He$ and $^1H(\vec{d},\gamma)^3He$ reactions will be presented. This chapter is divided into two parts. In the first one, the vector analyzing powers of $A_y(E_{c.m.},\theta)$ or $iT_{11}(E_{cm}, \theta)$ are shown, which are followed by the results for the tensor analyzing powers $T_{20}(E_{c.m.},\theta)$ and $T_{22}(E_{c.m.}, \theta)$. In the second part of this chapter, The final results for the angular distributions of the differential cross sections and total cross sections are given. The extracted astrophysical S-factor based on the energy dependence of the total cross section will be discussed. The results will be compared with the previous measurements (see references [Gri63], [Bai70], and [Sch95]). Since full angular distributions of the analyzing powers at energies below 1 MeV are measured here for the first time in such an energy range, analysis based on the Legendre polynomials expansion will also be presented.

5.1 Legendre Polynomial Analysis

The goal for performing Legendre polynomial analysis to the data is to extract more information about the various multipole contributions to the proton-deuteron capture processes. The formulae used here followed the definitions given by Seyler [Sey79].

It has been proved that the following expansions can be applied to the polarized cross sections and analyzing powers:

$$\sigma(\theta) = A_0(1 + \sum_1 a_1 P_1(\cos\theta)) \qquad (5.1)$$

$$\sigma(\theta)A_y(\theta) = A_0 \sum_1 b_1 P_1^1(\cos\theta) \qquad (5.2)$$

$$\sigma(\theta)iT_{11}(\theta) = \frac{A_0}{\sqrt{3}} \sum_1 b_1' P_1^1(\cos\theta) \qquad (5.3)$$

$$\sigma(\theta)T_{20}(\theta) = A_0 \sum_1 c_1 P_1(\cos\theta) \qquad (5.4)$$

$$\sigma(\theta)T_{22}(\theta) = \frac{A_0}{2} \sum_1 e_1 P_1^2(\cos\theta) \qquad (5.5)$$

In these expressions, we have chosen a convention that iT_{11} denotes the vector analyzing power for $^1H(\vec{d},\gamma)^3He$ reaction, and A_y denotes the vector analyzing power for $^2H(\vec{p},\gamma)^3He$ reaction. Since one of them is a rank-2 tensor, the other one is a vector, this notation is appropriate. The P_l^m coefficients in the equations are associated Legendre polynomials and $\sigma(\theta)$ is the unpolarized cross section. The mutipole combinations which contribute to each Legendre expansion coefficients is summarized in the Table 5.1.

The cross section $\sigma(\theta)$ for the proton-deuteron capture reaction can be written as [Wol62],

$$\sigma(\theta) = \sigma_0(a/b + \sin^2\theta(1 + \beta\cos\theta)) \qquad (5.6)$$

where a/b represents M1/E1 strength ratio, and β represents E1-E2 interference. The measurements performed by Griffith [Gri62, Gri63] showed that β vanishes for the reaction energy $E_{c.m.}$ below 330 keV. Therefore, all the angular distributions for $\sigma(\theta)$ can

be simply fitted by $A+B\sin^2(\theta)$, which was the formula used by Griffiths et al. throughout their analysis. This result is consistent with the theoretical work of Donnely[Don67] who showed that for proton-deuteron capture only M1 and E1 transition contribute significantly to the cross sections at low energies. Based on these findings, the present analysis for cross sections includes only up to second order polynomial in Equation 5.1. All the fits to the analyzing powers are expanded up to $L_{max}=4$ in Equation 5.2-5.5. In the fits, all the Legendre polynomials were also weighted by their finite geometric correction coefficients Q_L as calculated from Equation 4.42.

Order of the expansion l	Contributing matrix elements
0	$\|E1\|^2+\|M1\|^2+\|E2\|^2$
1	E1•M1+E1•E2
2	E1•E1+M1•M1+E2•E2+M1•E2
3	E1•E2
4	E2•E2

Table 5.1 Multipole contributions to each Legendre expansion coefficients.

5.2 Vector Analyzing Powers

In this section, the measured energy dependence of vector analyzing powers for $^2H(p,\gamma)\ ^3He$ and $^1H(d,\gamma)^3He$ reactions are first shown. Then results are also presented for the angular distributions and their Legendre polynomials best fits at center of mass energy of 50 keV . This energy was chosen in order to compare with the available theoretical model calculations discussed in the next chapter. Similar analysis have been conducted for

several reaction energies and all the expansion coefficients and their associated errors are given.

The measured energy dependence of A_y for $^2H(\vec{p},\gamma)^3He$ for $E_{c.m.}$=70-210 keV is shown in Figure 5.1. The energy dependence of iT_{11} for $^1H(\vec{d},\gamma)^3He$ reaction from center of mass energy of 50 keV to 110 keV is shown in Figure 5.2.

It can be seen from our measurements that the vector analyzing powers for both $^2H(\vec{p},\gamma)^3He$ and $^1H(\vec{d},\gamma)^3He$ show a very weak energy dependence. Some structures in the curves shown are believed to be caused by the statistical fluctuation in the γ-ray spectra, which lies within the overall statistical uncertainties. Vector analyzing power A_y is positive (close to 0.04) and is almost independent of the angle. The iT_{11} is negative and also shows more angular dependence.

As described in Chapter 4, the energy dependence of all the presented analyzing powers was first extracted as a continous function of the center of the mass energy. The error band enclosing this functional dependence was defined as encompassing one-sigma (68.3%) confidence level. In all the following figures showing the energy dependence of the analyzing powers, it should be kept in mind that the data points on the fitted curve are equidistant but selected subjectively and the error bar on each data point is the *extrapolated* statistical error, or simply the positions marking the calculated error band.

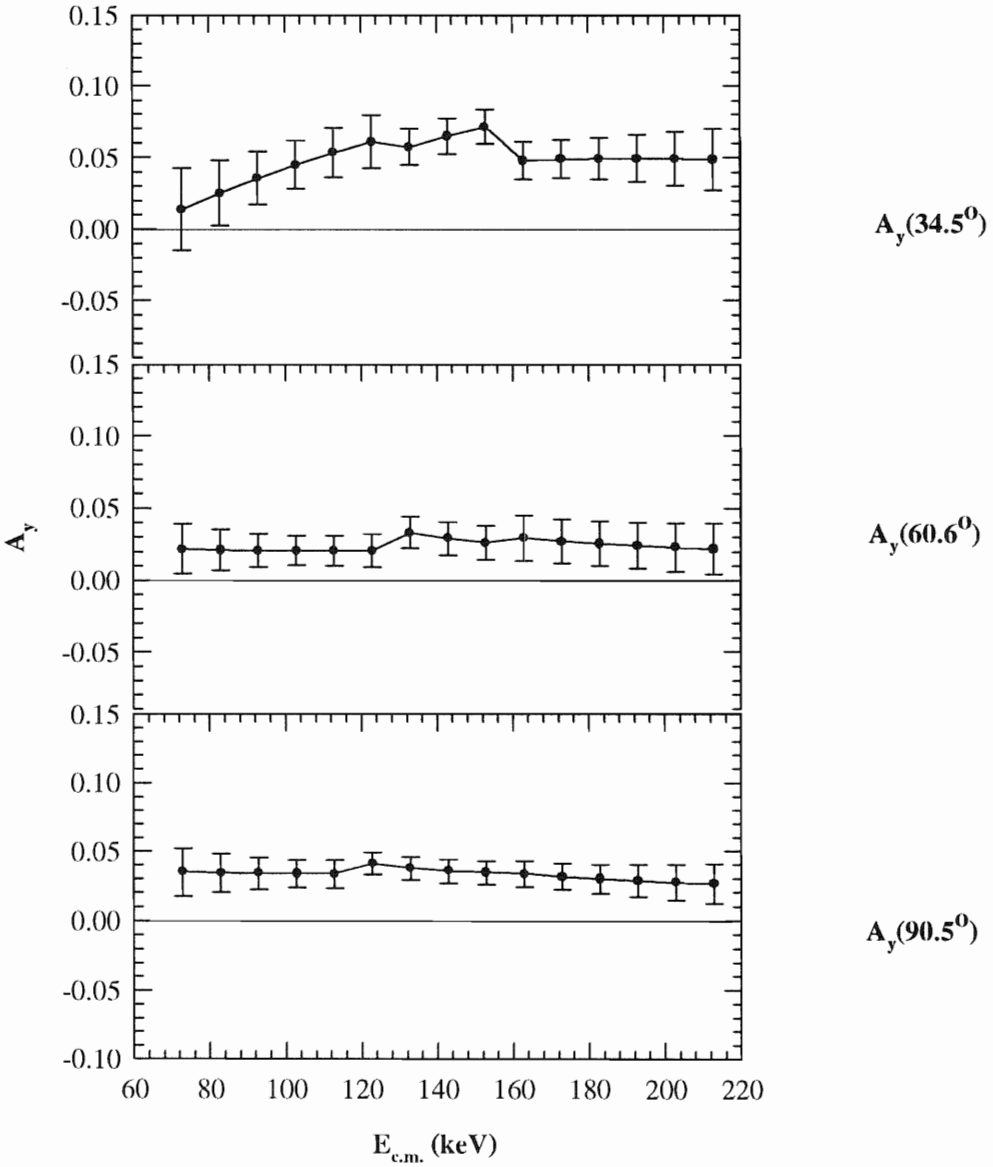

Figure 5.1 The measured energy dependence of A_y for $^2H(\vec{p},\gamma)^3He$ reactions.

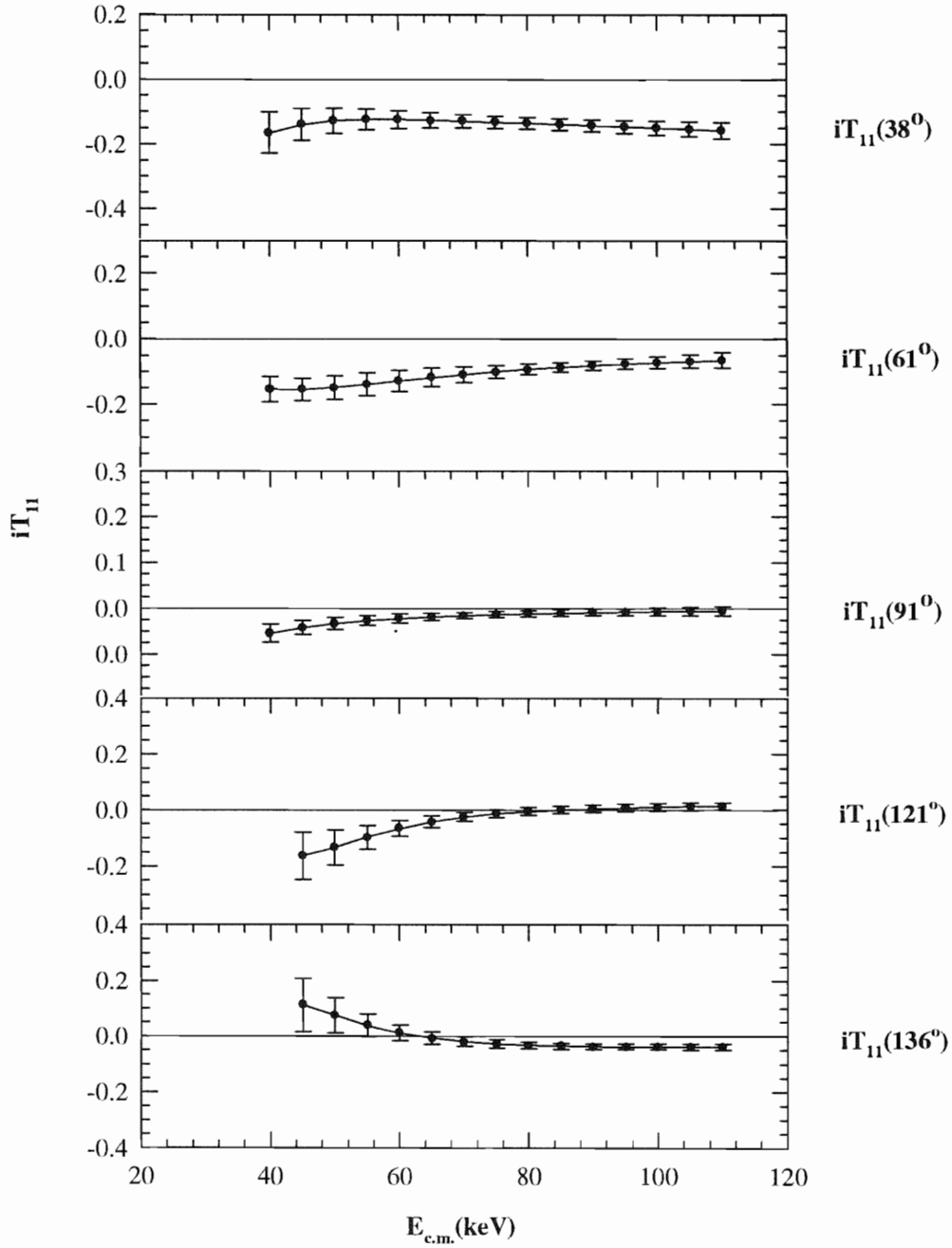

Figure 5.2 The energy dependence of iT_{11} for $^1H(\vec{d},\gamma)^3He$ reactions.

The angular distributions for both A_y and iT_{11} are fitted with the first order associated Legendre polynomials as described in Equation 5.12. Since the Legendre functional basis is in the linear form, the error associated with each expansion coefficients can be calculated using the prescription described in Chapter 4. The χ^2 definition for the minimization process used in this analysis can be written as

$$\chi^2 = \sum \frac{(f(\vec{p}) - y_i)^2}{(\Delta y_i)^2} \qquad (5.7)$$

where f are the associated Legendre expansions listed in Equations 5.1-5.5, $\vec{p}$ denotes the vector for expansion coefficients, y_i's are the measured observables, which here are A_y, iT_{11}, T_{20} and T_{22} and Δy_i's are their statistical errors. The extrapolated error on each expansion coefficient could be calculated by solving Equation 4.30 using the same minimization algorithms as described in Chapter 4. It should be noted that in the expansions of A_y and iT_{11}, b_0 and b'_0 should be identically zero since the zeroth order of P^l_m vanishes when l=1. For a similar reason, both e_0 and e_1 in Equation 5.5 also should vanish.

In this section, Legendre polynomials' best fit coefficients will be presented for both A_y of $^2H(\vec{p},\gamma)^3He$ and iT_{11} of $^1H(\vec{d},\gamma)^3He$ at four sampled center of mass energies.

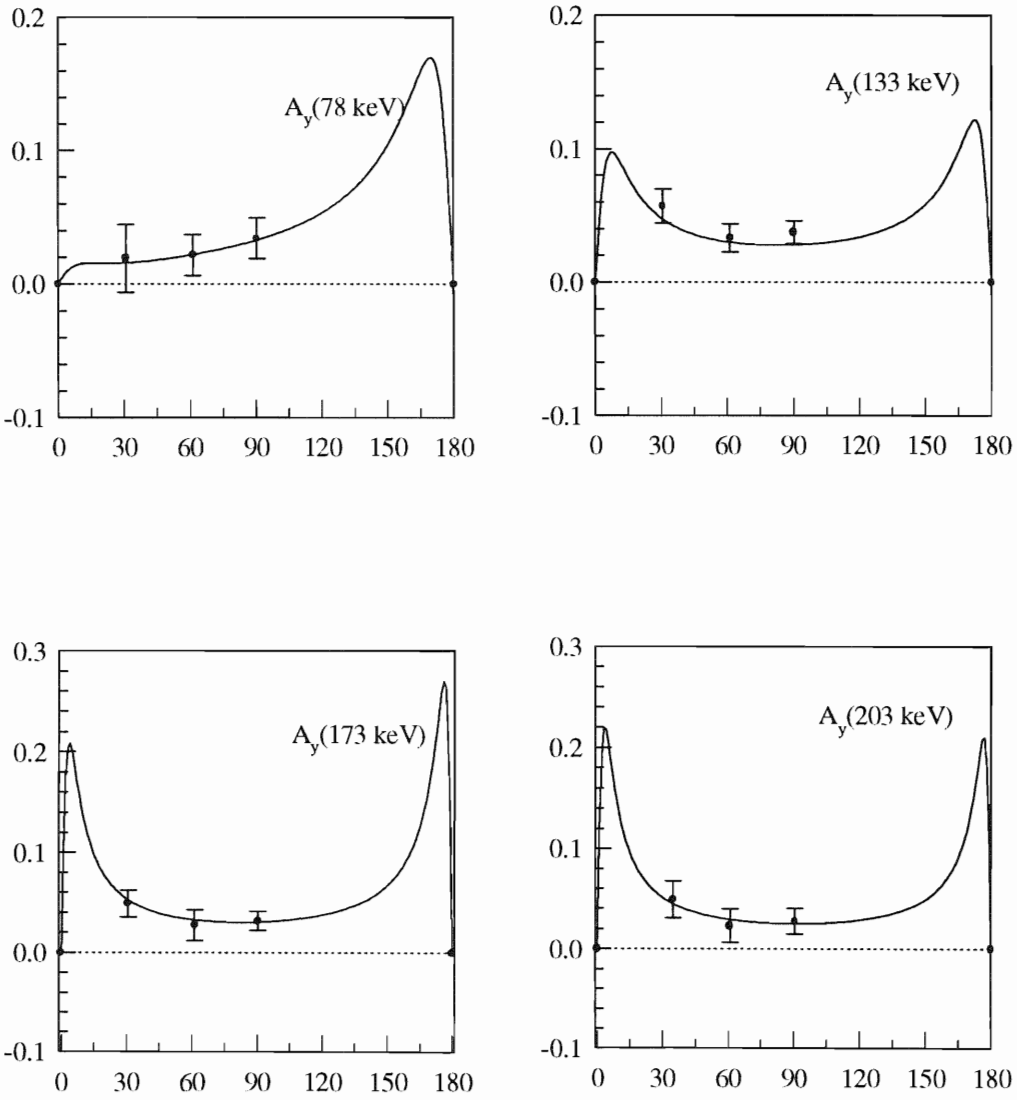

Figure 5.3 The best Legendre polynomials' fit of A_y for $^2H(\vec{p},\gamma)^3He$ at four sampled energies. The table of the all the fitting coefficients is given in Table 5.2.

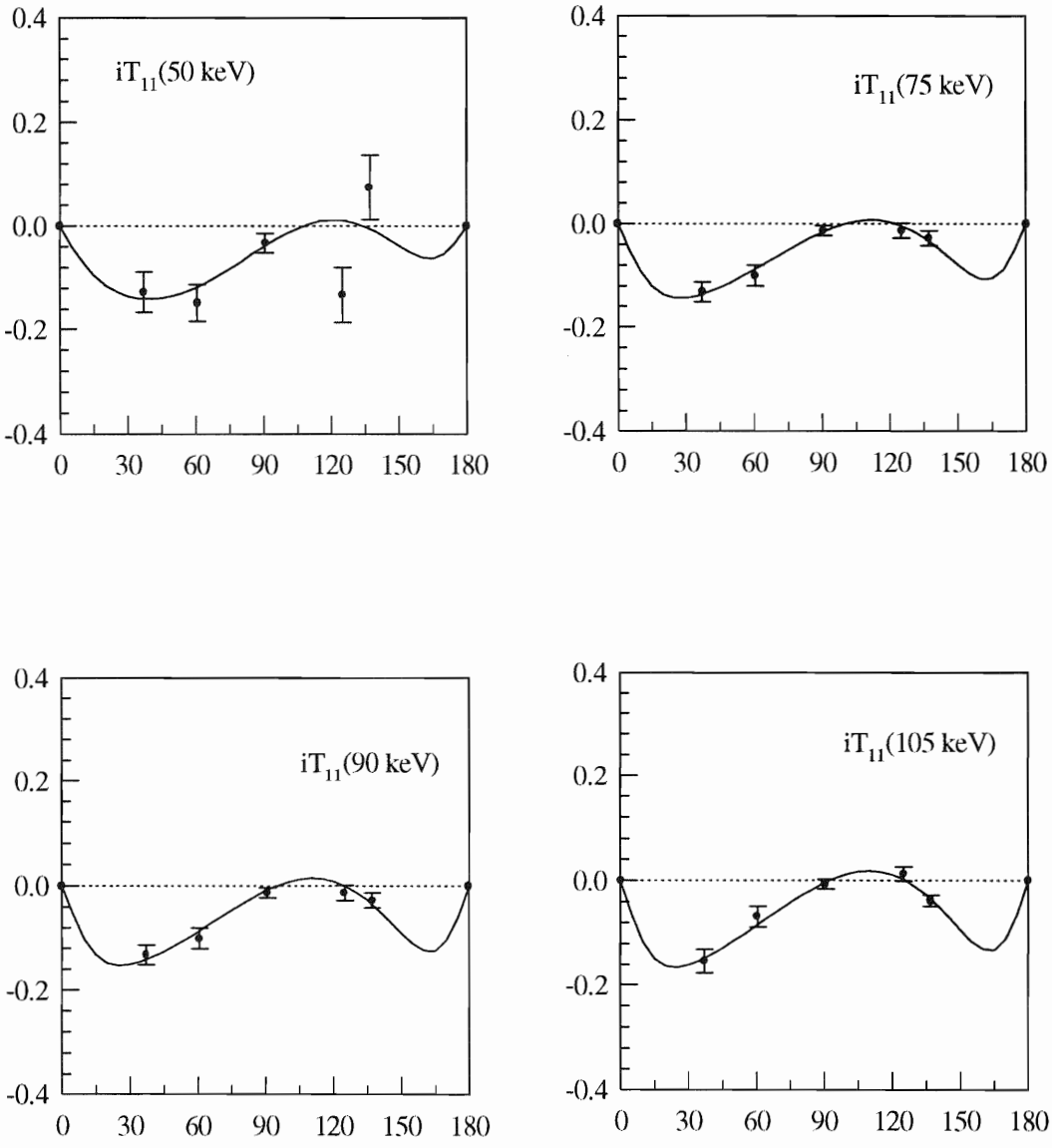

Figure 5.4 The best Legendre polynomial fits of iT_{11} for $^2H(\vec{d},\gamma)^3He$ at four energies. The fitting coefficients are given in Table 5.3.

$E_{c.m.}$(keV)	78	133	173	203
a_2	-0.965 ± 0.068	-0.989 ± 0.045	-1.008 ± 0.073	-1.012 ± 0.102
b_1	-0.049± 0.021	-0.042 ± 0.012	-0.046± 0.014	-0.038 ± 0.018
b_2	0.014± 0.012	-0.0016± 0.0069	-0.0020± 0.0075	-0.0003± 0.010
χ^2/nf	0.15	2.3	0.15	0.20

Table 5.2 Legendre coefficients of A_y for $^2H(\vec{p},\gamma)^3He$ at four reaction energies, where fore-aft symmetry is assumed for unpolarized cross sections, i.e., a_1=0. By definition a_0=1.

$E_{c.m.}$(keV)	50	75	90	105
a_2	-0.953± 0.095	-0.964± 0.071	-0.971± 0.058	-0.977± 0.048
b_1'	0.112 ± 0.029	0.081± 0.012	0.072± 0.012	0.064± 0.015
b_2'	0.073± 0.028	0.049± 0.010	0.051± 0.008	0.052± 0.010
b_3'	0.0055± 0.017	0.024± 0.006	0.031± 0.006	0.035± 0.007
b_4'	-0.026± 0.026	-0.019± 0.011	-0.021± 0.009	-0.020± 0.011
χ^2/nf	8.1	1.7	0.4	1.0

Table 5.3 Legendre coefficients of iT_{11} for $^1H(\vec{d},\gamma)^3He$ at four reaction energies.

As can be seen from Table 5.2, b_2 coefficients are consistently zero within statistical uncertainty and the interference among M1, E1, E2 yields negative b_1. On the other hand, Table 5.3 shows that b_3' and b_4' terms are zero within statistical uncertainty. This confirmed that E2 contribution is negligibly small at these low reaction energies. The interference among M1 and E1 yield an overall positive values for b_1' and b_2' coefficients.

5.3 Tensor Analyzing Powers

The experimental tensor analyzing power A_{yy} and A_{zz} for $^1H(\vec{d},\gamma)^3He$ reaction were measured at $\theta_{c.m.}$= 0°, 38.2°, 60.6°, 90.7°, 120.6°, and 137.1° respectively. Due to the relationship between A_{zz} and A_{yy} at 0° from Equation 3.25, only A_{zz} was measured at 0°.

The conversion formula between the Cartesian and the spherical analyzing powers are given as the following,

$$\begin{cases} iT_{11} = \dfrac{\sqrt{3}}{2} A_y \\ T_{20} = \dfrac{1}{\sqrt{2}} A_{zz} \\ T_{22} = -\dfrac{1}{\sqrt{3}} A_{yy} - \dfrac{1}{2\sqrt{3}} A_{zz} = \dfrac{1}{2\sqrt{3}} (A_{xx} - A_{yy}) \end{cases} \tag{5.8}$$

It can be seen that the error propagation for A_y and A_{zz} conversions are straightforward. The error for (A_{xx}-A_{yy}) is deduced in our analysis by the following:

$$\Delta(A_{xx} - A_{yy})^2 = \Delta(A_{zz} + 2A_{yy})^2 = (\Delta A_{zz})^2 + 4(\Delta A_{yy})^2 \tag{5.9}$$

In this section, the energy dependence for the measured T_{20} and T_{22} are presented first. Next the angular distributions for T_{20} and T_{22} at $E_{c.m.}$= 50 keV together with their Legendre polynomial fits are shown. As before, the error bar on each data point correspond to a statistical error with one-sigma confidence level (C.L.)(i.e. 68.26%), which we have discussed in Chapter 4. The final results for Legendre coefficients are tabulated for four characteristic reaction energies.

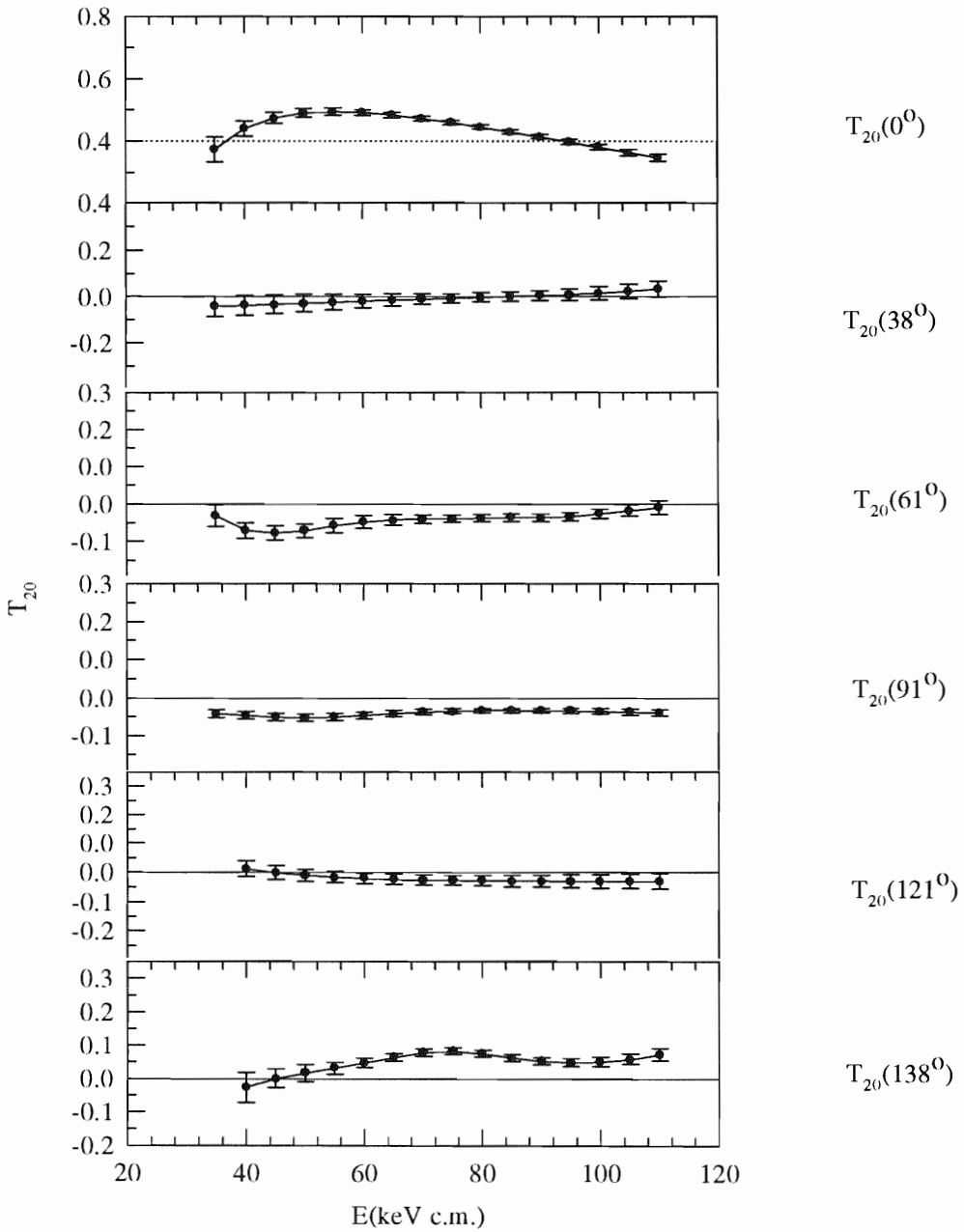

Figure 5.5 Measured energy dependence of T_{20} for $^1H(\vec{d},\gamma)^3He$ reaction.

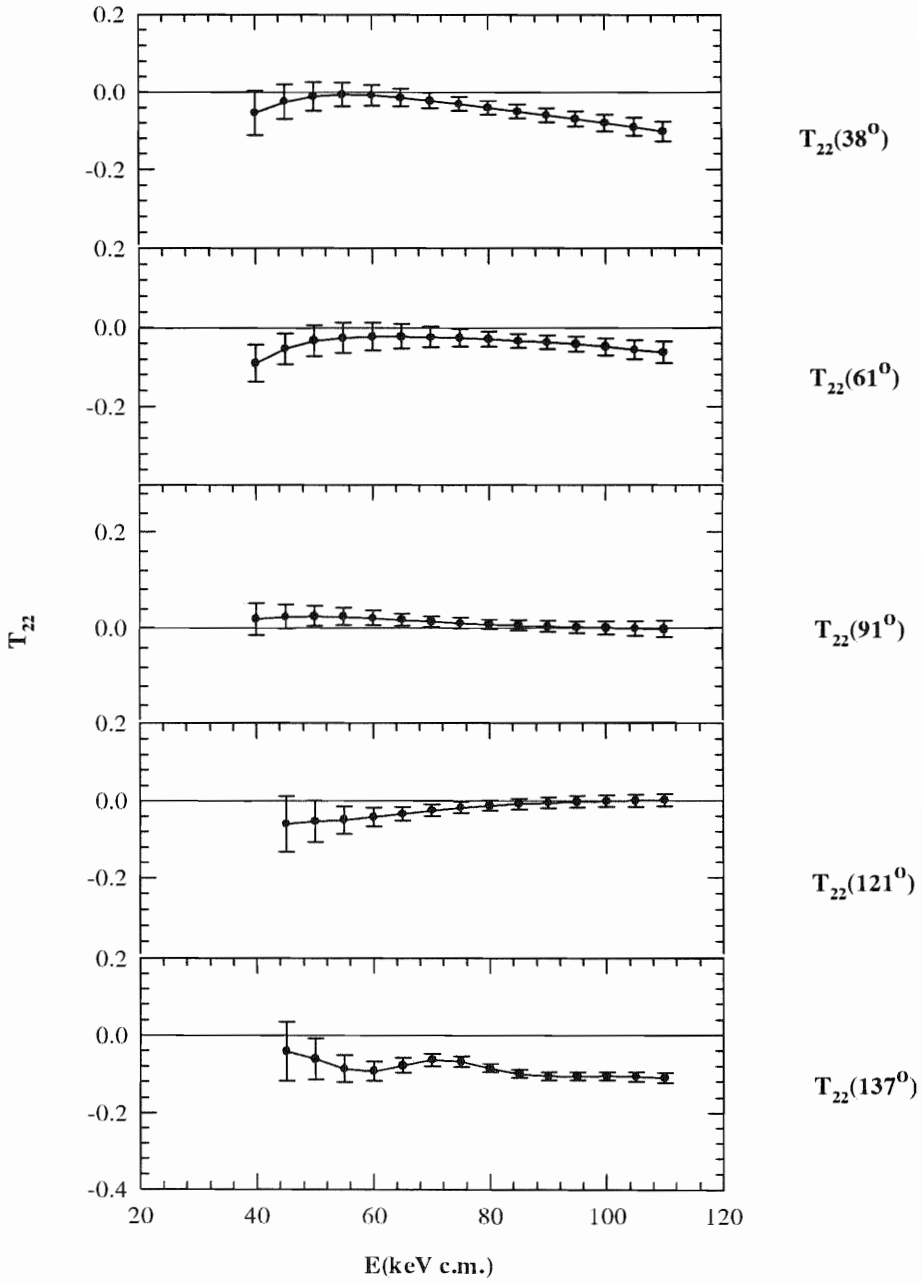

Figure 5.6 Measured energy dependence of T_{22} for $^1H(\vec{d},\gamma)^3He$ reaction.

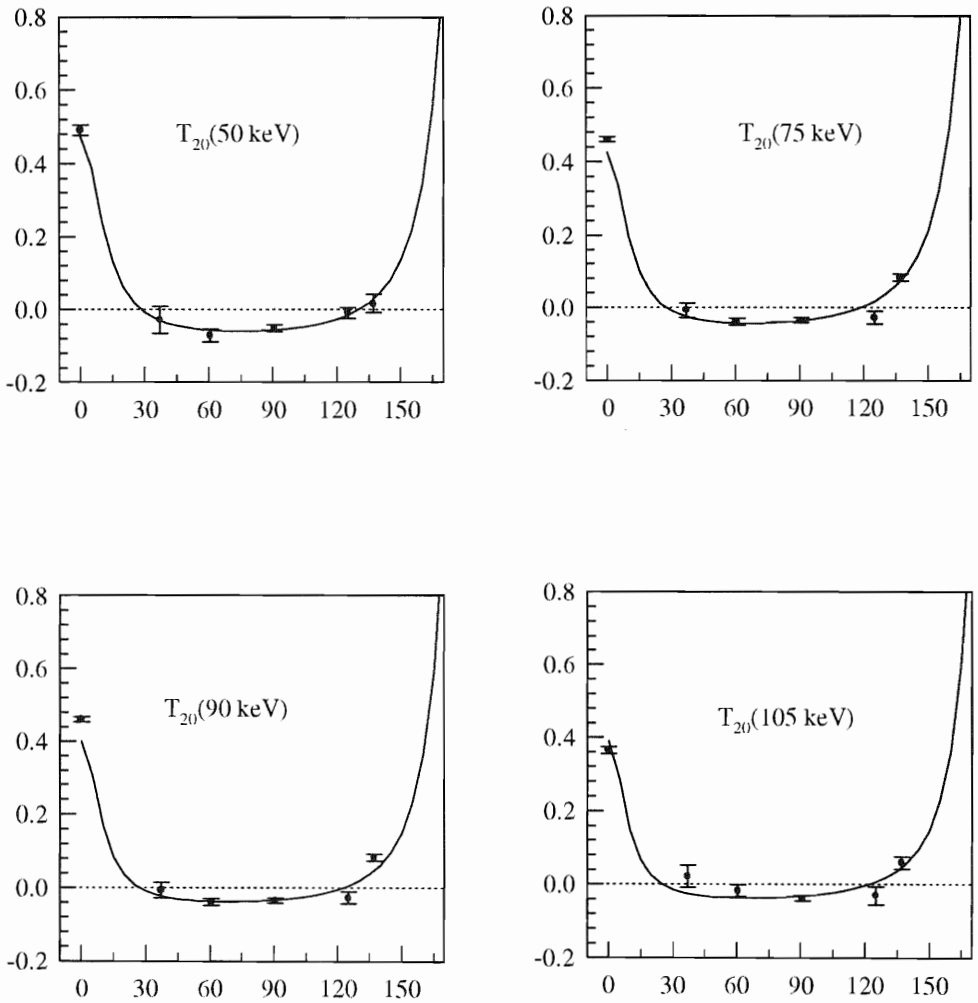

Figure 5.7 The best Legendre polynomials' fit of T_{20} for $^1H(\vec{d},\gamma)^3He$ at four reaction energies.

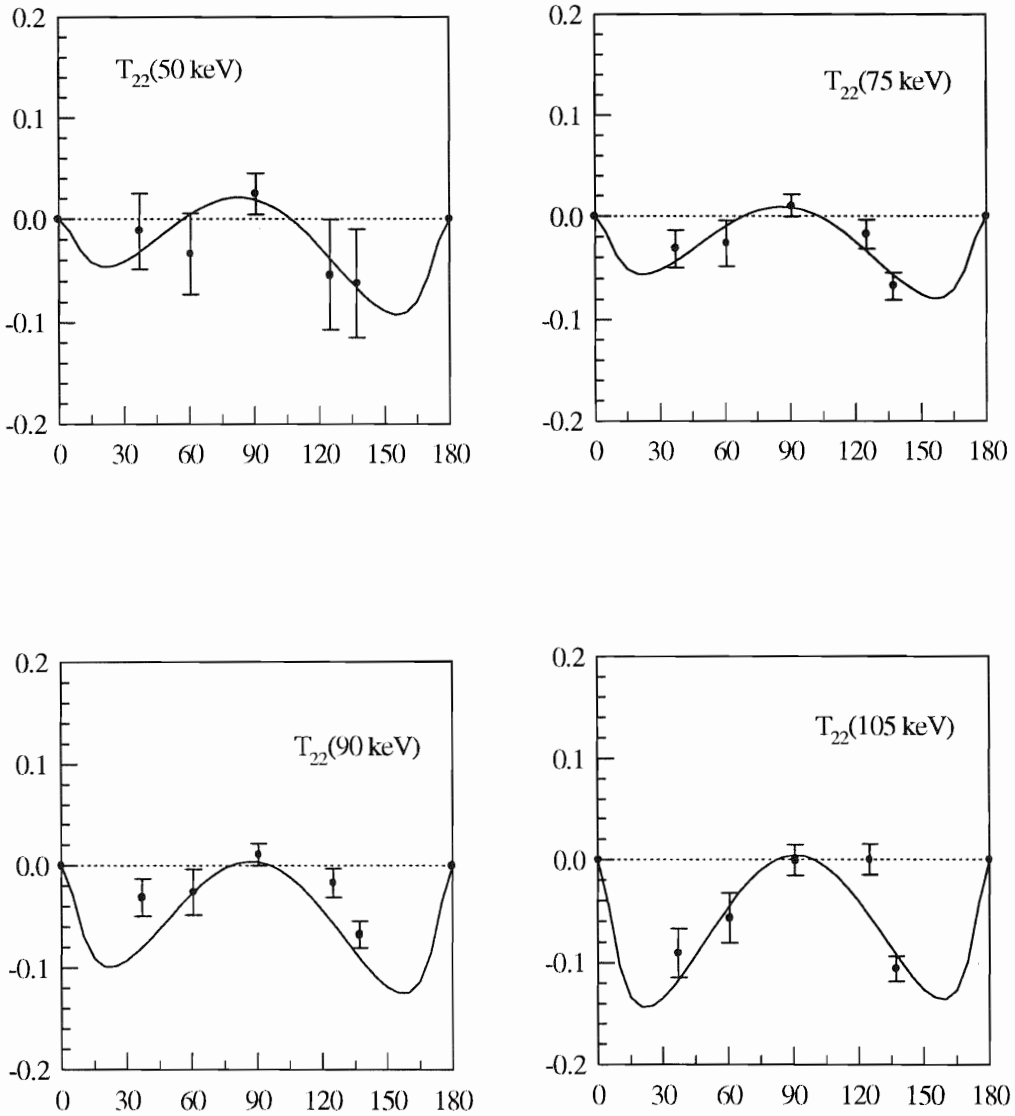

Figure 5.8 The best Legendre polynomial's fit of T_{22} for $^1H(\vec{d},\gamma)^3He$ at four reaction energies.

E (keV c.m.)	50	75	90	105
a_2	-0.953± 0.095	-0.964± 0.071	-0.971± 0.058	-0.977± 0.048
c_0	-0.034± 0.007	-0.011± 0.005	-0.015± 0.003	-0.014± 0.005
c_1	-0.034± 0.012	-0.052± 0.006	-0.037± 0.004	-0.037± 0.005
c_2	0.099± 0.013	0.085± 0.008	0.070± 0.004	0.066± 0.005
χ^2/nf	0.4	2.9	1.6	2.5

Table 5.4 Legendre coefficients of T_{20} for $^1H(\vec{d},\gamma)^3He$ at four reaction energies.

E (keV c.m.)	50	75	90	105
a_2	-0.953± 0.095	-0.964± 0.071	-0.971± 0.058	-0.977± 0.048
e_2	0.002± 0.023	-0.006± 0.011	-0.019± 0.012	-0.023± 0.015
e_3	0.0062± 0.0072	0.003± 0.003	0.0033± 0.002	-0.001± 0.003
e_4	-0.007± 0.004	-0.006± 0.002	-0.009± 0.002	-0.011± 0.002
χ^2/nf	0.7	1.5	8.3	7.4

Table 5.5 Legendre coefficients of T_{22} for $^1H(\vec{d},\gamma)^3He$ at four reaction energies. Note that e_0 and e_1 are equal to zero by definition.

As it can see from angular distribution of T_{20} in Figure 5.7, it is consistently small negative at 90° and large (close to 0.5) positive at extreme forward and backward angles. The E1 transition is responsible for the behavior at 90°, while the M1 is responsible for the extreme forward and backward angles, especially at 0°. From Table 5.4 of the Legendre

coefficients, the inteference between E1 and M1, E2 mutipoles all contribute significantly to the T_{20} data. For T_{22} analyzing power, it is close to zero or slight positive at 90° and all its Legendre coefficients are small in Table 5.5.

5.4 Total Cross Section and S-factor

The measured differential cross section data in four energy bins center around 75, 108, 133, 175 keV are shown in Figure 5.9. The bin size was chosen to be 20 keV around the centroid energy.

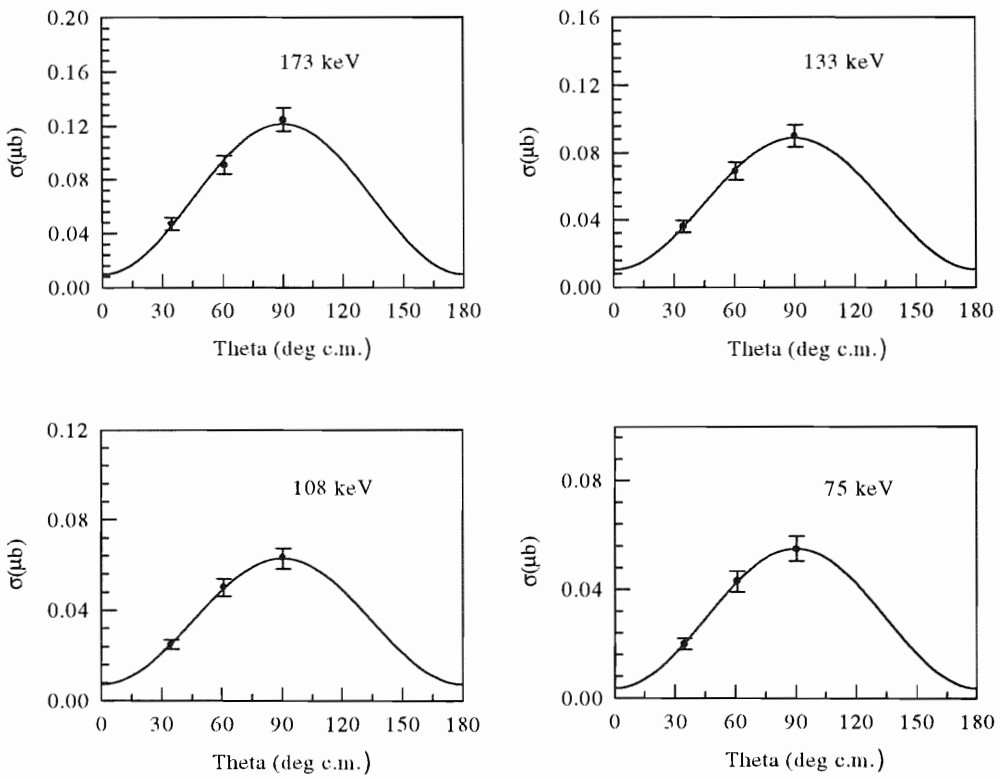

Figure 5.9 The angular distributions of the cross sections at four binned energies.

The average energy in each energy bin is calculated by using Equation 5.10, which takes the beam stopping effects into consideration [Fle92].

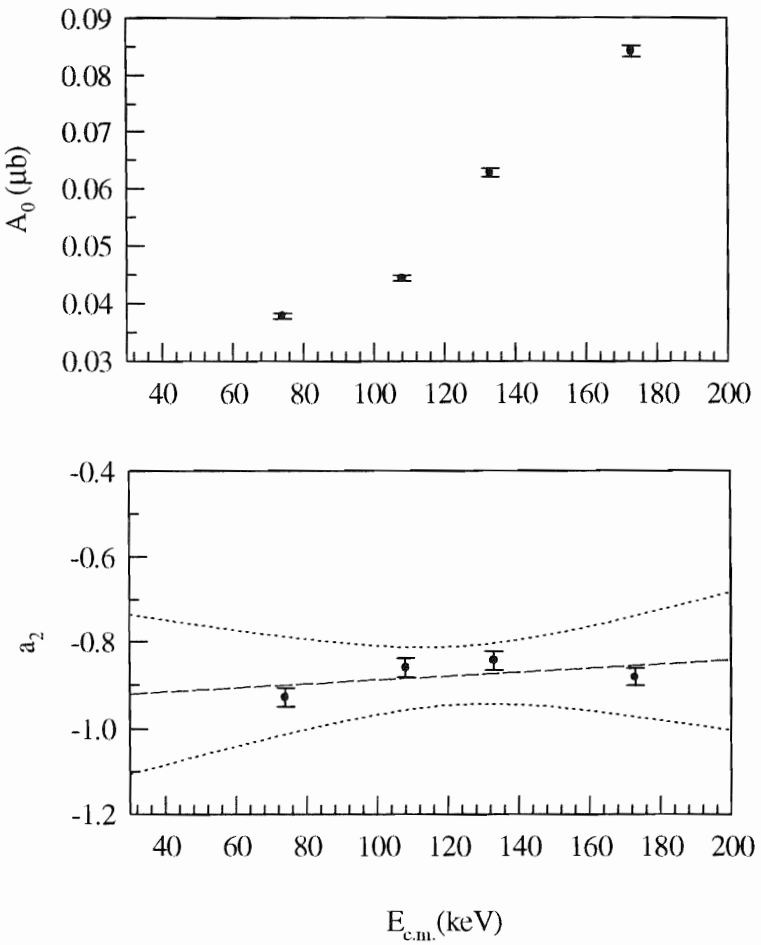

Figure 5.10 Energy dependence of the Legendre coefficients for cross section data. The solid line in the second plot is the linear regression result enclosed by two dashed lines corresponding to 95% confidence level.

$$\langle E \rangle = \frac{\sum_i E_i \sigma(E_i)}{\sum_i \sigma(E_i)} \qquad (5.10)$$

where $\sigma(E_i)$ is the cross section in the ith energy channel.

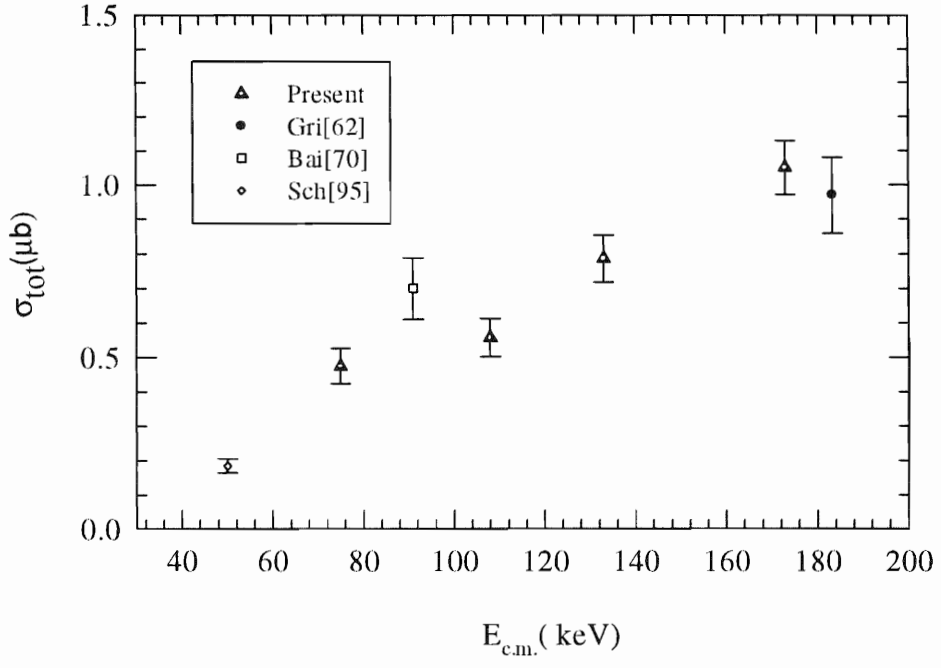

Figure 5.11 The extracted total cross sections in comparison with previous results.

The total cross sections at each energy can be extracted from the zeroth order coefficients of the Legendre polynomial fits of the angular distributions of the cross sections. The for-aft symmetry around 90° is assumed in the above Legendre polynomial fits to the angular distribution of the cross section. The energy dependence of the A_0 and a_2 coefficients are given as following in Figure 5.10.

The total cross section is equal to $4\pi A_0$ from Equation 4.34 as described in the last chapter. The final results are plotted together with the previous measurements[Gri63] in Figure 5.11.

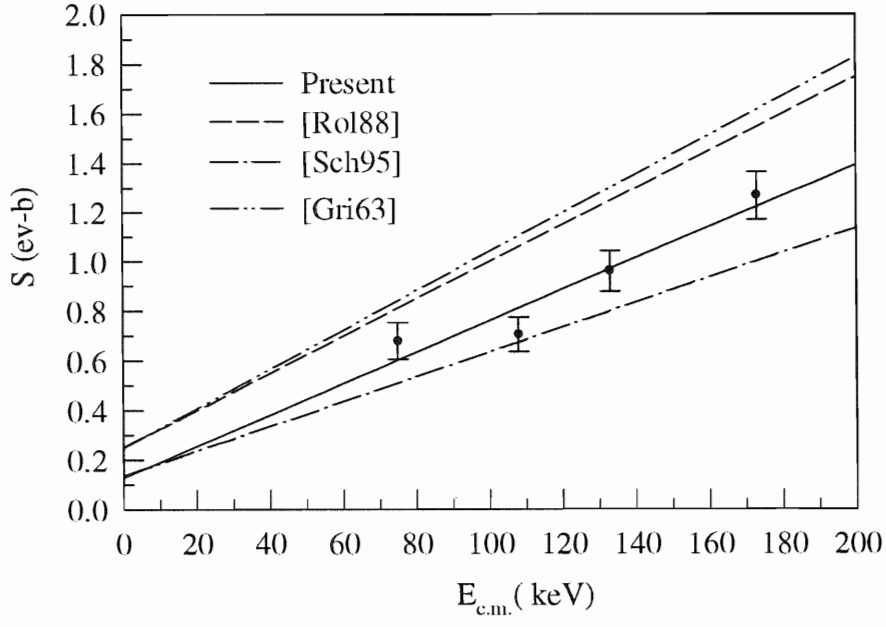

Figure 5.12 The comparison among the present extracted S-factors and previous measurements [Rol88, Sch95].

As it can been from Figure 5.11, our present measurements agree very well within statistical errors with the previous measurements at the same energy region [Gri62], [Bai70]. Further comparison can be done for the astrophysical S-factors.

The astrophysical S-factor can be extracted from the total cross section data from its definition of Equation 3.1. The results are plotted in Figure 5.12.

The solid line in Figure 5.12 is the linear regression result from the four energy bins. The dash line corresponds to values currently used in the standard astrophysical model [Rol88]. The double-dotted dashed line corresponds to the measurements of Griffith [Gri63]. The recent measurement by Schmidt *et al.* [Sch95] is given by the dot-dash line. It can be seen that in the measured energy range, none of these curves could describe our present data reasonably though our cross section data agree reasonably well with the previous data [Gri62][Bai70].

	Griffith [Gri63]	Rolfs [Rol88]	Schmid [Sch95]	Present Work
S(0) (ev b)	0.25±0.04	0.25 (theory)	0.136±0.013	0.130±0.074
dS/dE (ev b/keV)	0.0079 (cal.)	0.075 (theory)	0.0050±0.0004	0.0062±0.00056

Table 5.6 Comparisons among all extracted S(0) and dS/dE values.

However, the linear regression fit gives an intercept of S(0)=0.130± 0.074, which agrees very well with the recently extracted value by Schmid *et al.* [Sch95]. The intercepts S(0) values and slopes dS/dE values for each of the curve are listed in the following Table 5.6. It is evident from Figure 5.12 and Table 5.6 that the results from the previous measurements are quite different at energy range below 40 keV. This leads to the conclusion that the presently accepted value of S(0) could be overestimated by as

much as 45%. This finding could have important consequences for the stellar evolution calculations.

VI. Theoretical Analysis

6.1 Introduction

In this chapter, we will explore two theoretical models for calculating the polarization observables in proton-deuteron capture reactions. The formalisms which will be presented are the Refined Resonating Group Model (RRGM) and the recently developed full three-body calculation, namely, Correlated Hyperspherical Harmonics expansion (CHH). The focus for the RRGM discussion will be concentrated on the inclusion of the meson-exchange-current effects. For variational techniques, full three body mechanism including the Coulomb treatment will be discussed in more detail. The final calculated results from both models will be compared with the experimental data.

As it is known, electromagnetic transition in a capture reaction can be treated as a small perturbation to a system's total Hamiltonian. In the configuration space, the nonrelativistic interacting Hamiltonian for such a process takes the form of

$$H_{\text{int}} = -\frac{1}{c}\int J^{\nu}(\vec{r})A_{\nu}(\vec{r},\vec{k})d^3\vec{r} \qquad (6.1)$$

where J^{ν} is the covariant current density and A_{ν} is the electromagnetic field carried by the photon with the momentum $\hbar k$.

The electromagnetic transitions in the proton-deuteron capture reactions conserve both angular momentum and parity. Since the photon is a spin-1 boson, the parity for EL transitions is $(-1)^{L+1}$ and it is $(-1)^{L}$ for ML transitions. The ^{3}He ground state has a spin-

parity of $(1/2)^+$. Following the rules of angular momentum coupling, the leading transitions for S, P, D partial waves are shown in the following diagram.

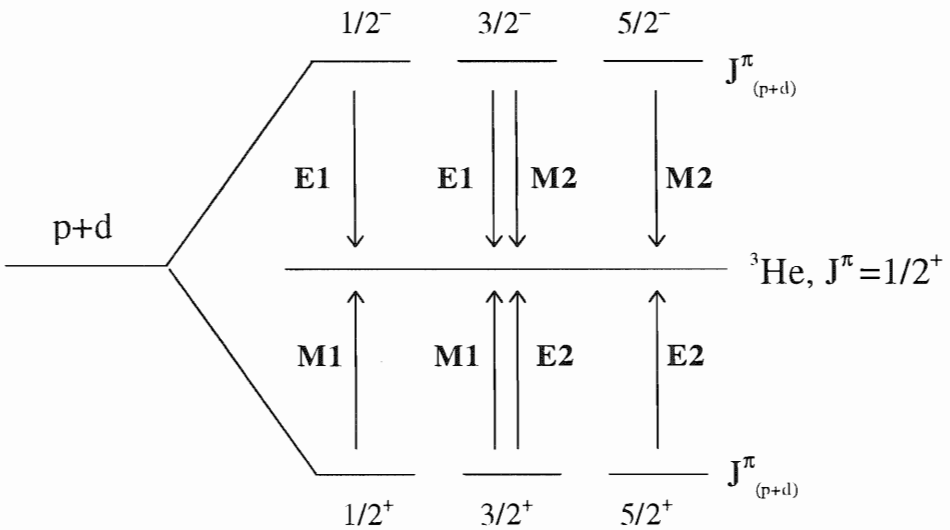

Figure 6.1. Diagram for allowed leading transitions and channel spins for proton-deuteron capture reactions.

It can be seen that E1 transition involves P-wave with channel spin $S=1/2^-$ or $3/2^-$, and M1 transition involves S-wave with channel spin of $1/2^+$.

The current density operator in Equation 6.1 must satisfy the continuity relation for particle number conservation, i.e.,

$$\partial_\nu J^\nu = 0 \qquad (6.2)$$

Eventually, the transition matrix element for proton-deuteron capture reaction can be calculated from $\langle {}^3\mathrm{He} \mid H_{int} \mid \mathrm{p+d} \rangle$, in which $|{}^3\mathrm{He}\rangle$ is ${}^3\mathrm{He}$ wave function and $|\,\mathrm{p+d}\,\rangle$ is

the proton-deuteron continuum state wave function. By expanding transition matrix element into the contributions from different multipoles, the total cross section is given by

$$\sigma \propto \frac{1}{E_{c.m.}} \sum_i c_i \left(|EL|^2 + |ML|^2 \right) \qquad (6.3)$$

where $|\mathrm{EL}|$ and $|\mathrm{ML}|$ represent the reduced matrix elements for the electric multipole and magnetic multipole contributions respectively.

If the angular distribution of the unpolarized differential cross section and analyzing powers are expanded into the associated Legendre polynomials by following the scheme of Seyler's papers [Sey79], [Sey84], then the Legendre expansion coefficients can be proven to be directly related to these reduced matrix elements. The formulae pertaining to these relationships can be found in the cited references [Mer86], [Web92]. Hence we can see that the calculation of the transition matrix elements is the key point for extracting all the physical observables for the capture reactions. This is the place where all the interesting physics comes from. It involves not only finding the eigenfunctions by solving the bound state Schrödinger equation, but also the careful treatment of the complete current operators such as inclusion of terms dependent on the meson-exchange currents. The following description of the RRGM and full three-body variational calculations will soundly illustrate this point.

6.2 Important Characteristics of RRGM

Resonating Group Model is a microscopic model, which means the bound state wave functions for the nuclear system are constructed explicitly from their substructures [Mer86]. The substructures are commonly called "clusters". For example, ^{3}He can be taken as a two-cluster structure. The two clusters can be formed by one proton-neutron pair (deuteron) plus the leftover proton, or it can be one "virtual" proton-proton pair interacting with the third neutron (see Figure 6.2 for illustration). Any nuclear bound state wave function should include all the combinations of the cluster configurations. In this sense, the inner structure of the deuteron inside ^{3}He is completely unfolded under RRGM in contrast to the direct models in which the deuteron is simply considered as a single spin-1 particle.

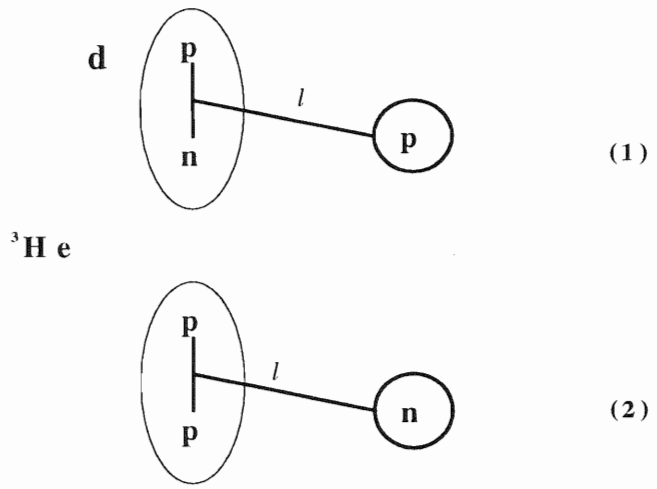

Figure 6.2 Illustration of cluster pairing for ^{3}He in the RRGM calculation.

The wave functions in the RRGM scheme are completely antisymmetrized so that Pauli Principle can be satisfied. This operation has adequately removed some unphysical

sources from the model itself. In addition, the center of the mass motion for different cluster fragments is treated correctly in the model. The resulting total Hamiltonian for the system is translational invariant.

The bound state wave function for ^{3}He in the present calculation is generated from the realistic two-body nucleon-nucleon potentials including Bonn potential and Stowe-Zahn potential. The final calculated binding energy for ^{3}He is 7.34 MeV as compared with the experimental value of 7.72 MeV [Sch88].

Finally, the Coulomb corrections are treated exactly in this model and one-pion-exchange diagrams are included effectively in the calculation of the total current density operator shown in Equation 6.1.

6.3 System Hamiltonian and Meson-exchange-current

The total Hamiltonian describing proton-deuteron capture reactions includes the sum of three components: a free nucleon-nucleon field, a free photon radiation field and a third term as shown in Equation 6.1 representing the interaction between these two fields. It can be written as:

$$H_{total} = H_{N-N} + H_{rad} + H_{Int} \qquad (6.4)$$

The $H_{N\text{-}N}$ term in Equation 6.3 is given in the translational invariant form as the following [Hof84],

$$H_{N-N} = \sum H_n + (\sum_{i\le j} V_{ij} - \frac{Z_1 Z_2 e^2}{R^2}) + (\sum_{i<j}^{3} \frac{(p_i - p_j)^2}{2m_i} + \frac{Z_1 Z_2 e^2}{R^2}) \qquad (6.5)$$

where H_n is the internal Hamiltonian for the cluster fragments, and Vij is the short-range, separable two-body nucleon-nucleon potential which includes the descriptions for central interaction, spin-orbital coupling, and tensor components involving spin and isospin interactions. Its general form is given by

$$\begin{aligned} V_{ij} &= V_c(r_{ij}) + V_s(r_{ij})(\vec{L}\cdot\vec{S}) + V_T(r_{ij})S(\vec{\sigma}_i,\vec{\sigma}_j) \\ &\quad + V_t(r_{ij})S'(\vec{\tau}_i,\vec{\tau}_j) \end{aligned} \qquad (6.6)$$

The last two terms in the second bracket of Equation 6.5 are the Coulomb and relative motion parts between two clusters inside ^{3}He. These two terms define the asymptotic form of the Hamiltonian if the two clusters are far from each other.

The photon radiation Hamiltonian can be written as the combination of creation and annihilation operators and then summed over all degrees of freedoms of photon polarization projections and total wave numbers, i.e.,

$$H_{rad} = \sum \hbar\omega\, b^+(\vec{k}) b(\vec{k}) . \qquad (6.7)$$

The field operator under Coulomb gauge is given by [Mer86]

$$A(\vec{k},\vec{r}) = \sum c_k (b\, e^{i\vec{k}\cdot\vec{r}} \mu^{(+)} + b^+ e^{-i\vec{k}\cdot\vec{r}} \mu^{(-)}) \qquad (6.8)$$

For the interactive Hamiltonian H_{int} as shown in Equation 6.1, the total current density includes the impulse term (point charge), the direct pion-exchange term and the Pion-Seagull term. Their Feynman diagrams are shown in Figure 6.3.

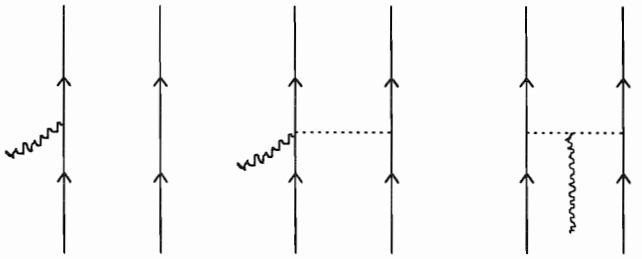

Figure 6.3 The leading meson exchange terms included in the RRGM calculations.

The terms involving heavy meson exchange current such as Δ and ρ have been neglected in the calculation.

The distinct property of the RRGM calculations is that the interaction between different clusters is represented by the Gaussian-type potentials. For example, one Gaussian type tensor potential used can be written as:

$$V_T = V_0(\vec{\tau}_1 \cdot \vec{\tau}_2)\left[3(\vec{\sigma}_1 \cdot \vec{r})(\vec{\sigma}_2 \cdot \vec{r}) - (r^2\,\vec{\sigma}_1 \cdot \vec{\sigma}_2)\right] e^{-\beta r^2} \qquad (6.9)$$

The Pion-Seagull exchange term can be extracted to be [Sch92],

$$\begin{aligned} \vec{J}_{\text{s-gte}}(\vec{r}) = -\frac{eV_0}{4\hbar\beta^2}\sum_{i<j}\left[\tau_i \times \tau_j\right]_3((3\vec{\sigma}_i(\vec{\sigma}_j\nabla_j) \\ -(\vec{\sigma}_i\vec{\sigma}_j)\nabla_j)\delta(\vec{r}-\vec{r}_i)e^{-\beta(\vec{r}_i-\vec{r}_j)^2}) \\ +(\mathrm{i} \leftrightarrow \mathrm{j}) \end{aligned} \qquad (6.10)$$

where V_0 is the constant normalization, β is the adjusting parameter, τ and σ denote isospin and spin matrices respectively. This term corresponds to the second diagram in Figure 6.3.

The Coulomb interaction part is calculated exactly in RRGM method, unlike in many other approaches [Hof86]. The spatial 1/r dependence in the Coulomb potential can be expanded into an integration of the Gaussian function as shown in the following form

$$\frac{1}{r} = 2\sqrt{\frac{\beta}{\pi}}\int_0^\infty dk \exp(-k^2\beta r^2) \qquad (6.11)$$

where β can be the potential adjusting parameter. Therefore, each term in Equation 6.5 can be treated as a Gaussian shape potential in the similar manner that will be described next.

6.4 Wave Functions

The ansätz for constructing the total wave function in RRGM has been given in detail in the paper of H. Hofmann [Hof83]. The ^{3}He wave function that will be described here is the simplest two-cluster structure under this model.

In general, the total wave function are the linear combinations of the base function Ψ_k, which is postulated to be

$$\Psi_k^{(J^\pi)} = \mathbf{A}\left\{\sum_{\lambda=1}^{N_k}\phi_\lambda\varphi_{k,\lambda}{}^{rel}(R_\lambda)\right\}$$
$$= \mathbf{A}\left\{\sum_{\lambda=1}^{N_k}\phi_\lambda\left[\delta_{\lambda k}F_k(R_k) + a_{\lambda k}G_\lambda(R_\lambda) + \sum_\mu b_{\lambda k}^\mu \exp(-\beta_\mu R_\lambda{}^2)\right]\right\} \qquad (6.12)$$

where **A** is the antisymmetrizing operator, N_k is the total number of cluster configurations (or channels) for the system (for ^{3}He, N_k=3) and φ^{rel} is the function describing the relative motion among the clusters. It contains a regular and an irregular Coulomb functions $F(R_\lambda)$ and $G(R_\lambda)$ to account for the asymptotic scattering behavior of the wave function. A linear combinations of Gaussian function is also included to account for the distortions in the reaction region [Hof83].

The ϕ_k in Equation 6.12 is the fragmentation wave function. In the case of two-cluster ^{3}He, it becomes

$$\phi_k = \frac{1}{R_k}Y_{L_k}(\hat{R}_k)\otimes\left[\chi_k^{J_1}\otimes\chi_k^{J_2}\right]^{J=J_1+J_2} \qquad (6.13)$$

where Y_L is the associated spherical harmonics function. Two fragments wave function χ with angular momenta of J_1 and J_2 are coupled to the total channel momentum of J.

The underlying construction of the fragment's wave function χ is the heart of the Refined Resonating Group Model. The following explicit form for ^{3}He has been postulated,

$$\chi = \left[c_1\exp(-\frac{\beta_1}{3}\sum_{i<k}(\vec{r}_i-\vec{r}_k)^2) + c_2\exp(-\frac{\beta_2}{3}\sum_{i<k}(\vec{r}_i-\vec{r}_k)^2)\right]\Xi^{J=\frac{1}{2}} \qquad (6.14)$$

where c_1 and c_2 are the coupling coefficients and Ξ are the spin-isospin components.

The final determination of the total wave function as in Equation 6.14 is calculated through the Kohn variational principle, namely,

$$\delta\left\{\langle\Psi|H-E_0|\Psi\rangle-\frac{1}{2}a_\lambda\right\}=0 \qquad (6.15)$$

The expansion coefficients a's and b's in Equation 6.13 are thus determined by solving Equation 6.15. The final parameters for ^{3}He can be found in the reference by S. Weber [Web92].

6.5 Results of RRGM Calculations and Comparison With Data

The calculated results at $E_{c.m.}$= 50 keV for all the analyzing powers compared with measured values are shown from Figure 6.4 to Figure 6.9.

As it can be seen that the calculations well predict the trends of the data for T_{20} data at 50 keV. However, the signs in the calculated A_y for ^{1}H(p,γ)^{3}He are negative while our measurements consistently show positive values. After careful evaluation, it was found that RRGM calculations could show a great sensitivity to the nucleon-nucleon potentials at very low energies[Muk94] and such sensitivities would greatly affect the final form of the wave functions.

Since low energy radiative capture processes are highly peripheral, i.e. the reaction usually happens in the asymptotic region of the overlapping wave functions between initial and final states, the tail of the entrance channel wave function can be typically described by

the shape of a Whittaker function up to a normalization factor due to the Coulomb interaction.

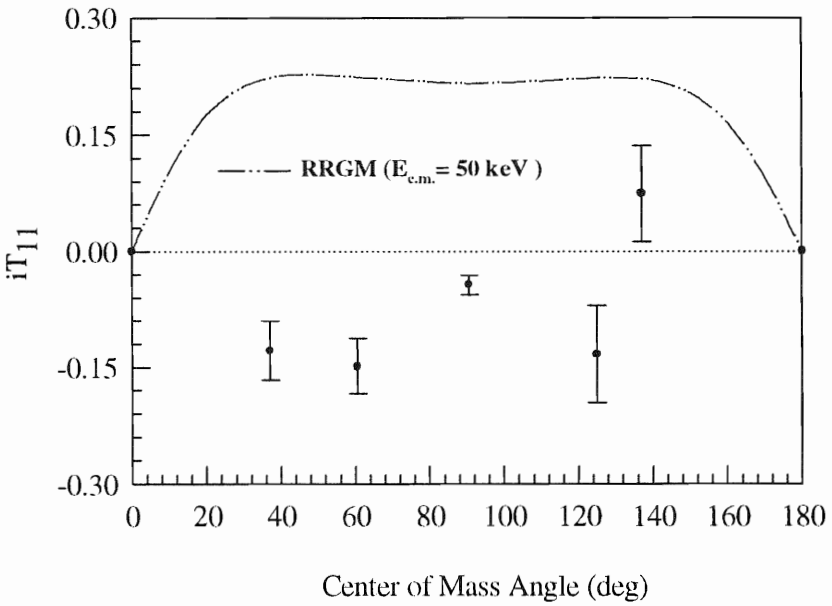

Figure 6.4. Comparison between measured iT_{11} and RRGM calculations for $^1H(\vec{d},\gamma)^3He$ reaction. The data points shown here are the measured results at $E_{c.m.}$= 50 keV.

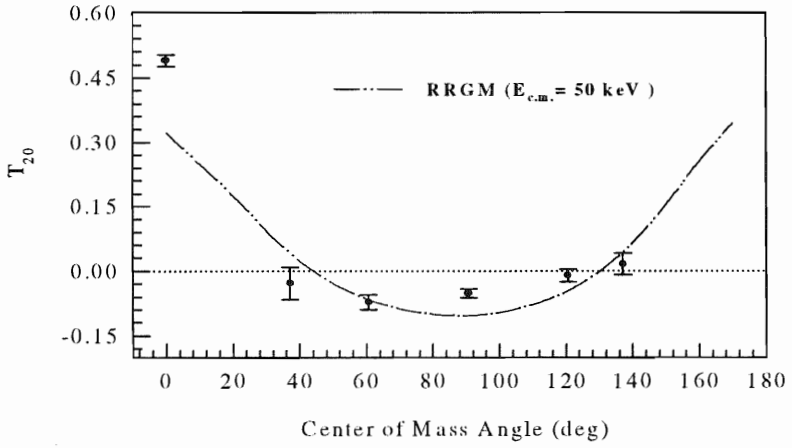

Figure 6.7 RRGM calculations and measured T_{20} for $^1H(\vec{d},\gamma)^3He$ at $E_{c.m.}$=50 keV.

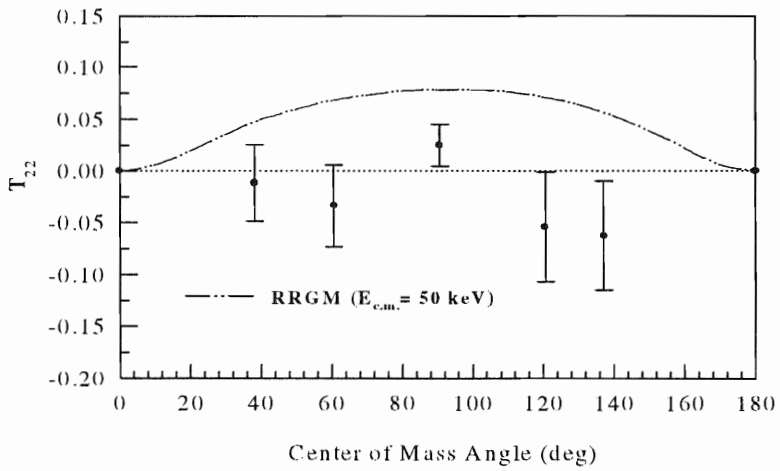

Figure 6.8 RRGM calculations and measured T_{22} for $^1H(\vec{d},\gamma)^3He$ at $E_{c.m.}$=50 keV.

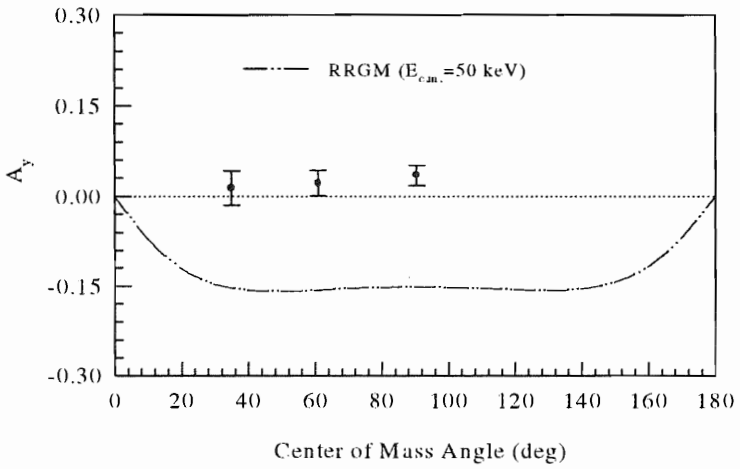

Figure 6.9 RRGM calculations compared with A_y data for $^2H(\vec{p},\gamma)^3He$ at $E_{c.m.}$=70 keV.

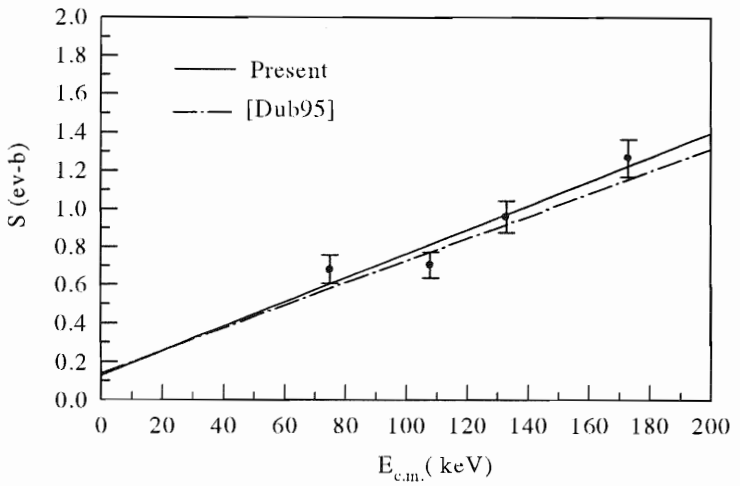

Figure 6.10 The extracted S-factor in comparison with an independent model calculation,

In the RRGM calculation, the expansion method of the Gaussian type potentials usually *overestimates* the asymptotic normalization constant, therefore the behavior of the wave functions in this region is easily distorted. This has already been observed in the low energy $^{7}Be(p,\gamma)^{8}B$ calculations and this effect could carry a strong influence to the analyzing powers [Muk94].

Another independent model calculation essentially using the RRGM formalism has been published recently by Dubovichenko[Dub95]. In this calculation, only E1 transition process has been considered. The predicted S(0)=0.13±0.02 (ev-b) matches *exactly* the presently measured S(0) as seen in Figure 6.10. The calculation has also shown that S(0) value has virtually no dependence on the choice of the selected nucleon-nucleon potentials. This result has ascertained that two-body cluster model calculations are generally adequate for describing the cross section but not the analyzing powers for proton-deuteron capture reactions.

6.6 Full Three-body Variational Method

In the context of full three-body formalism, Hamiltonian of the total system in Equation 6.3 should include extra potential terms which describe the effects of three-body interaction. Conceptually, these terms should be strongly correlated with each other. The general form for the full three-body Schrödinger equation is usually given as

$$i\hbar\frac{d}{dt}\Psi = (H_0 + (V_{12} + V_{13} + V_{23} + u^c + W_{123}))\Psi \qquad (6.16)$$

where V_{ij} represents the nuclear interaction between particle i and j, u^c denotes the Coulomb interaction between two protons inside ^{3}He, and W_{123} is the three body force in the separable form of $W_{123} = W_1 + W_2 + W_3$.

It can be seen from Equation 6.16 that physically separating the correlation between these three potential terms is the key challenge in solving this equation. The usual approach selected to tackle this problem is generally selected by using the famous Faddeev expansion method [Fad61].

In this section, a newly developed method for calculating the exact three body quantum systems will be discussed. The method is called Correlated Hyperspherical Harmonics (CHH) expansion and it has been developed by the group consisting of the collaboration of Kievsky and Viviani from INFN, University of Pisa and Schiavilla at CEBAF. The underlying technique for the calculation is based on the variational principle. It is the major improvement over many other methods based on the original Faddeev method. In this technique, a new set of correlated hyperspherical harmonics basis functions is multiplied by appropriate correlation factors to form the trial wave functions for the system under consideration. The purpose for such a series of expansion is basically to fine tune the behavior of the radial components of the variational wave functions. In this way, CHH method can adequately handle both the realistic soft-core and hard-core nucleon-nucleon potentials.

By comparing with other full-three body calculations either in the configuration space or in momentum space, CHH method has achieved remarkable agreements. For one simple example, the binding energies of ^{3}H and ^{4}He calculated from CHH method compared with other methods are listed below.

	^{3}H (MeV)	^{4}He (MeV)
CHH	-8.484	-23.93
Experimental	-8.48	-23.80

Table 6.1 Comparison of calculated ^{3}H and ^{4}He binding energies with experimental values.

One of the important features in the CHH calculations is its explicit inclusion of all the leading terms in the exchange-current field, including even Δ degrees of freedom [Kie94]. In the discussion of the following sections, the treatment of Coulomb interaction in this method will also be explored. Finally, calculated results will be presented and compared with our experimental measurements.

6.7 Faddeev Expansions

In order to solve Schr^dinger equation as shown in Equation 6.13, Faddeev first proposed that the total wave function Ψ can be decomposed into three components under Jacobi coordinate system, i.e.

$$\Psi = \psi_1(\vec{x}_i, \vec{y}_i) + \psi_2(\vec{x}_j, \vec{y}_j) - \psi_3(\vec{x}_k, \vec{y}_k), \tag{6.17}$$

where Jacobi coordinates are given in the cyclic order of (i, j, k) = (1, 2, 3) as the following,

$$\vec{x}_i = \frac{1}{\sqrt{2}}(\vec{r}_j - \vec{r}_k), \qquad \vec{y}_i = \frac{1}{\sqrt{6}}(\vec{r}_j + \vec{r}_k - 2\vec{r}_i). \tag{6.18}$$

This is illustrated in the following Figure 6.11 for ^{3}He system.

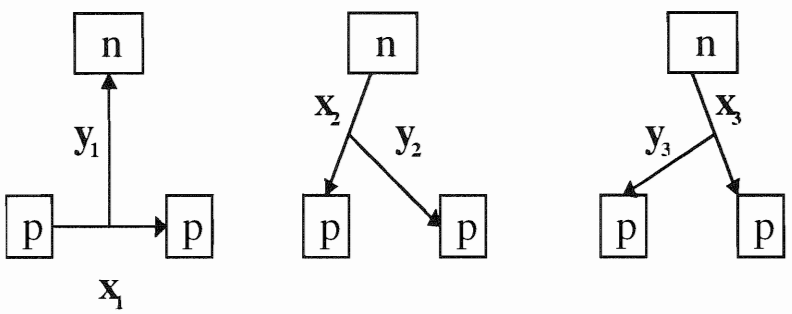

Figure 6.11 The definitions of Jacobi coordinates for ^{3}He system.

It can be proven [Fad61] that these three Faddeev components satisfy the following modified Faddevv equations as derived from Equation 6.16,

$$\left[E - H_0 - (V_{23} + u^c)\right]\psi_1 = \left[V_{23} + u^c\right](\psi_2 - \psi_3) + W_1(\psi_1 + \psi_2 - \psi_3) \quad (6.19)$$

$$\left[E - H_0 - V_{13}\right]\psi_2 = V_{13}(\psi_1 - \psi_3) + W_2(\psi_1 + \psi_2 - \psi_3) \quad (6.20)$$

$$-\left[E - H_0 - V_{12}\right]\psi_3 = V_{12}(\psi_1 + \psi_2) + W_3(\psi_1 + \psi_2 - \psi_3) \quad (6.21)$$

By summing together Equations 6.19-6.21 on both and left and right hand-sides, the Schrödinger Equation 6.16 for the energy eigenstates can be recovered:

$$(H_0 + (V_{12} + V_{13} + V_{23} + u^c + W_{123}))\Psi = E\Psi \quad (6.22)$$

Hence, the Equations 6.19-6.21 are consistent with the three-body Schrödinger Equation 6.16. From Equations 6.19-6.21, we can see that the Faddeev components satisfy an array of second-order linear differential equations. Moreover, each equation is ingeniously separated in the way that it involves only the interacting potentials between two nucleons inside the three-body system. Numerically, the computational effort to solve such second-order linear differential equations is much less than solving one nonlinear equation like Equation 6.16.

6.8 Variational Wave Functions

In the approach of the variational method, the adjusted variational wave function for ^{3}He is given by [Sch95b]

$$\Psi = S\left[\prod_{i<j} F_{ij}\right]|\Phi\rangle$$
$$= S\left[\prod_{i<j}(f^{c}(r_{ij}) + f^{t}(r_{ij})S_{ij}(\vec{\tau}_i \cdot \vec{\tau}_i) + \text{ (other spin - isospin terms)}\right]|\Phi\rangle \qquad (6.23)$$

In this equation, a symmetrized product of correlated operators is generated to act on an antisymmetrized and independent trial wave function $|\Psi\rangle$, whose eigenvalues can be evaluated from a two-body Hamiltonian as shown in Equation 6.3. The matrix elements are evaluated by applying the variational principle. To calculate the binding energy of ^{3}He, it simply goes by solving,

$$\delta\left[E = \frac{\langle\Psi_f|H_{total}|\Psi_i\rangle}{\langle\Psi_f|\Psi\rangle}\right] = 0 \qquad (6.24)$$

In the CHH method, the Faddeev components of the ^{3}He wave function in Equation 6.17 can be expanded to the following form in the L-S coupling scheme [Kie93],

$$\Psi(\vec{x}_i, \vec{y}_i) = \sum_{\alpha} \Phi_{\alpha}(\vec{x}_i, \vec{y}_i)[Y_{\alpha}(\hat{x}_i) \otimes Y_{\alpha}(\hat{y}_i)] \otimes \Xi(\vec{S}, \vec{\tau}), \qquad (6.25)$$

where Y is the normal spherical harmonics and Ξ represents spin-isospin coupling. By introducing the hyperspherical coordinates, i.e.,

$$\begin{cases} x_i = \rho\cos(\phi_i) \\ y_i = \rho\sin(\phi_i) \end{cases} \qquad (6.26)$$

the radial dependence of the total wave function Φ in Equation 6.25 can again be expanded under the basis of hyperspherical polynomials. Such an expansion is chosen mainly for the reason of fast convergence. It is especially suited to describe the soft

interparticle interactions, where only a small number of the basis function are sufficient to reproduce the wave function with a reasonable accuracy [Kie93]. The final form of the wave function from Equation 6.25 is determined from the functional Rayleigh-Ritz principle,

$$\langle \delta\Psi | (H - E) | \Psi \rangle_{\Omega} = 0. \qquad (6.27)$$

where integration is done over all the solid angles of $d\Omega = \sin^2 \phi_i \cos^2 \phi_i d\phi_i d\hat{x} d\hat{y}$.

The initial continuum wave function for calculating the low energy proton-deuteron reaction is in the form of [Kie95]

$$\Psi_{p+d} = \sum_{J,L,S} \Psi_d \left[F_L(qy) + R G_L(qy) \right] / qy \qquad (6.28)$$

where y is the relative proton-deuteron distance, Ψ_d is the deuteron wave function, F and G are the regular and irregular Coulomb functions, R is the reaction R-matrix element, and q is relative proton-deuteron wave number. The sum in Equation 6.28 is over the relative proton-deuteron orbital angular momentum(L), entrance channel spins (S=1/2, 3/2) and the total angular momentum J (=L+S). The R-matrix elements in Equation 6.28 are calculated again through variational principles. Finite partial waves are normalized so that when y goes to infinity, Ψ_{p+d} becomes plane wave $\Psi_{p+d} = e^{iqy}$.

Although both bound state and scattering state wave functions are generated by the variational principles, they give very accurate results. For example, by using realistic AV18 potential plus a three-body force component(Urbana IX) in the proton-deuteron

capture calculations [Sch86], the ^{3}H binding energy is reproduced exactly and ^{3}He binding energy is predicted within 1% of the experimental value [Kie95].

The meson-exchange-current is also treated properly in the calculation, and the leading term can be generated consistently from the AV18 potential [Sch95b]. In the present prescription, the Δ degrees of the freedom are also included in a non-perturbative way. The details of this calculation can be found in the paper of Schiavilla [Sch92].

6.9 Results of CHH Calculations and Comparison With Data

The comparison of CHH calculations with experimental data are shown in Figures 6.12-6.15.

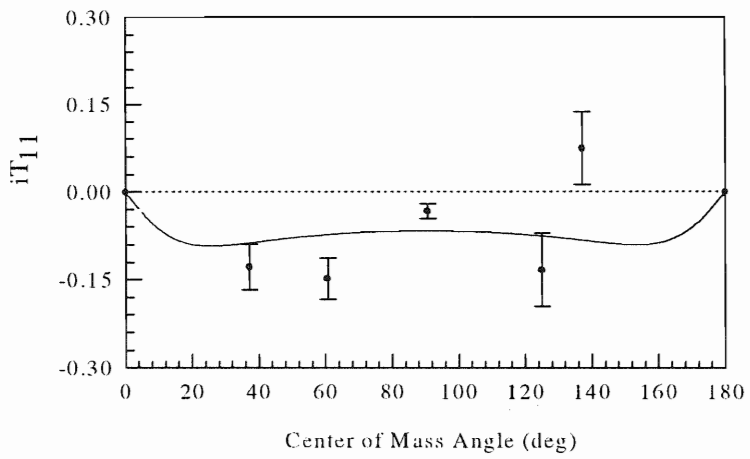

Figure 6.12 Comparison between CHH model calculation and measured iT_{11} for $^1H(\vec{d},\gamma)^3He$ reaction at $E_{c.m.}$=50 keV.

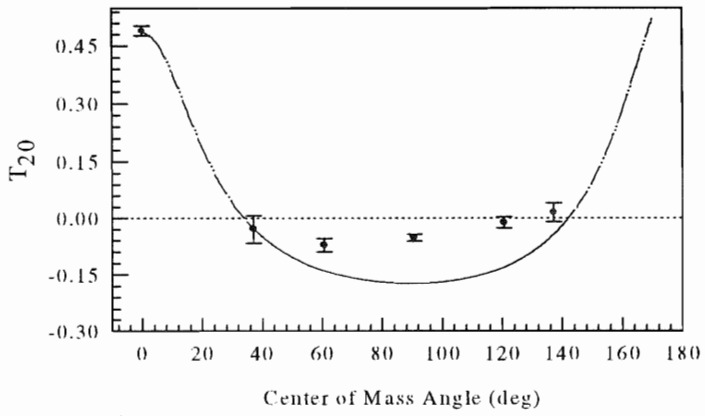

Figure 6.13 Comparison between CHH model calculation and measured T_{20} for $^1H(\vec{d},\gamma)^3He$ reaction at $E_{c.m.}$=50 keV.

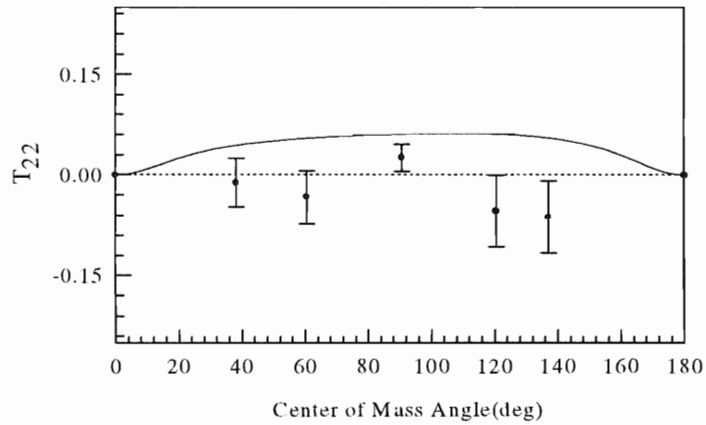

Figure 6.14 Comparison between CHH model calculation and measured T_{22} for $^1H(\vec{d},\gamma)^3He$ reaction at $E_{c.m.}$=50 keV.

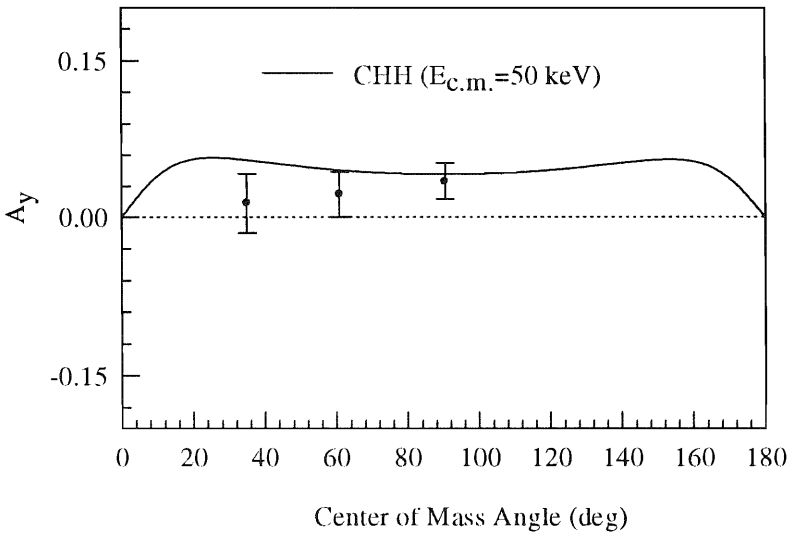

Figure 6.15 Comparison between CHH model calculation at $E_{c.m.}$=50 keV and the measured A_y for $^2H(\vec{p},\gamma)^3He$ reaction at $E_{c.m.}$=70 keV.

As it can be seen from Figures 6.12-6.15, CHH calculation generally predicts the trends of the measured analyzing powers quite well. For T_{20} results, we have achieved remarkable agreements at the forward angles, especially at zero degree. Since M1 contribution should be dominant at zero degree and, as described earlier it is very sensitive to meson exchange current effects, we can conclude that meson-exchange current treatment is adequate in the CHH model.

The predicted curve of the astrophysical S-factor from the CHH model calculations and the measured values are further compared in the following Figure 6.16.

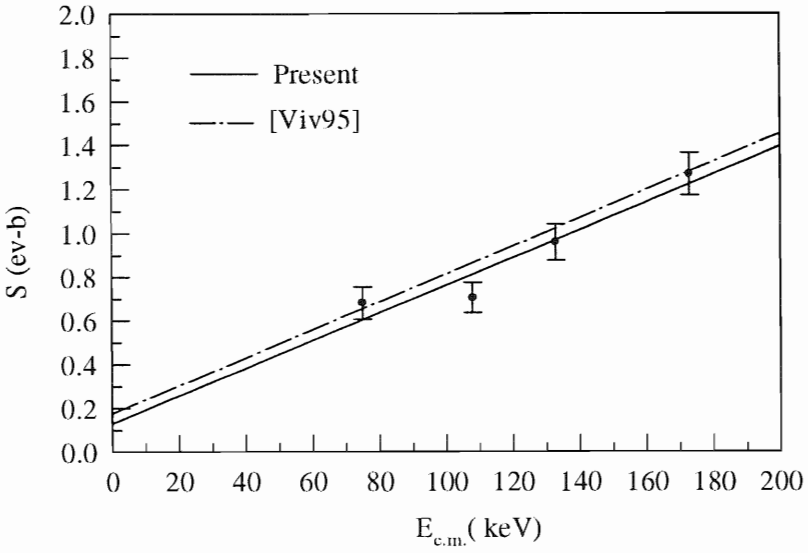

Figure 6.16 Comparison between CHH model calculation of astrophysical S-factor and the measured results.

As it can been, the measured data all agree excellently with the CHH predictions. The calculated S(0)=0.180 (ev-b) agrees the present experimental value of 0.130± 0.074 within one-sigma statistical error. All the measured S-factors can be described very well by CHH calculations within statistical uncertainties.

However, it can be seen that some disagreements still exists between the present measured analyzing powers and CHH model predictions, especially the T_{20} data at 90° for $E_{c.m.}$= 50 keV. Regarding these disagreements, it is suspected that due to cancellations among all the E1 matrix elements, calculations would become very difficult to pinpoint the contributions from some particular matrix elements, especially from the ones with channel spin 3/2. A strong sensitivities could be developed for the three-body force models we used, i.e. AV18+Urbana IX TNI [Viv95].

Further calculations at other measured energies in the present work are currently under way at Pisa. One may expect that specific aspects of CHH calculations ca be discerned from the energy dependence of the measured polarization observables.

VII. Conclusion and Future Work

In this final chapter, a brief summary of this whole thesis project will be given: firstly the experimental and theoretical effort will be described; secondly the astrophysical implications of the present measurements of the astrophysical S-factor will be explored; thirdly, the suggestions for the future work will be discussed.

In the course of this work, we have completed the measurements of cross sections and vector analyzing powers A_y of $^2H(\vec{p},\gamma)^3He$ reaction in the energy region of $E_{c.m.}$=70-210 keV. We have also measured the vector and tensor analyzing powers iT_{11}, T_{20}, T_{22} of $^1H(\vec{d},\gamma)^3He$ reaction in the energy region of $E_{c.m.}$= 40-110 keV. It is the first time that such an extensive set of polarization observables has been measured at these energy regions. Despite the fact that the measured reactions have a very low cross section (under1 μb), a consistent data set has been obtained.

The experiments are performed at Triangle Universities Nuclear Lab (TUNL) using Atomic Beam Polarized Ion Source (ABPIS) and Low Energy Beam Accelerator Facility (LEBAF). During the experiments, polarized proton or deuteron beam was directed onto a vapor condensed ice or heavy ice targets. The γ-rays of energy around 5.7 MeV resulting from the proton-deuteron radiative capture reactions were observed by two large volume High Purity Germanium (HPGe) detectors. The absolute efficiency of the detector for the full energy γ-ray peak was precisely calibrated using both commercially manufactured radioactive γ-ray source and the $^9F(p,\alpha\gamma)^{16}O$ resonance reaction at E_p=346

keV. The measured efficiency was in a very good agreement with the results obtained from a full Monte Carlo simulation, which mathematically modeled the detector response.

Due to the fact that the beam was completely stopped in the solid ice or heavy ice target, the full energy peak of the γ-rays observed in the HPGe detector exhibited an energy dependence that was convoluted with the reaction cross section. A sophisticated analysis method for spectrum deconvolution was successfully developed and implemented in the due course of this work. The method is highly effective in analyzing the obtained γ-ray spectra for obtaining analyzing powers. It is poven to be robust against all the spin-independent effects and most spin-dependent effects.

The polarizations of the beam for the present experiment were carefully monitored through three different polarimeters: ^{4}He($\vec{p}$,p')^{4}He polarimeter, high energy ^{3}He($\vec{d}$,p)^{4}He polarimeter using Van de Graaff tandem accelerator, and a recently developed low energy ^{3}He($\vec{d}$,p)^{4}He polarimeter. The measured polarizations for the beam were consistently stable throughout most of the experimental runs that lasted more than 4 weeks of data collecting time.

The astrophysical S-factors for the ^{2}H(p,γ)^{3}He reaction have also been determined at four averaged reaction energies, i.e. $<E_{c.m.}>$=75, 108, 133, 173 keV. Accordingly, the linear energy dependence of the S-factor is extracted.

Our final analyzing powers results have been compared with both Refined Resonating Group Model (RRGM) calculations and full three-body correlated hyperspherical harmonics (CHH) expansion calculations. It has been found that RRGM

model disagrees with some of the measured results, especially the predicted signs of the vector analyzing powers for both $^2H(\vec{p},\gamma)^3He$ and $^1H(\vec{d},\gamma)^3He$ from RRGM are just opposite of those of the measured data. The disagreements are most likely due to the intrinsic two-body structures of the RRGM method, especially the overestimation of the asymptotic normalization constants for the wave functions.

The full three-body variational calculation agrees reasonably well with the trends of all the analyzing powers data. It is found that meson-exchange-current effects play an important role in explaining these data. Although the proton-deuteron reactions are dominated by E1 and M1 transitions, E2 transition gives a small yet appreciable contributions to the measured T_{22} analyzing powers, as indicated by the coefficients of fitted Legendre polynomials. The CHH calculation has shown remarkable agreements with our measurements of T_{20} at the forward angles. Some disagreements between the calculation and the measured data at $E_{c.m.}$=50 keV are most likely due to the model sensitivities to particular matrix elements, which may still need to be refined in the future calculations.

The final analysis of the cross section data was conducted by assuming predominant E1 transitions in their angular distributions, which had been tested and implemented in the previous measurements. This assumption was also ascertained by a recent TUNL measurement at lower reaction energies. Our final results for the energy dependence of the astrophysical S-factors are compared with the predictions from both the full three-body CHH model and a two-body cluster model. The measured data agrees reasonably well with all the theoretical predictions. Furthermore, our measured

S(0)=0.130±0.074 ev-b is virtually the same as the result from a recent measurements by Schmid *et al.*, which was quoted as 0.136±0.013 ev-b. This value is about 45% lower than the previously measured by Griffith. Even though our measured cross sections are in agreements with the previous measurements of the Griffith and Bailey at the same energy range.

The astrophysical significance for the proton-deuteron capture reaction lies in the fact that it is the "bottle-neck" process in the primary P-P chain reactions determining the formation of observed cold stars. The reaction itself affects the deuterium depletion process of the prostellar evolution and the ^{3}He production rate thus primordial ^{3}He abundance. If further confirmed, the recent measured 45% lower S(0) value may significantly change the results of many standard astrophysical model calculations regarding the evolution of main sequence stars and some protostars.

In the prospect of future theoretical analysis, calculations of all the analyzing powers and the cross sections for the reaction energy near $E_{c.m.}$=100 keV under the full three-body formalisms would be beneficial for the investigation of energy dependence of all the data that have been obtained in the present project. Such calculations are presently in progress at Pisa group and the final results will be expected in the near future. More theoretical work is also needed to test the sensitivities of various nucleon-nucleon potentials in the full three-body dynamics. We intend to pursue a detailed comparison between the present data with the calculations using different nucleon-nucleon potentials. Furthermore, calculations are also need to check the quantitative Coulomb contribution to the reaction mechanism. A straight-forward approach would lead to comparing neutron-

deuteron capture reactions with proton-deuteron capture reactions. Moreover, the source(s) of the most contributing matrix elements to the tensor analyzing powers in the present CHH model calculations should be examined in more details as discussed in Chapter 5.

From the perspective of future experimental work, the measurement of the full angular distribution and energy dependence for the analyzing powers at the center of mass energies below 30 keV could be the next challenge to take.

References

[Ald92] Aldrich Chemical Company, Inc., *Aldrichem Data Search* (IBM Software No. Z17000-3, 1992).

[Ald93] C. Alderliesten, Nucl. Inst. Meth., A335(1993) 219.

[Alt78] E.O. Alt, W. Sandhas and H. Ziegelmann, Phys. Rev. C 17(1978)1981

[And77] H.H. Anderson and J.F. Ziegler, *Hydrogen Stopping Powers and Ranges in All Elements* (Pergammon Press, New York, 1977).

[Arr83] A. Arriaga, F.D. Santos, Phys. Rev. C29(1983) 1945.

[Aus52] N. Austern, Phys. Rev. 85(1952) 247.

[Bai70] G.M. Bailey, G.M. Griffiths, M.A. Olivo, and R.L. Helmer, Can. J. Phys. 48(1970) 3059.

[Bal87] J.L. Ballot and A.M. Eiro, *Few Body Systems* (Springer-Verlag, New York, 1987).

[Bar67] I.M. Barbour and A.C. Phillips, Phys. Rev. Let. 19(1967) 1388.

[Ber86] B.L. Berman and B.F. Gibson, *Lecture Notes in Phys. vol. 260* (Springer-Verlag, Berlin, 1986).

[Ber88] G.H. Berthold, A. Stadler and H. Zankel, Phys. Rev. Lett. 61(1988)1077.

[Bet39] H. Bethe, Phys. Rev. 55(1939) 434.

[Bie80] J. Biersack and L. Haggmark, Nucl. Instr. Meth., 174(1980) 257.

[Bla93] T.C. Black, B.E. Hendrix, E.R. Crossson, K.A. Fletcher, H.J. Karwowski, E.J. Ludwig, Nucl. Instr. Meth. A333(1993)239.

[Bla95] T.C. Black, *Ph.D. Thesis*, University of Noth Carolina at Chapel Hill, 1995

[Bok69] J.C. Bokros, *Chemistry and Physics of Carbon* (Marcel Dekker, New York, 1969).

[Bow89] J. Bowsher, *Ph.D. Thesis* (University of North Carolina at Chapel Hill, 1989).

[Bru93] R. Brun, Program Library Q121, CERN (1993).

[Bru94] C.R. Brune, *Ph.D. Thesis* (California Institute of Technology, 1994).

[Car88] J. Carlson, Phys. Rev. C 38(1988) 1897.

[Cha34] J. Chadwick and M. Goldhaber, Nature 134(1937)237.

[Che86] C.R. Chen, G.L. Payne, J.L. Friar and B.F. Gibson, Phys. Rev. C 25(1986) 1740.

[Cla83] D.D. Clayton, *Principles of Stellar Evolution and Nucleosynthesis* (University of Chicago Press, Chicago and London, 1983).

[Cle94] T. B. Clegg, T. Mendez, C. Roper, J. Dunham, Bull. of the Am. Phy. Soc. 40(1994) 10 .

[Cle93] T.B. Clegg, J. Dunham and E. Crosson, *Atomic Beam Polarized Ion Source Operating Manual*, (TUNL, Duke University, 1993).

[Coh72] B.L. Cohen, C.L. Fink and J.H. Degnan, J. Appl. Phys. No.1 43(1972) 19

[Don64] T.W. Donnelly, *Ph.D. Thesis* (University of British Columbia, 1964).

[Dub95] S.B. Dubovichenko, Phys. of Atomic Nuclei, Vol 58, 7(1995) 1253.

[Dus62] S. Dushman, *Scientific Foundations of Vacuum Technique* (John Wiley and Sons, New York, 1962).

[Eir91] A.M. Eiro and F.D. Santos, J. Phys. G16(1991) 1129.

[Fad60] L.D. Faddeev, Zh. Eksp. Teor. Fiz. 39(1960) 1459.

[Fad61] L.D. Faddeev, Sov. Phys. JETP 12(1961) 1014.

[Fes74] H. Feshbach and A. Shalit, *Theoretical nuclear physics* (John Wiley & Sons, New York, 1974).

[Fle92] K. Fletcher, *Ph.D. Thesis* (University of North Carolina at Chapel Hill, 1992).

[Fon91] A.C. Fonseca and D.R. Lehman, Phys. Lett. B267(1991) 159.

[Fon93] A.C. Fonseca and D.R. Lehman, Phys. Rev. C 48(1993) R503.

[Fow62] W.A. Fowler, J.L Greenstein and F. Hoyle, Geophys. J. 6(1962) 148.

[Fri88] J.L. Friar, B.F. Gibson, D.R. Lehman, and G.L. Payne, Phys. Rev. C 37(1988) 2859.

[Fri90] J.L. Friar, B.F. Gibson, G.L. Payne, Phys. Lett. B251(1990) 11.

[Fri95] J.L Friar, Summary talk on the 14th International IUPAP conference on Few Body Problems in Physics, unpublished, 1995.

[Gei95] W. Geist, Z. Ayer, A.C. Hird, H.J. Karwowski and E.J. Ludwig Nucl. Inst. Meth. A365(1995)36.

[Gib76] B.F. Gibson and D.R. Lehman, Phys. Rev. C 139(1976) 477.

[Gil81] P.E. Gill, W. Murray and M.H. White, *Practical Optimization* (Academic Press, New York, 1981).

[Glö90] W. Glöckle, H. Witala and T. Cornelius, Nucl. Phys. A508(1990) 115c.

[Goe92] F. Goeckner, W.K. Pitts and L.D. Knutson, Phys. Rev. C 45(1992) R2536.

[Gou81] C.R. Gould, L.G. Holzsweig, S.E. King, Y.C. Lau, P.V. Poore and N.R. Roberson. IEEE Tans. Nucl. Sci. NS-28(1981) 3708.

[Gri55] G.M. Griffiths and J.B. Warren, Proc. Phys. Soc. A68(1955) 781.

[Gri62] G. M. Griffiths, E.A. Larson and L.P. Robertson, Can. J. Phys. 40(1962) 402.

[Gri63] G.M. Griffiths, M. Lal and C.D. Scarfe, Can, J. Phys. 41(1963) 724.

[Had86] E. Hadjimicheal, *Few-body problems, Int. Rev. Nucl. Phys. 3* (World Scientific, Singapore, 1986).

[Hae70] W. Haeberli and H.H. Barschall, *Proceedings of the Third International Symposium on Polarization Phenomena in Nuclear Reactions* (Cushing-Malloy, Inc., Michigan, 1970).

[Hee85] W. Heeringa, R. Aures, R. Maschuw, and F.K. Schmidt, Cryogenics 25(1985) 369.

[Hof84] H.M. Hofmann, Nucl. Phys. A416(1984) 363.

[Hof83] H.M. Hofmann, T. Mertelmeier and W. Zahn, Nucl. Phys. A410(1983) 208.

[Hir94] A. Hird, private communications, 1994.

[Ish92] S. Ishikawa, Few-Body Systerms. Suppl. 6 (1992) 285.

[Jac74] J.D. Jackson, *Classical Electrodynamics* (John Wiley & Sons, New York, 1974).

[Jam77] F. James. Determing the statistical significance of experimental results, CERN Report 81-03, CERN (1981).

[Jor77] H.H. Jorsch, J.L. Campbell, Nucl. Inst. Meth. 143(1977) 551.

[Jou86] J. Jourdan, M. Baumgartner, S. Burzynski, P. Egelhof, R. Henneck, A. Klen, M.A. Pickar, G.R. Plattner, W.D. Ramsay, H.W. Roser and I. Sick, Nucl. Phys. A453(1986) 220.

[Kar86] H.J. Karwowski, K. Komisarcik, C. Foster, K. Pitts and B. Utts, Nucl. Instr. Meth. A245 (1986) 291.

[Kha84] F.M. Khan, *The Physics of Radiation Therapy* (Williams and Wilkins, Bartimore, MD, 1984).

[Kha92] V.F. Kharchenko, M.A. Navroskii and P.A. Katerinchuk, Sov. J. Nucl. Phys. 55(1992) 49.

[Kie93] A. Kievsky, M. Viviani, and S. Rosati, Nucl. Phys. A551(1993)241.

[Kie95] A. Kievsky, private communication.

[Kin83] S.E. King, N.R. Roberson, H.R. Weller and D.R. Tilley, Phys. Rev. Lett. 51(1983) 877.

[Kin84] S.E. King, N.R. Roberson, H.R. Weller, D.R. Tilley, H.P. Engelberty, H. Berry, E. Huttel and F. Clausnitzer, Phys. Rev. C 30(1984) 1335.

[Kos90] J.E. Koster, *Ph.D. Thesis* (North Carolina State University, 1990).

[Kra87] A. Krauss, H.W. Becker, H.P. Trautvetter and C. Rolfs, Nucl. Phys. A 456(1987) 150.

[Kra92] L.H. Kramer, *Ph.D. Thesis* (Duke University, 1992).

[Lan92] G. Lanzano, A. Pagano, S. Urso, E. De Filippo, B. Berthier, J.L. Charvet, R. Dayras, R. Legrain, R. Lucas, C. Mazur, E. Pollacco, J.E. Sauvestre, C. Volant, C. Beck, B. Djerround and B. Heusch, Nucl. Instr. and Meth. A312(1992) 515.

[Leh94] D. Lehman, Lecture notes 1994, unpublished.

[Leo87] W.R. Leo, *Thechniques for Nuclear and Particle Physics Experiments* (Springer-Verlag, New York, 1987).

[Lyo86] L. Lyons, *Statistics for nuclear and particle physicists* (Cambridge University Press, London, 1986).

[Mer86] T. Mertelmeier and H.M. Hofmann, Nucl. Phys. A 459(1986)387.

[Moo88] T. Mooney, *Ph.D. Thesis* (University of North Carolina at Chapel Hill, 1988).

[Muk94] A.M. Mukhamedzhanov, private communications.

[Nel65] J.A. Nelder and R. Mead, Comptu. J. 7(1965)149.

[Nel85] W.R. Nelson and A.F. Bielajew, SLAC Report-265(1985)1.

[Nov87] R. Novotny, R. Riess, R. Hingmann, H. Stroher, R.D. Fischer, G. Koch, W. Kuhn, V. Metag, R. Muhlhans, U. Kneissl, W. Wilke, B. Haas, J.P. Vivien, R. Beck, B. Schoch, Y. Schutz, Nucl. Instr. Meth. A262(1987) 340.

[Ort95] EG&G ORTEC, *Detectors & Instruments for nuclear spectroscopy* (EG&G, ORTEC, Oak Ridge, 1995).

[Par64] P.D. Parker, J.N. Bahcall and W.A. Fowler, Astrophys. J. 139(1964) 602.

[Pic87] M.A. Pickar, H.J. Karwowski, J.D. Brown, J.R. Hall, M.Hugi, R.E. Pollock, V.R. Cupps, M. Fatyga and A.D. Bacher, Phys. Rev. C. 35(1987) 37.

[Pit88] W.K. Pitts, H.O. Meyer, L.C. Bland, J.D. Brown, R.C. Byrd, M. Hugi, H.J. Karwowski, P. Schwandt, A. Sinha, J. Sowinski, I.J. van Heerden, A. Arriaga and F.D. Santos, Phys. Rev. C 37(1988)1.

[Ris72] D.O. Riska and G.E. Brown, Phys. Lett. B38(1972) 193.

[Ris84] D.O Riska, Progr. part. nucl. Phys. 11(1984) 199.

[Roe92] B.P, Roe, *Probability and Statistics in Experimental Physics* (Springer-Verlag, 1992).

[Rol88] C.E. Rolfs and W.S. Rodney, *Cauldrons in the Cosmos* (University of Chicago Press, 1988).

[Ros53] M.E. Rose, Phys. Rev. 91(1953) 610.

[Sag94] K. Sagara, TUNL 1994 seminar and private communication.

[Sey79] R.G. Seyler and H.R. Weller, Phys. Rev. C 20(1979) 453.

[Sey84] R.G. Seyler and H.R. Weller, Phys. Rev. C 30(1984) 1146.

[Sch71] P. Schwandt, T.B. Clegg, W. Haeberli, Nucl.Phys. A163(1971) 432.

[Sch86] R. Schiavilla, V.R. Pandharipande, R.B. Wiringa, Nucl. Phys. A449(1986) 219.

[Sch91] J. Schmidt, *Ph.D. Thesis* (University of Erlangen, Germany, 1991).

[Sch92] R. Schiavilla and D.O. Riska, Phys. Rev. C 45(1992) 2628.

[Sch95a] G.J. Schmid, *Ph.D. Thesis* (Duke University, 1995).

[Sch95b] R. Schiavilla, private communication.

[Sie31] A. Sieverts and A. Gotta, Z. anorg. Chem. 199(1931)384.

[Sie37] A.F.J. Siegert, Phys. Rev. 52(1937) 787.

[Sta88] G.R. Stahler, The Astrophy. J. 322(1988)804.

[Tak88] Y. Takeuchi, N. Imanishi, K. Toyoda, T. Uchino and M. Iwasaki, J. Appl. Phys. 64(1988) 2959.

[Tor84] J. Torre and B. Goulard, Phys. Rev. C 28(1984) 529.

[Ton80] S.A. Tonsfeldt, *Ph.D. Thesis* (University of North Carolina at Chapel Hill, 1980).

[Vet85] M.C. Vetterli, J.A. Kuehner, A.J. Trudel, C.L. Woods, R. Dymarz, A.A Pilt, and H.R. Weller, Phys. Rev. Lett. 54(1985) 1129.

[Viv95] M. Viviani, private communications.

[Wap85] A.H. Wapstra and G. Audi, Nucl. Phys. A432(1985) 1.

[Web92] S. Weber, *Ph.D. Thesis* (University of Erlangen, Germany, 1992).

[Wei92] S. Weinberg, Phys. Lett. B295(1992) 114.

[Wen52] W.A. Wenzel, W. Whaling, Phys. Rev. 87(1952)499.

[Whe37] J.A. Wheeler, Phys. Rev. 52(1937)1083.

[Wis84] K. Wisshäk, F. Kappeler and G. Schatz, Nucl. Instr. and Meth. 221(1984) 358.

[Wöl66] W. Wölfi, R. Bösch, J. Lang, R. Müller, and P. Marmier, Phys. Lett. 22(1966) 75.

[Wol91] S. Wolfram, *Mathematica* (Addison-Wesley, Menlo Park, 1991).

[Zie85] J.F. Ziegler, J.P. Biersack and U. Littmark, *The Stopping and Range of Ions in Solids* (Pergammon Press, New York, 1985).

[Zie92] J.F. Ziegler, private communication, 1992.